NRBF2, a novel component of the class III PtdIns3K complex, regulates starvation-induced autophagy and nuclear receptor-mediated gene expression

Inaugural-Dissertation

zur Erlangung des Doktorgrades
der Mathematisch-Naturwissenschaftlichen Fakultät
der Heinrich-Heine-Universität Düsseldorf

vorgelegt von

Niklas Berleth

aus Göttingen

Düsseldorf, August 2018

aus dem Institut für Molekulare Medizin I
der Heinrich-Heine-Universität Düsseldorf

Gedruckt mit der Genehmigung der
Mathematisch-Naturwissenschaftlichen Fakultät der
Heinrich-Heine-Universität Düsseldorf

Referent: Univ. Prof. Dr. Björn Stork

Korreferent: Univ. Prof. Dr. Thomas Klein

Tag der mündlichen Prüfung: 03.12.2018

Danksagung

Mein besonderer Dank gilt meinem Doktorvater Herrn Prof. Dr. Björn Stork für die hervorragende fachliche Betreuung, die vielen konstruktiven Diskussionen und seine uneingeschränkte Unterstützung während der gesamten Zeit meiner Promotion. Dadurch ließen sich auch so manche blau-weißen Probleme überstehen.

Herrn. Prof. Thomas Klein danke ich für die Bereitschaft, meine Dissertation zu betreuen und diese vor der Mathematisch-Naturwissenschaftlichen Fakultät der Heinrich-Heine-Universität Düsseldorf zu vertreten.

Bei Herrn Prof. Dr. Sebastian Wesselborg möchte ich mich für die Möglichkeit bedanken, meine Dissertation in seinem Institut anfertigen zu dürfen, sowie für seinen fachlichen Rat und das mir entgegengebrachte Vertrauen.

Ich danke allen Kooperationspartnern für die gute Zusammenarbeit, ohne deren Expertise zahlreiche Teile dieser Arbeit nicht möglich gewesen wären. Auch dem Team der Molekularen Radioonkologie möchte ich für ihre Hilfe und Unterstützung danken.

Alexandra Ziemski möchte ich für ihre Unterstützung bei der Generierung der Genexpressionsdaten und das großes Engagement während ihrer Bachelorarbeit danken.

Des Weiteren möchte ich mich bei den aktuellen und ehemaligen Mitgliedern der Molekularen Medizin I bedanken. Man mag es kaum glauben, aber Arbeit kann auch Spaß machen. Ihr habt das ermöglicht und mich in der langen Zeit immer unterstützt und das ein oder andere mal auch abgelenkt. Beides war wichtig. Nora, vielen Dank fürs Korrekturlesen, obwohl dein Platz im Büro schon lange leer ist.

Meinen Eltern und Jacqueline mit Matthias möchte ich für den ständigen Rückhalt und die Liebe danken. Ohne euch wäre diese Arbeit nicht möglich gewesen (aber das wisst ihr). Genauso danke ich dem „neu dazugekommen“ Teil meiner Familie und allen liebgewonnen Menschen, welche ich hier nicht namentlich aufgeführt habe. Ihr habt alle auf eure Weise zum Gelingen dieser Arbeit beigetragen.

Und das Wichtigste kommt zum Schluss: Ich danke meiner Frau Mareike für so viele Dinge. Was ein Glück, dass es dich gibt.

Remarks

The results depicted in Figure 5-10 and 5-11 were partially obtained by Alexandra Ziemski during her bachelor thesis, which was supervised by Niklas Berleth. The results depicted in Figure 5-14 were partially obtained by Dr. Nora Wallot-Hieke (Institute for Molecular Medicine I, Heinrich Heine University Düsseldorf, Germany). The purification of recombinant 6xHis fusion proteins was performed by M.Sc. Mareike Berleth (Institute of Biochemical Plant Physiology, Heinrich Heine University Düsseldorf, Germany). The mass spectrometric analysis of BECN1-interacting proteins was performed by Dr. Anja Stefanski (Molecular Proteomics Laboratory, BMFZ, Heinrich Heine University Düsseldorf, Germany) and the mass spectrometric analysis of NRBF2 phosphorylation status was performed by Dr. Astrid Tschapek (Institute of Cardiovascular Physiology, Heinrich Heine University Düsseldorf, Germany). The gene expression analysis by microarray was performed by Dr. René Deenen (Genomics & Transcriptomics Laboratory, BMFZ, Heinrich Heine University Düsseldorf, Germany).

Table of contents

Abbrevations

aa	amino acid
[Ca^{2+}]	Ca^{2+} concentration
[^{32}P]-ATP	[gamma-^{32}P] adenosine triphosphate
ACOX1	peroxisomal acyl-coenzyme A oxidase 1 (gene or protein)
AF	activation function
ALV	avian leukosis virus
AMBRA1	activating molecule in Beclin1-regulated autophagy
AML12	alpha mouse liver 12
Amp	ampicillin (or ampicillin resistance gene)
AMPK	adenosine 5'-monophosphate-activated protein kinase
APS	ammonium persulphate
ATCC	American type culture collection
ATG	autophagy related (gene or protein)
ATP	adenosine triphosphate
ATPase	adenosine triphosphatase
BafA1	bafilomycin A_1
Barkor	Beclin-1-associated autophagy-related key regulator
BAT	brown adipose tissue
Bcl-2	B cell lymphoma 2
BECN1	Coiled-coil myosin-like BCL2-interacting protein (Beclin 1) (gene or protein)
bleo	bleomycin (or bleomycin resistance gene)
β-ME	beta-mercaptoethanol
BMFZ	Biologisch-Medizinisches Forschungszentrum
BNIP3	Bcl-2 interacting protein 3 (gene or protein)
bp	base pair
BRET	bioluminescence resonance energy transfer
BSA	bovine serum albumin
CaMKKβ	Ca^{2+}/calmodulin-dependent protein kinase kinase β
CCL	cleared cellular lysate
cDNA	complementary DNA

ch	chicken
CHAPS	3-[(3-cholamidopropyl)dimethylammonio]-1-propanesulfonate
CMA	chaperone-mediated autophagy
co-AP	co-affinity purification
COPR	comodulator of PPAR and RXR
CQ	Chloroquine
CREB	CRE-binding protein
CRTC2	CREB-regulated transcription coactivator 2
CS	chicken serum
C_T	threshold value
CTSF	cathepsin F (gene or protein)
DNA	deoxyribonucleic acid
DAPK	death-associated protein kinase
DBD	DNA-binding domain
DFCP1	double FYVE domain containing protein 1
dH_2O	deionized H_2O
DMEM	Dulbecco's modified Eagle's medium
DMP	dimethyl pimelimidate
DMSO	dimethylsulfoxide
dNTP	2'-deoxynucleoside-5'-triphosphate
DPBS	Dulbecco's phosphate-buffered saline
dsDNA	double stranded DNA
DTT	1,4-dithiothreitol
E	Amplification efficiency
E. coli	Escherichia coli
EBSS	Earle's buffered salt solution
EDTA	ethylenediamine tetraacetic acid
EGFP	enhanced GFP
EGFR	epidermal growth factor receptor
EGTA	ethylene-glycol-bis(2-aminoethyl ether)-N,N,N',N'-tetraacetic acid
EMT	epithelial-mesenchymal transition

env	gene encoding glycoprotein 160 (envelope protein)
ER	endoplasmic reticulum
EtOH	ethanol
FastAP	fast alkaline phosphatase
FCS	fetal calf serum
FIP200	focal adhesion kinase family-interacting protein of 200 kDa
FOXO 1/3	forkhead box O proteins 1/3 (gene or protein)
FUNDC1	FUN14 domain-containing protein 1
FXR	farnesoid X receptor
GABARAP	gamma-aminobutyric acid A-receptor associated protein
gag	gene encoding p55 (core protein)
GAPDH	glyceraldehyde-3-phosphate dehydrogenase
GFP	green fluorescent protein
GO	GeneOntology
GST	glutathione-S-transferase
GTPase	guanosine triphosphatase
HA	nonapeptide from influenza hemagglutinin protein (YPYDVPDYA)
HCQ	Hydroxychloroquine
HDAC	histone deacetylase
HEK	human embryonic kidney
HEPES	2-[4-(2-Hydroxyethyl)-1-piperazinyl]-ethanesulfonic acid
HIF1 alpha	hypoxia-inducible factor 1 alpha
hisD	histidinol (or histidinol resistance gene)
HOAc	acetic acid
HPLC	high performance liquid chromatography
Hprt1	gene encoding for hypoxanthine-guanine phosphoribosyltransferase
HSC70	heat shock-cognate protein of 70 kDa
HTFR	homogeneous time resolved fluorescence
IB	immunoblot
IF	immunofluorescence
IFN	interferon

IgL	immunoglobulin light chain
IgM	immunoglobulin M
IL	Interleukin (gene or protein)
IM	isolation membrane
IP	immunopurification
IPTG	isopropyl-β-D-thiogalactopyranoside
IRF7	interferon regulatory factor 7 (gene or protein)
JNK1	c-Jun N-terminal protein kinase 1
JUN	Transcription factor AP-1 (gene or protein)
Kan	kanamycin (or kanamycin resistance gene)
KLD	Kinase Ligase *DpnI*
KOAc	potassium acetate
LA	left arm (in knock-out targeting constructs)
LAMP2A	lysosome-associated membrane protein 2 A
LB	lysis buffer or lysogeny broth
LBD	ligand-binding domain
LC	liquid chromatography
LC3-I	unlipidated (cytosolic) form of MAP1LC3B (apparent MW ~18 kDa)
LC3-II	PE-conjugated (membrane bound) form of MAP1LC3B (apparent MW ~16 kDa)
LDL	low-density lipoproteins
LIR	LC3-interacting region
LTQ	Linear Trap Quadrupole
MAP1LC3B	microtubule-associated proteins 1A/1B light chain 3B (gene or protein)
MAPK	p38 mitogen-activated protein kinase
MAPKAPK 2/3	MAPK-activated protein kinase 2/3
MCS	multiple cloning site
MEF	mouse embryonic fibroblast
MeOH	methanol
MHC	major histocompatibility complex
min	minute(s)
MIT	microtubule interacting and trafficking molecule

MMLV	Moloney murine leukemia virus
MOPS	3-(N-morpholino)propanesulfonic acid
mRNA	messenger RNA
MS	mass spectrometry
mTOR	mechanistic target of rapamycin
mTORC1/2	mechanistic target of rapamycin complex 1/2
MW	molecular weight
NBR1	neighbor of BRCA1 gene 1
NCBI	National Center for Biotechnology information
NCoR/SMRT	nuclear receptor co-repressor/silencing mediator for retinoid and thyroid hormone receptors
NES	nuclear export signal
NFKB1	gene encoding for nuclear factor NF-kappa-B p105 subunit
NFκB	nuclear factor kappa-light-chain-enhancer of activated B cells
NLS	nuclear localization signal
NRBF2	nuclear receptor-binding factor 2
OD	optical density
OPTN	optineurin
p	protein (as prefix or suffix) or phospho (as prefix)
PAGE	polyacrylamide gel electrophoresis
PAS	phagophore assembly site (or pre-autophagosomal structure)
PCR	polymerase chain reaction
PDAC	pancreatic ductal adenocarcinoma
PDB	Protein Data Bank
PE	phosphatidylethanolamine
PEP	posterior error probability score
PEX7	peroxisomal targeting signal 2 receptor / Peroxin-7 (gene or protein)
PIK3C3	phosphatidylinositol 3-kinase catalytic subunit type 3 (gene or protein)
PIK3R4	phosphoinositide 3-kinase regulatory subunit 4
PINK1	PTEN-induced putative kinase 1 (gene or protein)
PLA	proximity ligation assay

Plat-E	Platinum E
PMSF	phenylmethylsulfonyl fluoride
pol	gene encoding protease, reverse transcriptase and integrase
Polybrene	1,5-dimethyl-1,5-diazaundecamethylene polymethobromide
PPAR	peroxisome proliferator-activated receptor (gene or protein)
PPRE	peroxisome proliferator response elements
pSer	phosphoserine
PtdIns	phosphatidylinositol
PtdIns(3)P	phosphatidylinositol 3-phosphate
PtdIns3K	phosphatidylinositol 3-kinase
PTM	post-translational modification
PTS	peroxisomal targeting signal
PVDF	polyvinylidenfluorid
qRT-PCR	real-time quantitative reverse transcription PCR
RA	right arm (in knock-out targeting constructs)
Rapamycin	macrolide from Streptomyces hygroscopicus (alternative: Sirolismus)
Raptor	regulatory associated protein of mTOR
RARG	gene encoding for retinoic acid receptor gamma
RAV-1	Rous associated virus 1
RB1CC1	retinoblastoma 1-inducibe coiled-coil 1
Rheb	Ras homolog enriched in brain
Rictor	rapamycin insensitive companion of mTOR
RNA	ribonucleic acid
RNAse	ribonuclease
ROS	reactive oxygen species
RP	reversed-phase
RPMI	Roswell Park Memorial Institute
rRNA	ribosomal RNA
RT	reverse transcription or room temperature
RXR	retinoic X receptor (gene or protein)
SDS	sodium dodecylsulfate

SEM	standard error of the mean
SESN1/2	sestrin 1/2 (gene or protein)
siRNA	small interfering RNA
SLIC	sequence and ligation independent cloning
SNAP29	synaptosomal-associated protein 29
SNARE	soluble N-ethylmaleimide-sensitive-factor attachment receptor
SQSTM1	Sequestosome-1
STAT2	signal transducer and activator of transcription 2 (gene or protein)
STX17	syntaxin 17
t	time
T	temperature
TAE	Tris acetate EDTA buffer
TBS	Tris buffered saline
TEMED	N,N,N',N'-tetramethylethylene-diamine
TFB I/II	transformation buffer I/II
TFEB	transcription factor EB
TGF	transforming growth factor
TLR	Toll-like receptors
T_m	melting temperature
TNF	tumor necrosis factor
Tris	Tris-(hydroxymethyl)-aminomethane
Triton X-100	4-(2',2',4',4'-tetramethylbutyl)phenyldecaethylene-glycolether
TSC1/2	tuberous sclerosis 1/2 (gene or protein)
Tween 20	polyoxyethylene (20) sorbitan monolaurate
ULK1/2/3/4	Ser/Thr kinase UNC-51-like kinase 1/2/3/4 (gene or protein)
UV	ultraviolet
UVRAG	UV radiation resistance associated gene (gene or protein)
v.	version
v/v	volume per volume
VAMP8	vesicle-associated membrane protein 8
VLDL	very-low-density lipoproteins

VSV-G	vesicular stomatitis virus glycoprotein
w/o	without
w/v	weight per volume
WAT	white adipose tissue
WDR45	gene encoding for WD repeat domain phosphoinositide-interacting protein 4
WIPI	WD repeat domain phosphoinositide-interacting protein
WT	wild-type
x	times (multiplication)
X-Gal	5-bromo-4-chloro-3-indoxyl-β-D-galactopyranoside
ZKSCAN3	zinc-finger protein with KRAB and SCAN domains 3
λPP	lambda protein phosphatase

Prefixes

p (pico)	10^{-12}
n (nano)	10^{-9}
µ (micro)	10^{-6}
m (milli)	10^{-3}
c (centi)	10^{-2}
k (kilo)	10^{3}
M (mega)	10^{6}

Units

s	second	Da	Dalton
min	minute	V	volt
h	hour	A	ampere
g	gram or local gravity	pH	$-\log10(a_{H+})$
L	liter	°C	degree Celsius
M	molar (mole/L)	rpm	rounds per minute
U	enzyme unit	Pa	pascal
psi	pounds per square inch		

Amino acids

	single-letter	three-letter code
Alanine	A	Ala
Cysteine	C	Cys
Aspartic acid	D	Asp
Glutamic acid	E	Glu
Phenylalanine	F	Phe
Glycine	G	Gly
Histidine	H	His
Isoleucine	I	Ile
Lysine	K	Lys
Leucine	L	Leu
Methionine	M	Met
Asparagine	N	Asn
Proline	P	Pro
Glutamine	Q	Gln
Arginine	R	Arg
Serine	S	Ser
Threonine	T	Thr
Valine	V	Val
Tryptophan	W	Trp
Tyrosine	Y	Tyr

Deoxyribonucleotides

		single-letter code
2’-Deoxyadenosine 5‘-monophosphate	dAMP	A
2’-Deoxycytidine 5‘-monophosphate	dCMP	C
2’-Deoxyguanosine 5‘-monophosphate	dGMP	G
2‘-Deoxythymidine 5‘-monophosphate	dTMP	T

1 Summary

Autophagy is a lysosomal degradation pathway that maintains cellular homeostasis by removal of protein aggregates or damaged organelles. The dysregulation or selective forms of autophagy have been linked to several human maladies, encouraging research to focus on a detailed elucidation of the underlying autophagy signaling pathways. This work contributes to a better understanding of the role of the class III PtdIns3K complex during autophagy induction and its crosstalk to the other autophagy-initiating ULK1 complex.

Here, nuclear receptor-binding factor 2 (NRBF2) could be identified as a novel PtdIns3K complex protein interacting with Beclin 1 (BECN1). Cellular knockout experiments using the DT40 system characterized NRBF2 as a positive regulator of the autophagic flux.

The extensive crosstalk between the ULK1 complex and the PtdIns3K complex is well documented. Here, NRBF2 was identified as further target of ULK1, harboring multiple ULK1-specific phospho-acceptor sites. Identification of corresponding amino acids was achieved by mass spectrometry and was validated in intact cells. Further experiments using phospho-mimicking mutations revealed an interference of phosphorylated NRBF2 with PtdIns3K complex I assembly, which excludes ATG14 from the PtdIns3K core complex. The general autophagic capacity is not affected, whereas the specific phosphatidylinositol 3-kinase catalytic subunit type 3 (PIK3C3) activity is positively regulated by phosphorylated NRBF2 following starvation conditions. This assigns a role to NRBF2 in fine-tuning the PIK3C3 activity, possibly by priming the PtdIns3K complex I for activation upon starvation.

Apart from its regulatory function during autophagy, NRBF2 comprises autophagy independent functions and is involved in the regulation of peroxisome proliferator-activated receptor (PPAR)-dependent gene expression. NRBF2 interacts with PPAR alpha and displays a weak constitutive nuclear localization. Pharmacological activation of the PPAR isoforms alpha, beta/delta or gamma induced NRBF2-dependent upregulation of cellular ULK1 and LC3-II protein levels. Microarray experiments revealed the general involvement of NRBF2 in gene expression under growth and starvation conditions. Several transcription factors and genes related to immunological processes were identified to be regulated by NRBF2-deficiency. NRBF2-dependent gene expression following PPAR stimulation displayed only weak effects, nevertheless revealing a contrary and NRBF2-dependent regulation of *Ppara* itself and of its heteromeric interaction partner *Rxra*. Additionally, opposed effects were observed for activation of PPAR alpha and the two other

PPAR family members beta/delta and gamma. In summary, NRBF2 represents a central regulator of both autophagy and PPAR-dependent gene expression.

1.1 Zusammenfasssung

Autophagie beschreibt einen katabolischen Prozess und ist für die Aufrechterhaltung der zellulären Homöostase durch den lysosomalen Abbau von Proteinaggregaten oder geschädigten Zellorganellen verantwortlich. Dysregulationen oder selektive Formen der Autophagie wurden unlängst mit verschiedenen menschlichen Erkrankungen in Verbindung gebracht, was die Notwendigkeit einer detaillierten Aufklärung der zugrundeliegenden Signalwege verdeutlicht. Diese Arbeit trägt zu einem besseren Verständnis der Rolle des Klasse III PtdIns3K-Komplexes während der Initiationsphase der Autophagie und der Vernetzung mit dem weiteren Autophagie-initiierenden ULK1-Komplex bei.

Im Rahmen dieser Arbeit konnte der *nuclear receptor-binding factor 2* (NRBF2) konnte als bisher unbekannter Interaktionspartner von Beclin 1 (BECN1) und somit als Bestandteil des PtdIns3K-Komplexes identifiziert werden. Durch Etablierung eines zellulären *Knockouts* im DT40-System wurde NRBF2 als positiver Regulator autophagischer Prozesse charakterisiert. Die starke Vernetzung zwischen dem ULK1-Komplex und dem PtdIns3K-Komplex ist hinlänglich bekannt. Im Zuge dieser Arbeit wurde NRBF2 als weiteres Substrat von ULK1 identifiziert, welches mehrere ULK1-spezifische Phosphorylierungsstellen aufweist. Die Identifizierung der entsprechenden Aminosäuren erfolgte mittels Massenspektrometrie und konnte darüber hinaus in intakten Zellen validiert werden. Durch weitere Experimente mit einer NRBF2-Version, welche einen konstitutiv phosphorylierten Zustand simuliert, konnte eine Beeinträchtigung der PtdIns3K-Komplex I-Zusammensetzung durch phosphoryliertes NRBF2 festgestellt werden, wobei ATG14 aus dem Komplex ausgeschlossen wird. Dies hat keine Beeinflussung der generellen autophagischen Kapazität zur Folge, jedoch wird die spezifische *phosphatidylinositol 3-kinase catalytic subunit type 3* (PIK3C3)-Aktivität durch phosphoryliertes NRBF2 in Folge von Hungerbedingungen positiv reguliert. Somit übernimmt NRBF2 eine Feinregulierung der PIK3C3-Aktivität, welche eventuell als Vorbereitung des PtdIns3K Komplexes für die Aktivierung in Folge von Hungerbedingungen dient.

Neben der regulatorischen Funktion innerhalb der zellulären Autophagie weist NRBF2 weitere, Autophagie-unabhängige Funktionen auf und ist an der Regulation der *Peroxisome proliferator-activated receptor* (PPAR)-abhängigen Genexpression beteiligt. NRBF2 interagiert mit PPAR alpha und zeigt eine schwache, konstitutive Kernlokalisation. Außerdem bewirkt eine pharmakologische Aktivierung von PPAR alpha, beta/delta oder gamma die Erhöhung der zellulären ULK1 und LC3-II Proteinmengen in Abhängigkeit von NRBF2. Durch *Microarray*-Experimente konnte zudem gezeigt werden, dass NRBF2 allgemein an der Genexpression unter Wachstums- oder Hungerbedingungen beteiligt ist. Dabei wurden durch NRBF2-Defizienz mehrere Transkriptionsfaktoren und Gene, welche mit immunologischen Prozessen in Zusammenhang stehen, reguliert. PPAR-Stimulation zeigte generell nur schwache Effekte bezüglich einer NRBF2-abhängigen Genexpression, jedoch wurde eine entgegengesetzte und NRBF2-abhängige Regulation von *Ppara* selber und dem heteromeren Komplex-Partner *Rxra* festgestellt. Zusätzlich wurden für die Aktivierung von PPAR alpha und der zwei weiteren PPAR-Familien Mitglieder beta/delta und gamma teilweise entgegengesetzte Regulationseffekte beobachtet. Zusammenfassend stellt NRBF2 einen zentralen Regulator sowohl der Autophagie als auch der PPAR-abhängigen Genexpression dar.

2 Introduction

2.1 Autophagy

Autophagy is one of the two cellular processes responsible for the degradation of intracellular material. Besides the ubiquitin proteasome system, which mediates the selective breakup of proteins marked for degradation, autophagy is a catabolic process for the breakup and recycling of intracellular material. In doing so, it keeps the cellular homeostasis and fulfills cytoprotective functions by removal of long-lived or damaged organelles and aggregated or misfolded proteins. Although autophagic processes occur on a basal level in every cell, the molecular machinery of autophagy can be actively induced by various stress conditions like nutrient deprivation, growth factor depletion, hypoxia or pathogen infections. This adaption ensures a sufficient supply of energy or amino acids for further protein synthesis thereby guaranteeing cellular survival.

Over 60 years ago, in 1955, Christian de Duve and colleagues identified a new subset of cellular compartments, containing a high number of hydrolytic enzymes: the lysosomes [1]. This discovery was the foundation of a new field of research and it was again de Duve, who observed the sequestration and subsequent delivery of intracellular material to these newly identified organelles for degradation, ultimately discovering a novel catabolic cellular process which he later on termed autophagy, originating from the Greek meaning “self-eating” [2]. The great medical importance of cellular autophagy, which up to nowadays resulted in the awarding of two Nobel Prizes in Physiology or Medicine, could not be estimated at that time point and nearly 30 years passed by without any major achievements. Finally, Yoshinori Ohsumi identified 15 autophagy-related proteins (Atgs; ATGs in mammals) which are essential for the process of autophagy in yeast [3]. These findings initiated a new enthusiasm for the detailed elucidation of the molecular machinery controlling autophagy. Nowadays it is known that functional autophagy is involved in immunological processes and supports physical health whereas dysregulation is linked to various diseases like cancer or neurodegenerative disorders (reviewed in [4]).

2.1.1 Types and morphology

Three distinct types of autophagy exist. Chaperone-mediated autophagy (CMA) is characterized by the selective recognition of proteins containing the KFERQ-motif via the cytosolic chaperone heat shock-cognate protein of 70 kDa (HSC70) and their active transport directly into the lysosomal lumen by lysosome-associated membrane protein 2 A (LAMP2A) (reviewed in [5]). Microautophagy describes the direct invagination of the lysosomal membrane and the uptake and subsequent degradation of small cytosol portions [6]. Macroautophagy (which will be referred to as autophagy from now on) is the last and best-studied type of autophagy. There, specialized double membrane vesicles termed autophagosomes engulf cytosolic portions, which are then transported to lysosomes. After fusion of these two vesicles, the cargo and the inner membrane of the newly formed autolysosomes are degraded. The degradation products are released back into the cytosol to fuel anabolic processes [7]. Besides this unselective form of bulk degradation, also specialized forms of selective autophagy exist to enable the targeted degradation of certain organelles (e.g. mitophagy, pexophagy or ribophagy, which represent the selective degradation of mitochondria, peroxisomes or ribosomes, respectively), cellular pathogens (xenophagy) or lipid droplets (lipophagy) [8,9].

The lifespan of an autophagosome, which is the prominent structural feature of autophagy, comprises several stages: nucleation, expansion, maturation and degradation. The nucleation occurs at the phagophore assembly site (PAS), a certain subcellular compartment, which locates to subdomains of the endoplasmic reticulum (ER) and mitochondria contact sites [10,11]. The emerging isolation membranes (IM) protrude into the cytosol and due to their morphology were termed omegasomes [12]. A delivery of additional lipids from various cellular compartments (e.g. plasma membrane, endosomes, Golgi network or nuclear membrane) enables a constant elongation of these membrane structures and a spherical growth around cytosolic cargo, ultimately resulting in the closure and thus the birth of an autophagosome [13]. During the maturation step, most of the associated proteins involved in formation and elongation are stripped off. These vesicles are then transported along microtubules until they meet their end by fusion with lysosomes [14].

The research performed by Ohsumi intensified the search for additional proteins involved in the regulation of autophagy and their mammalian counterparts. Recently, Atg41 has been identified in yeast [15]. Most of these yeast Atgs have orthologues in the human system and some even have multiple isoforms. Nevertheless, non-ATGs like mechanistic target of rapamycin (mTOR) or phosphatidylinositol 3-kinase catalytic subunit type 3 (PIK3C3) are also involved in the regulation of autophagic signal transduction.

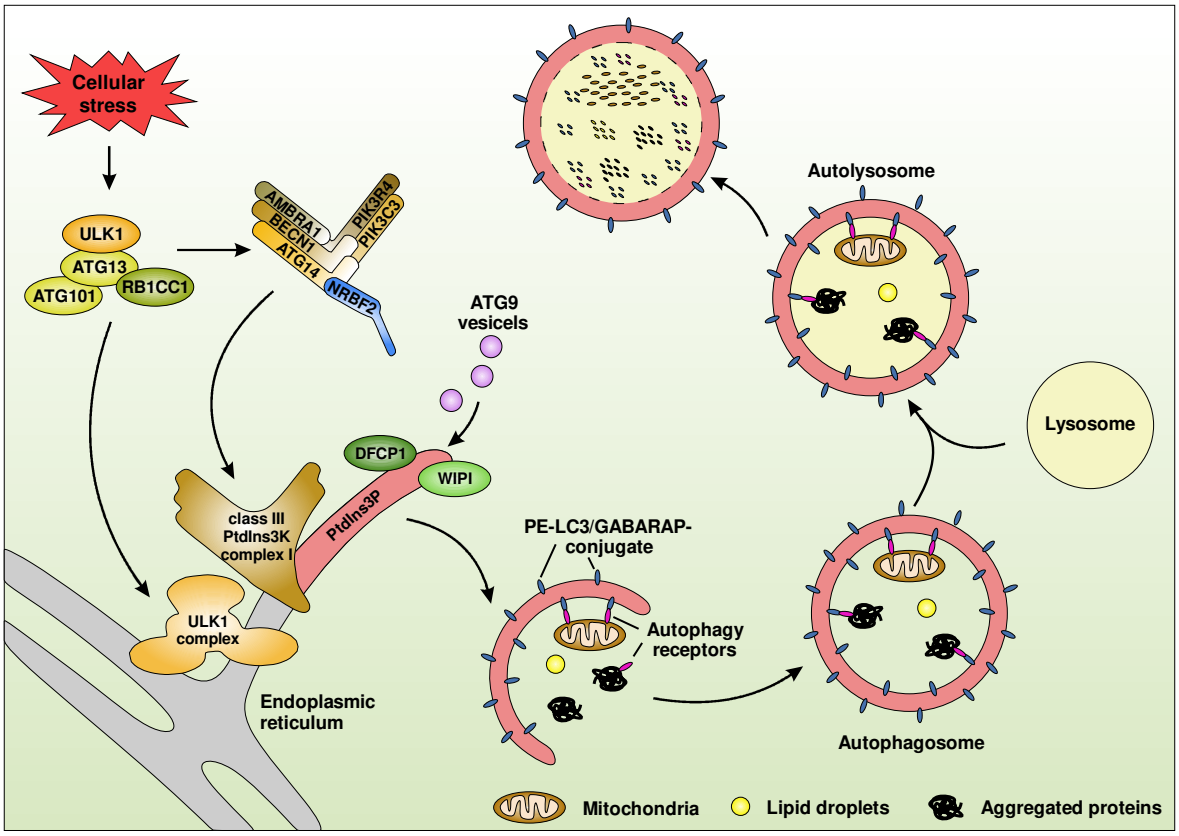

Figure 2.1: Autophagy at a glance. Cellular stress signals (amino acid or glucose starvation, hypoxia or others) activate the ULK1-RB1CC1-ATG13-ATG101 protein kinase complex, which initiates phagophore nucleation by phosphorylation of downstream components of the autophagy signaling pathway like members of the class III PtdIns3K complex I (PIK3C3, BECN1, ATG14, AMBRA1) or LC3/GABARAP. After activation, the ULK1 complex and the PtdIns3K complex I including NRBF2, which was identified as fifth component of the class III PtdIns3K complex (this thesis) relocalize to phagophore assembly sites at the endoplasmic reticulum and initiate the spherical growth of isolation membranes into the cytosol. The PtdIns3K complex I generates PtdIns3P, which enriches at the isolation membranes and recruits the PtdIns3P binding effector proteins DFCP1 or members of the WIPI protein family. ATG9 containing vesicles deliver lipid portions to support membrane elongation. The ubiquitin-like proteins of the LC3 and GABARAP families are conjugated to PE present at the autophagosomal membranes and enable direct cargo-binding or recognition of autophagy receptors. After closure of the membrane structures, the autophagosomes fuse with lysosomes, the sequestered cargo is degraded by hydrolytic enzymes and is released back to the cytosol.

2.1.2 The autophagy signaling pathway

Regarding their different functions and the order of their activation, autophagy related proteins can be classified into five functional groups: 1) the ULK1 kinase complex including ATG13, RB1CC1 and ATG101, 2) the class III PtdIns3K core complex composed of PIK3C3, PIK3R4, BECN1 and additional regulatory proteins, 3) the integral transmembrane protein ATG9, 4) a complex of WIPI proteins with ATG2 and 5) the two ubiquitin-like proteins ATG12 and ATG8-family members and their corresponding conjugation machinery.

2.1.2.1 Induction of autophagy part 1 – the ULK1 complex

In yeast, Atg1 is the only Atg displaying a protein kinase activity. It forms a complex with the associate proteins Atg13 and Atg17 and together they are critically involved in the initiation of autophagy. In higher eukaryotes, the Ser/Thr kinase UNC-51-like kinase 1 (ULK1) was identified as the Atg1 homolog and exists in a stable complex with RB1-inducible coiled-coil protein 1 (RB1CC1, also known as FIP200), the functional counterpart for yeast Atg17, which is thought to have scaffold functions and ATG13, an adaptor protein mediating the ULK1-FIP200 interaction [16]. Unlike in budding yeast, the regulatory protein ATG101 is also part of this complex and presumably functions in the recruitment of further downstream components to the PAS [17] and stabilizes the ULK1 complex [18]. Of note, five Atg1 orthologues have been identified in mammals (ULK1, ULK2, ULK3, ULK4 and STK36), whereas only ULK1 and ULK2 and possibly ULK3 function in the regulation of autophagy [19,20].

The activity of the ULK1 kinase complex is tightly regulated by a network of upstream kinases. Under normal growth conditions, ULK1 is kept in an inactive state by mechanistic target of rapamycin (mTOR), which is why this protein was referred to as the gatekeeper to autophagy. mTOR, the master regulator of cell growth and proliferation, exists in two distinct complexes, which differ in the presence of associated proteins [21]. Only the mTOR complex I (mTORC1), which includes Raptor as additional scaffold protein [22], directly regulates autophagy by association and phosphorylation of several phospho-acceptor sites within ULK1 and ATG13 [23]. Incorporation of Rictor leads to formation of the mTOR complex II (mTORC2), which has distinct cellular functions [24].

Since autophagy can be induced by a variety of stress stimuli, this inhibitory association with mTORC1 can be disrupted by several metabolic relevant kinases. Increasing cellular AMP levels (e.g. as a result of glucose starvation) leads to an activation of AMP-activated protein kinase (AMPK) which in turn inhibits mTORC1 either directly by phosphorylation of Raptor [25] or indirectly by activation of the TSC1/TSC2 complex which in turn inhibits Rheb and thereby mTORC1 [26]. Additionally, AMPK is able to circumvent mTORC1 and directly phosphorylate and activate ULK1 [27] and other downstream components of the autophagy signaling network (e.g. PIK3C3 and BENC1) [28,29]. Apart from the regulation by AMPK, the TSC1/TSC2 signaling node is crucial for the integration of other stress signals like hypoxia, growth factor withdrawal or insulin signaling. In these cases, TSC1/TSC2 is either activated by REDD1 or released from inhibitory effects of ERK1/2 or AKT, respectively [30–32]. Moreover, a very well established model for the induction of autophagy is amino acid starvation via the Rag proteins, a family of small guanosine triphosphatases (GTPases), which activate mTORC1 in response to amino acids [33]. Ultimately, the immunosuppressive drug rapamycin can directly bind and inactivate mTORC1 and thereby induce autophagy [34].

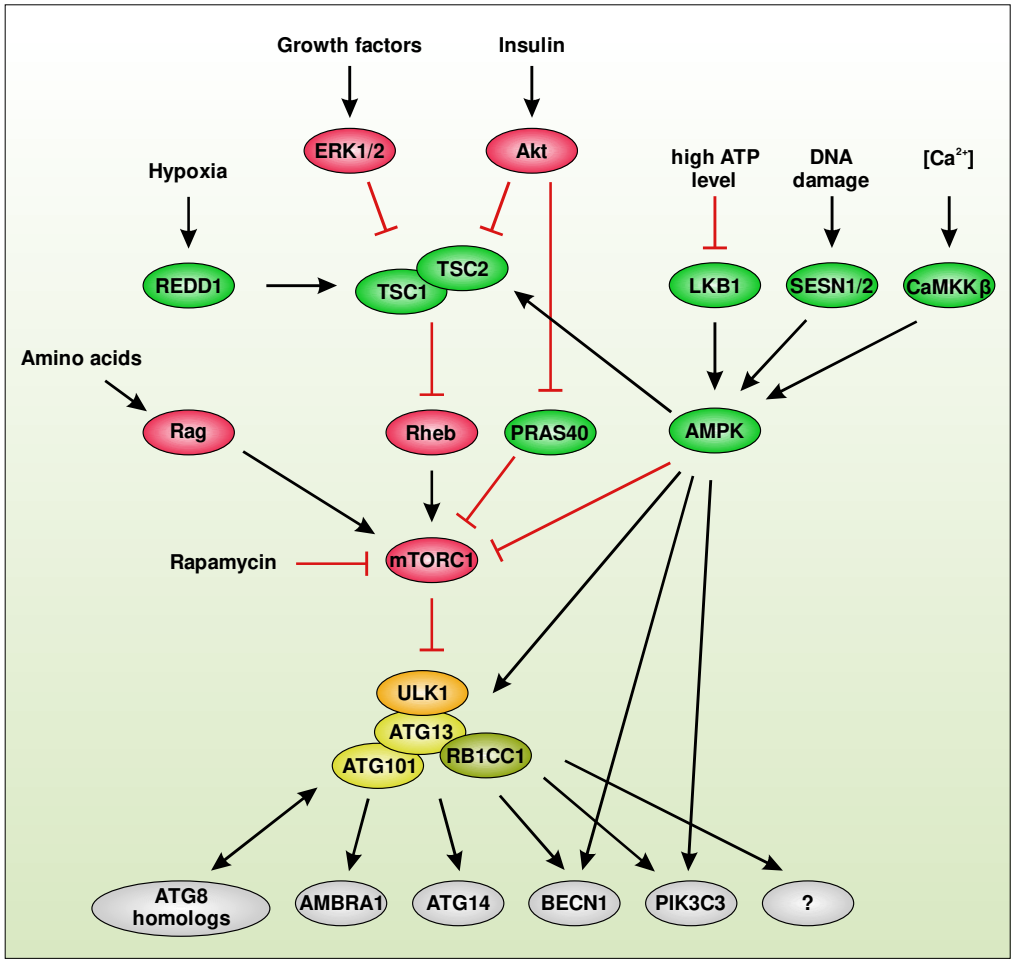

Figure 2.2: Cellular stress factors and their impact on autophagy. The activity of the autophagy-initiating ULK1 complex is tightly regulated by several metabolic signaling pathways. Under growth conditions, mTORC1 binds and inactivates the ULK1 complex. mTORC1 activity is stimulated either by amino acid levels via Rag proteins, by growth factors via ERK1/2 or insulin signaling via Akt. Low cellular ATP levels, DNA damage or Ca^{2+} signaling can activate AMPK via LKB1, SESN1/2 or CaMKKβ, respectively. In turn, AMPK can inactivate mTORC1 either directly or via activation of the TSC1/TSC2 complex. Additionally, AMPK can directly phosphorylate and thereby activate ULK1 or the downstream components BECN1 and PIK3C3. Furthermore, mTORC1 can be inactivated via REDD1 after hypoxic conditions or by direct binding of pharmacologic compounds like rapamycin. Once activated, the ULK1 complex phosphorylates further downstream components of the autophagy signaling network and initiates autophagy. (modified from the postdoctoral thesis (Habilitation) of Prof. Dr. Björn Stork)

All the above-described signal cascades lead to the inhibition of mTORC1 and the removal of inhibitory ULK1 and ATG13 phosphorylations. In turn, ULK1 autophosphorylates and transphosphorylates ATG13 and RB1CC1, ultimately resulting in the complete activation of the ULK1 kinase complex [35].

Several downstream components of the autophagy signaling network have been identified to be ULK1 substrates, thereby promoting the induction of autophagy. Among them are several members of the PtdIns3K complex. Phosphorylation of Beclin 1 (BECN1) is required for PIK3C3 activation [36], whereas the function of direct PIK3C3 phosphorylation remains elusive [37]. In addition, phosphorylation of Beclin 1-associated autophagy-related key regulator (Barkor/ATG14) increases PtdIns3K complex activity and promotes autophagy [38]. Finally, phosphorylation of activating molecule in BECN1-regulated autophagy 1 (AMBRA1) controls the dissociation of the AMBRA1-containing PIK3C3-BECN1 complex from the dynein motor complex and allows relocalization to the PAS [39]. ATG9 can also be phosphorylated by ULK1, promoting vesicle trafficking in response to starvation [40].

In addition, selective forms of autophagy can be controlled by ULK1. Accordingly, proteotoxic stress induces ULK1-mediated Sequestosome-1 (SQSTM1/p62) phosphorylation and autophagic clearance of protein aggregates [41]. Furthermore, ULK1 is able to promote mitophagy by the phosphorylation of FUN14 domain-containing protein 1 (FUNDC1) and thereby increase its binding to microtubule-associated proteins 1A/1B light

chain 3B (MAP1LC3B, short LC3B) [42]. As a feedback mechanism, also Raptor becomes phosphorylated during starvation conditions thereby inhibiting mTORC1 activity [43].

Following its activation, the ULK1 complex itself translocates to the PAS to participate in the maturation process of autophagosomes. How exactly ULK1 is recruited is not entirely clear. Several studies reveal a role for the ATG8 family members LC3B, GATE-16 and Gamma-aminobutyric acid receptor-associated protein (GABARAP), with strong preference for the latter one, which can target ULK1 to emerging isolation membranes via interacting with the LC3-interacting region (LIR) domain [44,45]. Recently, a positive regulation of autophagy by redistribution of centrosomal GABARAP to phagophores was identified and supports this theory [46].

2.1.2.2 Induction of autophagy part 2 – the class III PtdIns3K complex

Besides the ULK1 protein kinase complex, a second initiator complex controls the induction of autophagy: the class III PtdIns3K complex. The catalytic active component VPS34 in yeast or its mammalian homolog PIK3C3, is the only known class III PI3-kinase and was identified to regulate membrane trafficking and endosome to lysosome sorting [47]. The intracellular membrane location of the complex is mediated by the N-terminally myristoylated adaptor protein VPS15 (phosphoinositide 3-kinase regulatory subunit 4 (PIK3R4) in mammals) [48]. In combination with the scaffold protein Atg6 (BECN1 in mammals) these three proteins form the class III PtdIns3K core complex. Depending on the integration of additional regulatory proteins, the PtdIns3K complex can be further divided into two sub complexes comprising different cellular functions and localization. Binding of Atg14/ATG14 and Atg38 (nuclear receptor-binding factor 2 (NRBF2) in mammals) defines the PtdIns3K complex I, which is required for the formation of autophagosomes during early stages of autophagy [49]. In this thesis and by other research groups, NRBF2 was identified as a fifth constitutive subunit of complex I. It interacts with both the VPS34/PIK3C3-VPS15/PIK3R4 and the Atg6/BECN1-Atg14/ATG14 sub complexes and via dimerization of two Atg38 monomers a functional complex I is assembled. Accordingly, Atg38 deficiency causes disintegration of these two sub complexes. Interaction with Atg14, but not with VPS34 is mediated via an N-terminal MIT domain in Atg38 [50]. In budding yeast, the C-terminal dimerization domain of Atg38 was

also found to mediate membrane localization of the PtdIns3K complex I [51]. In contrast, dimers of the eukaryotic Atg38 homolog NRFB2 are able to bridge two units of the PtdIns3K complex I, thereby enhancing PIK3C3 activity up to 10-fold [52]. Nevertheless, also oligomers of a single complex I bound to one NRBF2-dimer exist, depending on the relative abundance of both complexes [51]. These findings were confirmed by studies investigating the role of NRFB2 during autophagy, assigning a positive regulatory function to NRBF2 on the simulation of PIK3C3 activity in response to stress conditions [53,54]. Controversially to these studies, negative regulatory activity of NRBF2 on autophagy was reported as well [55]. In contrast, complex II involves VPS38 (UV radiation resistance associated gene (UVRAG) in mammals). This complex associates with Rab9-positive endosomes and regulates endosomal trafficking and lysosomal fusion [49,56]. The interactions of ATG14 or UVRAG are mutually exclusive due to their overlapping binding regions in BECN1 [57]. Besides this conserved complex architecture, some differences between yeast and eukaryotic cells can be found. In mammals, the PtdIns3K complex I temporally interacts with AMBRA1, causing subsequent relocalization to the PAS [39]. Additionally, some evidence exists for the involvement of complex II in early stages of autophagosome biogenesis [58]. Situational, other proteins were found to transiently interact with the class III PtdIns3K complex, enabling a temporal activity regulation. The interaction of anti-apoptotic Bcl-2 family members with BECN1 is of high physiologic relevance [59], since it links an important autophagy signaling node to the apoptosis pathway. Binding of Bcl-2 is able to segregate BECN1 from the class III PtdIns3K complex and thereby inhibits PIK3C3 activity and suppresses autophagy [60]. Phosphorylation of either Bcl-2 by c-Jun N-terminal protein kinase 1 (JNK1) [61] or of BECN1 by death-associated protein kinase (DAPK) [62] leads to the disruption of the BECN1-Bcl-2 interaction and stimulates autophagy, whereas phosphorylated Bcl-2 itself in combination with Bax inhibits apoptosis [63]. This crosstalk of autophagy and apoptosis further encompasses many critical ATGs (BECN1, SQSTM1, ATG3, ATG7), which can be cleaved by activated caspases for the inactivation of their autophagic functions [64–67].

Additionally, the class III PtdIns3K complex can directly be inhibited or activated by several growth or stress signals. Under growth conditions both, AKT and epidermal growth factor receptor (EGFR) phosphorylate BECN1 and inhibit autophagy [68,69]. Cellular stress in turn can activate the class III PtdIns3K complex via several pathways. The direct phosphorylations of

BECN1 by ULK1 or AMPK have already been discussed [29,36]. Additionally, the two members of the p38 mitogen-activated protein kinase (MAPK) pathway MAPKAPK 2 and 3 have been shown to positively regulate autophagy by phosphorylation of BECN1 [70]. Once activated, the class III PtdIns3K complex I catalyzes the generation of PtdIns3P out of PtdIns, which enriches in the nascent isolation membranes and recruits further downstream effector proteins [12].

2.1.2.3 Closure, maturation and degradation of autophagosomes

DFCP1 or Atg18 family members are PtdIn3P effector proteins by recruitment to emerging autophagosomal membrane structures. DFCP1 is able to bind PtdIns3P through interaction with its FYVE-domain and thereby localizes to omegasomes [12]. WD repeat domain phosphoinositide-interacting proteins (WIPI) are the human Atg18 homologs. So far, four members have been identified (WIPI 1-4), albeit only WIPI1 and 2 are involved in autophagosome biogenesis and localize to isolation membranes via their seven-bladed β-propeller, which enables PtdIns3P binding [71]. The complex of WIPI proteins and ATG2 enables the subsequent recruitment of Atg8 family members to the emerging isolation membranes [72].

During the expansion phase of autophagosomal membranes, a continuous transport of lipids from various cellular compartments, like recycling endosomes, early endosomes, late endosomes or the trans-Golgi network occurs [73,74]. At these vesicles, the transmembrane protein ATG9 can be found, which shuttles between cellular lipid reservoirs and the emerging autophagosomal membranes and supports their elongation without being incorporated into the isolation membranes itself [73].

The two ubiquitin-like ATG12-ATG5 and ATG8-phosphatidylethanolamine (PE) conjugation systems are centrally involved in the expansion processes of autophagosomal membranes [75] and presumably mediate the sealing of autophagosomes [76]. In eukaryotic cells nine homologs of yeast Atg8 have been identified, which can be further divided into the LC3 (LC3A (two isoforms), B, B2, C) and the GABARAP (GABARAP, GABARAPL1, 2, 3) subfamily [77]. In the first pathway, the ubiquitin-like ATG12 is activated by the E1-like enzyme ATG7 and transferred to the E2-like enzyme ATG10 before it is finally conjugated

to ATG5. This ATG12-ATG5 conjugate possess E3-like activity, which is needed for the second conjugation cascade. Therefore, homo-oligomerization with ATG16L and subsequent relocalization to autophagosomal membranes via interaction of ATG16L and WIPI proteins are necessary requirements. Nascent pro-ATG8s are C-terminally cleaved by ATG4 to expose a terminal glycine residue, which will be conjugated to PE later on. Again, an activation step by the same E1-like enzyme ATG7 occurs, followed by the transfer to the E2-like ATG3. The final conjugation to PE at the autophagosomal membranes is now performed by the E3-like activity of ATG12-ATG5 conjugate (reviewed in [16]).

Beside their function in autophagosome expansion, the ATG8-PE conjugates mediate recognition and recruitment of cytosolic substrates by interacting with LIR domains of cargo receptors needed for selective forms of autophagy. Autophagy receptors like SQSTM1/p62, neighbor of BRCA1 gene 1 (NBR1) or optineurin (OPTN) in turn can interact with ubiquitinated proteins, thereby linking them to autophagosomal membranes [78–80].

After sequestration of the cytosolic cargo by fusion of the autophagosomal membranes, the autophagosomes undergo a maturation processes. Thereby ATGs present at the outer autophagosomal membrane are cleared and the autophagosomes are transported along microtubule structures towards the lysosome [81]. The fusion process is mediated by the soluble N-ethylmaleimide-sensitive-factor attachment receptor (SNARE) proteins syntaxin 17 (STX17) and synaptosomal-associated protein 29 (SNAP29) on the autophagosomal membranes and vesicle-associated membrane protein 8 (VAMP8) on the lysosomal membrane [82].

This way, the lifespan of the autophagosome ends by the rise of the autolysosome and the degradation of autophagosomal cargo by lysosomal hydrolases.

2.1.3 Implications of autophagy in health and disease

In healthy individuals, autophagy is executed on a normal/basal level, which is responsible for maintenance of cellular homeostasis. The positive influence of physical activity and regular exercise on general health is associated with a stimulation of basal autophagy rates [83]. Similarly, a decrease in autophagic capacity is well documented during aging [84].

Recently, the dysregulation of autophagy could be linked to various human diseases from neurodegeneration to cancer or immunological disorders, which will be summarized in the following chapters.

2.1.3.1 Autophagy and neurodegenerative diseases

The most common forms of neurodegeneration like Alzheimer disease, Parkinson disease or Huntington disease share one specific characteristic: the accumulation and aggregation of misfolded proteins, which affects the cellular functions of neuronal cells (reviewed in [85]). Under normal conditions, the ubiquitin proteasome system is the main degradation pathway for aggregated proteins, supported by autophagic degradation processes. Thereby, a key position in recognition of ubiquitinated proteins is assigned to the autophagy receptor p62/SQSTM1 [86].

Additionally, impaired mitochondrial function and the resulting increase in cellular reactive oxygen species (ROS) level has been identified as another frequent cause of neurodegenerative disorders. Accordingly, mutations of PTEN-induced putative kinase 1 (PINK1) and Parkin, which specifically label damaged mitochondria for the selective degradation through mitophagy, can be associated with neurodegenerative disorders [87].

In each case, activation of cellular autophagy is thought to be beneficial for prevention and therapeutic approaches. Therefore, either a pharmacological inhibition of mTOR or an activation of AMPK are currently explored [88,89].

2.1.3.2 Autophagy and cancer

The general and close connection of the autophagy signaling pathway and oncogenic signaling can be deduced from the inhibiting influence of activated oncogenes like AKT or mTOR on autophagy. Additionally, several ATGs have tumor suppressive functions. Accordingly, BECN1 was identified to act as tumor suppressor [90] and is frequently monoallelically deleted in up to 75% of several cancer types like breast, ovarian and prostate cancer [91].

Unlike for neurodegenerative disorders, the role of autophagy in cancer has to be evaluated in the specific context. In general, the cytoprotective functions of autophagy are thought to prevent the formation of cancer, whereas suppression of autophagic capacity is associated with a high risk in cancer development [92]. Once a tumor is manifested, autophagy presumably supports energy supply by its cytoprotective function and attenuates therapy efficiencies [93]. Accordingly, it could be shown that certain types of cancer strongly depend on autophagy [94]. Moreover, the activation of autophagy occurs as a side effect of several cancer therapies [95].

Consequently, inhibition of autophagy by pharmacological compounds currently attracts great attention. However, some reports describe positive results through activation of autophagy with regard to recruitment and recognition of immune cells [96].

Furthermore, additional factors can influence the physiological outcome of targeted modulation of autophagy. In a mouse model of pancreatic ductal adenocarcinoma (PDAC) inhibition of autophagy in the presence of p53 prevents tumor formation, whereas tumor growth is accelerated by autophagy inhibition in the absence of p53 [97].

The fact that autophagy is involved in the shaping of tumor microenvironment by secretion of exosomes containing cytosolic proteins like IL-6, lipids, RNA or DNA underlines the importance for a targeted modulation [98,99]. Furthermore, autophagy is thought to downregulate various transcription factors related to epithelial-mesenchymal transition (EMT), a way for adherent cells to acquire motility and thereby metastatic potential, thereby hindering this process [100]. Moreover, autophagy generally affects cell migration. On the one hand increased turnover and remodeling of focal adhesions supports motility and on the other hand degradation of proteins controlling actin dynamics inhibits cell migration [101,102].

Since autophagy can support and impede cancer progression, medical therapies designed to either activate or inhibit autophagy are possible, depending on the specific situation. However, inhibition of autophagy seems to be commonly applicable and therefore currently attracts more attention. Chloroquine (CQ) and hydroxychloroquine (HCQ) prevent lysosomal acidification and thereby inhibit autophagic turnover [103]. These

compounds were originally used for the treatment of malaria and meanwhile have been applied successfully in several phase 2 clinical trials for therapy of various types of cancer [96].

2.1.3.3 Autophagy and immunological processes

The involvement of autophagy in immunological processes was excessively shown and was termed "immunological autophagy" as it refers to the involvement of autophagic processes in innate or adaptive immune responses. It is of importance for the secretion of pro-inflammatory cytokines, antigen presentation via the major histocompatibility complex (MHC) class I and II, the removal of intracellular bacteria and lymphocyte development [104,105]. Furthermore, attenuations of autophagic capacity can be related to autoimmune diseases like multiple sclerosis or diabetes type 2 [106].

The selective removal of various cellular pathogens like *Salmonella typhimurium* is termed xenophagy. Thereby, ubiquitin is attached to invading bacteria, which later on is recognized by autophagy receptors and subsequently results in the degradation of the bacteria, similar to other types of selective autophagy [107]. Of note, some bacteria are able to circumvent their degradation by interfering with autophagosome maturation or block of the autophagosomal-lysosomal fusion [108]. In some special cases, bacteria like *Staphylococcus aureus* have evolved strategies not only to circumvent their autophagic degradation, but to utilize the autophagic vesicles as intracellular transport mechanism for bacterial propagation [109].

Nevertheless, like for neurodegenerative diseases, the induction of autophagy is thought to be beneficial for the therapy of autoimmune diseases or bacterial infections [110].

2.1.4 Transcriptional control of autophagy

The short-term and rapid modulation of the autophagic flux in response to stress periods has already been studied in detail, whereas the long-term transcriptional regulation of autophagy remained largely unexplored until recently. However, the general involvement of transcriptional processes has already been shown in 1999. In yeast, autophagy related genes were upregulated within 30 minutes as response to nitrogen starvation [111]. In the meantime, over 20 transcription factors were linked to the regulation of autophagy related

genes and autophagy itself, but their interconnection remains enigmatic (reviewed in [112]). The following chapter will sum up the transcription cascades found to have a major impact on transcriptional control of autophagy.

The identification of transcription factor EB (TFEB), which is as a master regulator of the lysosomal pathway itself, as regulator of a large set of ATGs involved in all distinct steps of autophagy was a huge achievement on the way of connecting execution and transcriptional control of autophagy [113]. Under growth conditions, TFEB is present in a complex with 14-3-3 proteins as a result of phosphorylation by mTORC1, which prevents its nuclear localization. Upon inhibition of mTORC1 by starvation, TFEB is freed of its inhibitory phosphorylation, translocates to the nucleus and induces transcription of key ATGs like *Atg4*, *Map1lc3b*, *Uvrag*, *Wipi* and genes responsible for lysosomal biogenesis [114]. The zinc-finger protein with KRAB and SCAN domains 3 (ZKSCAN3) acts as counterpart of TFEB and represses transcription of various ATGs like *Ulk1* or *Map1lc3b*. During induction of autophagy, this repression is released by translocation of ZKSCAN3 to the cytosol [115]. Since the mere overexpression of TFEB or the knockdown of ZKSCAN3 is sufficient to induce autophagy, these two transcription factors are currently explored as possible therapy-targets in neurodegenerative diseases that might benefit from autophagy induction [116].

Another family of transcription factors, which was linked to the process of autophagy quite early, are Forkhead box O (FOXO) proteins (FOXO1 and 3). Under growth conditions, the nuclear localization of FOXOs is antagonized by inhibitory phosphorylation events contributed by AKT or occupation of FOXO3 DNA binding sites by activated FOXK1, which in turn is regulated by mTOR. The induction of starvation conditions now reverses these conditions [117]. Again, a large set of core ATGs (*Atg5*, *Atg12*, *Atg13*, *Atg14*, *Becn1*, *Bnip3*, *Map1lc3b*, *Ulk1* or *Pik3c3*) is regulated by members of the FOXO family [118]. Of note, cytosolic FOXO1 is able to induce autophagy independent of its transcriptional function [119].

The transcription factor E2F1 controls the expression of some ATGs like *Atg5*, *Map1lc3b*, *Ulk1* and *Bnip3* [120]. In contrast, nuclear factor kappa-light-chain-enhancer of activated B cells (NF-κB) competes with E2F1 and thereby restricts *Bnip3* expression [121]. Nevertheless, also a positive regulation of ATGs could be shown for NF-κB, as it can regulate expression of *Becn1* and other ATGs [122].

Expression of autophagy receptor *Bnip3*, which is involved in induction of mitophagy or cell death (reviewed in [123]), is induced as response to hypoxia by hypoxia-inducible factor 1 alpha (HIF1 alpha) [124].

The JNK-JUN pathway, which can be activated by several environmental stress conditions or cytokines [125], is also linked to the autophagy pathway. An increased nuclear translocation of JUN as a reaction to starvation periods and an associated elevated transcription of *Becn1* or *Map1lc3b* was observed [126].

Also for the tumor suppressor protein TP53, an association to the promotor regions of various ATG genes (*Atg4*, *Atg7*, *Atg10* and *Ulk1*) has been observed [127].

Very recent findings link the FXR-PPAR alpha-CREB axis of nuclear receptors to the transcriptional control of autophagy in the liver for the first time. Under growth conditions, the farnesoid X receptor (FXR) represses a large set of core ATGs (*Atg3*, *Atg5*, *Atg7*, *Atg10*, *Becn1*, *Gabarap*, *Map1lc3b*, *Ulk1* or *Pik3c3*). The release of this repression can be explained by two separate models. On the one hand, FXR disrupts the functional complex of CRE-binding protein (CREB) and CREB-regulated transcription coactivator 2 (CRTC2). Upon induction of starvation, the CREB-CRTC2 complex assembles and induces transcription [128]. In a second model, peroxisome-proliferator-activated receptor alpha (PPAR alpha) controls transcription of several ATGs, but shares specific DNA-binding regions (DR1 elements) with FXR. Only by starvation these binding regions are released and PPAR alpha may induce transcription [129]. Interestingly, PPAR alpha is also able to induce transcription of *Tfeb*, which itself is a master regulator of transcription of core ATGs [130]. In addition, PPAR gamma could be linked to transcriptional regulation of autophagy, though its function as a positive or negative regulator is still controversially discussed [131,132].

The large number of transcriptional processes activated as response to starvation conditions highlights the increasing importance of transcriptional control of autophagy. How exactly these processes cooperate and if certain pathways are favored awaits further elucidation.

2.2 The PPAR nuclear receptor sub family

Nuclear receptors comprise a large spectrum of cellular functions from metabolic or developmental processes to immune signaling (reviewed in [133]). Three subtypes of nuclear receptors are known. The first class comprises prototypical receptors like steroid hormone receptors, which require ligand binding for activation, the second class encompass the orphan receptors without ligands (because they are either not known or not needed). The PPARs belong to the third class of metabolite-activated nuclear receptors, which form obligatory heterodimers with the retinoic X receptor (RXR). Like all nuclear receptors, PPARs display the typical domain organization of an N-terminal ligand-independent activation function (AF1), a DNA-binding domain (DBD), a variable hinge region, a ligand-binding domain (LBD) and a C-terminal ligand-dependent activation function (AF2) [134]. Three different PPAR family members have been identified: PPAR alpha, beta/delta and gamma. Due to an unusually large ligand-binding pocket, a multitude of substances can serve as endogenous ligands: various fatty acids (unsaturated, saturated or branched-chained), eicosanoids, derivatives of linoleic acid, low-density lipoproteins (LDLs) and very-low-density lipoproteins (VLDLs) [135]. In the absence of ligands, a co-repressor complex (nuclear receptor co-repressor/silencing mediator for retinoid and thyroid hormone receptors, NCoR/SMRT) in association with histone deacetylases (HDACs) and chromatin-modifying enzymes is bound to the receptor dimers to enable repression of target genes. Upon ligand binding a conformational change is initiated, which leads to the exchange of the co-repressor complex for co-activators, the binding of DNA via peroxisome proliferator response elements (PPRE) and the induction of gene transcription. Unlike PPAR alpha and gamma, which are cytosolic complexes in the absence of ligands, PPAR beta/delta is constantly bound to DNA [136].

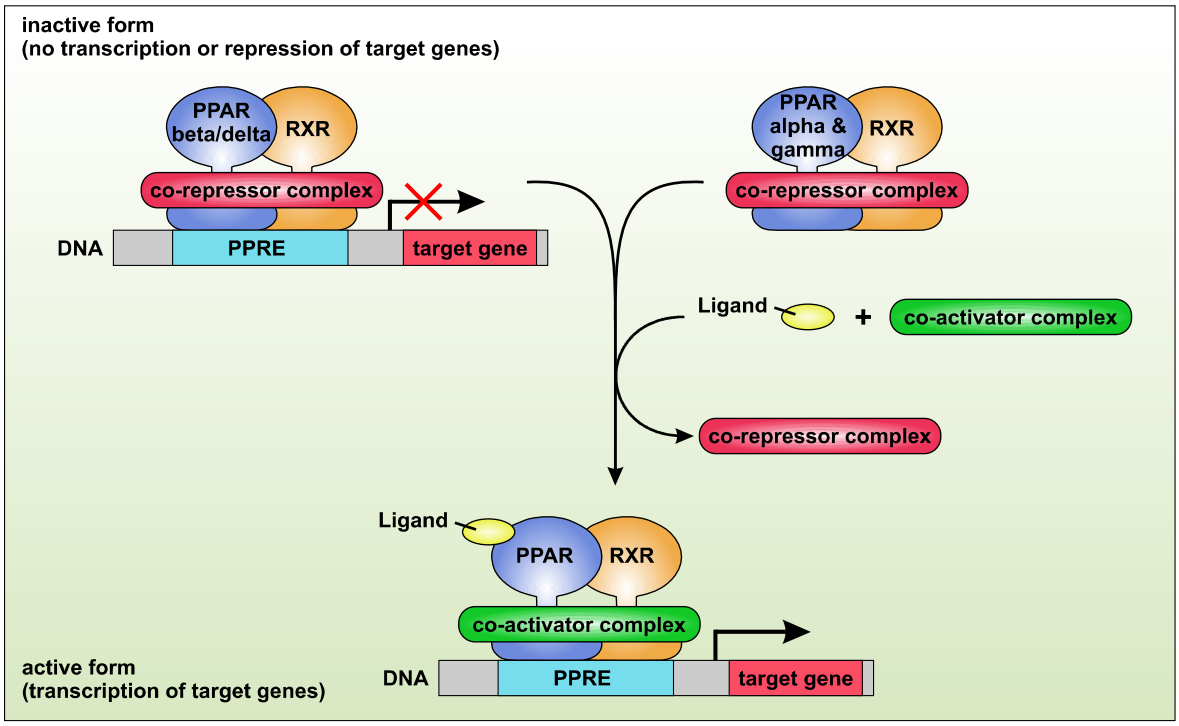

Figure 2.3: Schematic representation of peroxisome proliferator-activated receptors and their function. The three PPAR family members PPAR alpha, beta/delta and gamma form obligate heterodimers with the retinoic X receptor (RX

R). In the unliganded state, binding of a co-repressor complex keeps the PPAR alpha and gamma complex in an inactive form, whereas the PPAR beta/delta complex is constitutively bound to PPAR response elements (PPRE) in the DNA and represses gene transcription. After ligand binding the co-repressor complex is exchanged for a co-activator complex and gene transcription is initiated.

PPAR alpha is expressed in brown adipose tissue (BAT) or metabolically active tissue like in the heart and hepatic tissue [137]. It is a master regulator of energy levels by controlling the cellular and systemic lipid catabolism, fasting responses and the expression of many target genes involved in mitochondrial and peroxisomal β-oxidation of fatty acids [138]. Additionally, PPAR alpha is expressed in a variety of immune cells like lymphocytes, dendritic cells or macrophages and negatively regulates inflammatory responses. Accordingly, activation of PPAR alpha is linked to induction of apoptosis in pro-inflammatory cytokine stimulated macrophages [139]. Due to its global regulation of lipid metabolism, impaired PPAR alpha function can be linked to inflammatory diseases like atherosclerosis [140].

PPAR beta/delta is ubiquitously expressed in many tissues with a considerable strong expression in BAT and muscle fibers. Like PPAR alpha, it controls expression of genes

involved in fatty-acid metabolism and mitochondrial respiration [141]. In BAT, PPAR beta/delta is crucially involved in energy uncoupling and thereby influences maintenance of body temperature [142]. Furthermore, PPAR beta/delta promotes growth of oxidative muscle fibers, which are resistant to high-fat diet induced obesity and display improved insulin resistance. Additionally, PPAR beta/delta confers exercise physiology to muscle fibers and mediates metabolic benefits of exercise training [143]. Some reports link PPAR beta/delta activation to the repression of inflammatory genes in macrophages [144]. Nevertheless, the general involvement in modulation of inflammatory processes remains enigmatic and awaits further elucidation.

PPAR gamma expression is restricted mainly to adipose tissue and is centrally involved during adipocyte differentiation into brown or white adipose tissue (WAT). Interestingly, this function cannot be compensated by the other two PPAR family members [145]. Additionally, PPAR gamma is a target of thiazolidinediones, which are commonly applied for treatment of type 2 diabetes, and mediates increased insulin sensitivity by induction of lipid repartitioning to the adipose tissue [146]. Increased expression of PPAR gamma in non-adipose tissue causes similar lipid deposition like in adipose tissue and is linked to heart or liver malfunctions [146,147]. Besides activation of target genes, absence of ligands transforms PPAR gamma into a major negative regulator of inflammatory gene expression. This process, where repression occurs without any DNA-binding of the nuclear receptor complex is called trans-repression and has emerged as an important mechanism of macrophage differentiation [148].

3 Aims of this work

Autophagy is a process to maintain cellular homeostasis by degradation of harmful protein aggregates and damaged or dysfunctional organelles, which induction is controlled by two multi-protein complexes, the ULK1 protein kinase complex and the class III PtdIns3K lipid kinase complex. Autophagy balances cellular survival via a tightly regulated crosstalk to apoptosis or senescence signaling pathways. Lately, selective forms of autophagy and the general dysregulation of cellular autophagy were linked to several severe human maladies like neurodegeneration, autoimmunity and cancer. In this context, the pharmacological inhibition of autophagic processes has proven a promising option for cancer therapy, indicating its clinical potential and a better understanding of the underlying signaling pathways can enable a more precise interference, e.g. by pharmacological compounds. For clinical research with special regard to the patients who will receive the medication, a minimization of side effects is of great importance. This drives the need for the identification of further, so far unknown and targetable proteins or interaction areas involved in the regulation of the autophagy signaling network.

This work aimed for the identification of novel interacting proteins of the PtdIns3K complex by enrichment of candidate proteins and their subsequent identification by mass spectrometry.

A biochemical validation of putative candidates and a characterization of their roles during autophagy should be performed *in vivo*. The potential crosstalk with the autophagy initiating ULK1 kinase complex and the resulting modulating effects on the PtdIns3K complex and on the general autophagic capacity should be investigated. Furthermore, the identified proteins and their underlying regulation mechanisms should be evaluated for their potential role as target for therapeutic autophagy modulation. In addition, the existence of crosstalk with other cellular metabolic pathways and related autophagy independent functions of the novel PtdIns3K-binding proteins should be explored.

4 Material and Methods

4.1 Materials

All chemicals and biologically reactive reagents were purchased from Carl Roth (Karlsruhe, Germany), Sigma Aldrich (St. Louis, MO, USA), Merck Millipore (VWR, Burlington, MA, USA), Thermo Fisher Scientific (Gibco, Molecular Probes, Waltham, MA, USA), GE Healthcare (Chalfont St Giles, UK). All chemicals were purchased in p.A. quality unless otherwise indicated.

4.1.1 Vectors

Commercial vectors	Application and source
pCR2.1®-TOPO	TA-cloning® of PCR products; Thermo Fisher Scientific
pEGFP-N3	Template of GFP cDNA for BECN1-GFP and GFP expression; Clontech Laboratories
pBluescript SK II (-)	Generation of targeting constructs; Statagene
pHisD, pBleo	Source of resistance cassettes for targeting constructs; Tomohiro Kurosaki (Yokohama, Japan)
pMSCVpuro	Retroviral transduction; Clontech Laboratories
pBABEpuro	Retroviral transduction; Addgene, #1764
pVSV-G	Pseudotyping of retroviral particles; Clontech Laboratories
pGEX-5x3	Expression of GST fusion proteins; GE Healthcare
pET-15b	Expression of 6xHis fusion proteins; Novagene

4.1.1.1 Generated vectors

For the generation of pMSCVpuro-based retroviral expression constructs, total RNA was isolated from HEK293 cells (see 4.2.1.13) and reverse transcribed in total cDNA (see 4.2.1.14). Protein coding cDNAs (BECN1 and NRBF2) were amplified by proof reading polymerase using sequence specific primers (see 4.2.1.16.2). cDNA encoding for human BECN1 was incubated with *Taq* polymerase to generate 3'-adenine overhangs and subsequently used for TA-cloning® into pCR2.1®-TOPO vector (see 4.2.1.17). A 5'-*BglII* restriction site was introduced and the 3'-TGA stop codon was removed by PCR and the PCR product was again introduced into pCR2.1®-TOPO vector via TA-cloning®. Subsequently, cDNA was cloned via *EcoRI* into pEGFP-N3 and the cDNA encoding for BECN1-GFP fusion protein was cloned via *BglII* and *HpaI* into pMSCVpuro. For generation

of pMSCVpuro GFP, cDNA encoding for GFP was excised from pEGFP-N3 via restriction by *BamHI* and *NotI*. 5'-overhangs were filled-in (see 4.2.1.5) and ligated (see 4.2.1.10) into *HpaI* sites of pMSCVpuro. cDNA encoding for human NRBF2 harboring 5'- and 3'-overlap to pMSCVpuro sequences was amplified from reverse transcribed total RNA and directly cloned via SLIC (see 4.2.1.18) into pMSCVpuro. cDNAs encoding for NRBF2 N- or C-terminally fused to GFP were generated by amplification of NRBF2 from pMSCVpuro NRBF2 and of GFP from pEGFP-N3 and combined by SLIC. For generation of pBABEpuro NRBF2, corresponding cDNA was amplified from pMSCVpuro NRBF2 and inserted into pBABEpuro via SLIC. Mutated versions of NRBF2 (S5-A and S5-D) were generated by site-directed mutagenesis (see 4.2.1.16.3) on pBABEpuro NRBF2. N-terminal HA-tag was introduced to respective NRBF2 versions in pBABEpuro via SLIC. For generation of N-terminally HA-tagged NRBF2 versions in pMSCVpuro, corresponding cDNAs were amplified from pBABEpuro vectors and inserted into pMSCVpuro vector via SLIC.

For the generation of NRBF2 targeting constructs, left arm (LA) and right arm (RA) sequences were amplified from DT40 genomic DNA using LA-*Taq* polymerase harboring a *EcoRV* restriction site in between and cloned into pBluescript SK II (-) vector via SLIC using *SpeI* and *SalI* restriction sites located in the multiple cloning site (MCS). Finally, resistance cassettes were excised via *BamHI*, 5'-overhangs were filled-in and cloned via *EcoRV* into pBluescript SK II (-) between the LA and RA. Subsequently, a premature stop codon was introduced by site-directed mutagenesis into exon 2 of the LA.

For generation of bacterial expression vectors, respective cDNAs were transferred to pGEX-5x3 or pET-15b vectors. For pGEX-5x3 NRBF2 WT, internal *BamHI* restriction site of pMSCVpuro NRBF2 WT was removed by site-directed mutagenesis without changing the amino acid sequence of NRBF2. Then, cDNA encoding for NRBF2 was amplified via PCR and 5'-*BamHI* and 3'-*XhoI* restriction sites were introduced. PCR product was directly incubated with restriction endonucleases (see 4.2.1.4) and inserted into pGEX-5x3 via *BamHI* and *XhoI*. NRBF2 WT and 5S-A were transferred to pET-15b vector from corresponding pMSCVpuro vectors via SLIC and restriction by *NdeI*.

Vector	Application
pBluescript NRBF2-HisD	Targeting vector for chicken NRBF2 allele, histidinol resistance cassette
pBluescript NRBF2-Bleo	Targeting vector for chicken NRBF2 allele, bleomycin resistance cassette
pMSCVpuro BECN1-GFP	Stable expression of human BECN1 fused to C-terminal GFP-tag
pMSCVpuro GFP	Stable expression of GFP
pMSCVpuro NRBF2-GFP	Stable expression of human NRBF2 fused to C-terminal GFP-tag
pMSCVpuro GFP-NRBF2	Stable expression of human NRBF2 fused to N-terminal GFP-tag
pMSCVpuro NRBF2 WT	Stable expression of wild-type human NRBF2
pMSCVpuro HA-NRBF2 WT	Stable expression of wild-type human NRBF2 fused to N-terminal HA-tag
pMSCVpuro HA-NRBF2 5S-A	Stable expression of serine to alanine quintuple mutant human NRBF2 fused to N-terminal HA-tag
pMSCVpuro HA-NRBF2 5S-D	Stable expression of serine to aspartate quintuple mutant human NRBF2 fused to N-terminal HA-tag
pBABEpuro NRBF2 WT	Stable expression of wild-type human NRBF2, lower expression levels than pMSCVpuro
pBABEpuro NRBF2 5S-A	Stable expression of serine to alanine quintuple mutant human NRBF2, lower expression levels than pMSCVpuro
pBABEpuro NRBF2 5S-D	Stable expression of serine to aspartate quintuple mutant human NRBF2, lower expression levels than pMSCVpuro
pBABEpuro HA-NRBF2 WT	Stable expression of wild-type human NRBF2 fused to N-terminal HA-tag, lower expression levels than pMSCVpuro
pBABEpuro HA-NRBF2 5S-A	Stable expression of serine to alanine quintuple mutant human NRBF2 fused to N-terminal HA-tag, lower expression levels than pMSCVpuro
pBABEpuro HA-NRBF2 5S-D	Stable expression of serine to aspartate quintuple mutant human NRBF2 fused to N-terminal HA-tag, lower expression levels than pMSCVpuro
pGEX-5x3 NRBF2 WT	Bacterial expression of wild-type human NRBF2 fused to N-terminal GST-tag
pET-15b NRBF2 WT	Bacterial expression of wild-type human NRBF2 fused to N-terminal 6xHis-tag
pET-15b NRBF2 5S-A	Bacterial expression of serine to alanine quintuple mutant human NRBF2 fused to N-terminal 6xHis-tag

4.1.2 Oligonucleotides

All oligonucleotides (primers) for polymerase chain reaction and qRT-PCR used in this thesis were synthesized by Sigma-Aldrich (St. Louis, MO, USA) or Thermo Fisher Scientific (Waltham, MA, USA). Small interfering RNAs (siRNA) were purchased from Dharmacon, GE Healthcare (Lafayette, CO, USA).

Oligonucleotides for amplification of cDNA and genomic DNA

Primer name	5' - 3' sequence
chNRBF2_screening_for	GTGTTGTTTCACAGAGCCCATGCC
chNRBF2_screening_rev	CACCTCTCCTGGATGAGCAGTAAC
HisD_screening_rev	GCCGTGACCCTGCGCGTAAACGCCCTCAAGG
Bleo_screening_rev	CAACTGCGTGCACTTCGTGGCC
hBECN1_for	AAGGATCCGCCGCCACCATGGAAGGGTCTAAGAC
hBECN1_rev	AAGTTAACTCATTTGTTATAAAATTGTGAGG
BENC1+BglII-TGA_for	AAAGATCTGCCGCCACCATGGAAGGGTC
BENC1+BglII-TGA _rev	TTTTTGTTATAAAATTGTGAGGACACCCAAGC
NRBF2_in pGEX-5x3_for	AAGGATCCTGGAAGTAATGGAAGGACCCCTC
NRBF2_in pGEX-5x3_rev	AACTCGAGTTAATTATTCATAAATCCTTTCAGAATATCC

For screening of wild-type, bleo- or hisD-targetet alleles, the forward primer (chNRBF2_screening_for) was combined with respective reverse primer.

Oligonucleotides for SLIC

Primer name	5' - 3' sequence	Restriction site in vector
chNRBF2_LA_for	GAATTGGGTACCGGGCCCCCCCTCGAGGTCGACC TCCGCTTTCTTCAACCAAGAGGC	*SalI*
chNRBF2_LA_rev	GTCCTGGTGGTTTTCCCTTTTCTTGGGATATCGCC AGATCGTTGATACTCCTGAGC	*SalI*
chNRBF2_RA_for	GCTCAGGAGTATCAACGATCTGGCGATATCCCAA GAAAAGGGAAAACCACCAGGAC	*SpeI*
chNRBF2_RA_rev	GCGGTGGCGGCCGCTCTAGAACTAGTCCGATCCA ATTTAAGGCCCATGGG	*SpeI*
NRBF2_SLIC in pMSCVpuro_for	CTCTAGGCGCCGGAATTAGATCTCTCGAGGCCGC CACCATGGAAGTAATGG	*XhoI*

NRBF2s SLIC in pMSCVpuro_rev	CCTCCCCTACCCGGTAGAATTCGTTAACCTCGAGT TAATTATTCATAAATCCTTTCAGAATATC	*XhoI*
HA-NRBF2_SLIC in pMSCVpuro_for	CTCTAGGCGCCGGAATTAGATCTCTCGAGGCCGC CACCATGTATCCGTATG	*XhoI*
NRBF2_SLIC in pBABEpuro_for	GATCCCAGTGTGGTGGTACGTAGGAATTCGCCGC CACCATGGAAGTAATGGAAGGACCC	*EcoRI*
NRBF2s SLIC in pBABEpuro _rev	CATTCCACAGGGTCGACCACTGTGCTGGCGAATT CTTAATTATTCATAAATCCTTTCAGAATATC	*EcoRI*
HA-NRBF2_SLIC in pBABEpuro _for	GATCCCAGTGTGGTGGTACGTAGGAATTCGCCGC CACCATGTATCCGTATGATGTGCCGGATTATGCG GAAGTAATGGAAGGACCCC	*EcoRI*
NRBF2_SLIC in pET-15b_for	CAGCGGCCTGGTGCCGCGCGGCAGCCATATGGAA GTAATGGAAGGACCCCTC	*NdeI*
NRBF2_SLIC in pET-15b_rev	GTTAGCAGCCGGATCCTCGAGCATATGTTAATTAT TCATAAATCCTTTCAGAATATC	*NdeI*
NRBF2-GFP_SLIC in pMSCVpuro_NRBF2_for	CTTCTCTAGGCGCCGGAATTAGATCTGCCGCCACC ATGGAAGTAATGGAAGGACCCC	*BglII*
NRBF2-GFP_SLIC in pMSCVpuro_NRBF2_rev	GTGAACAGCTCCTCGCCCTTGCTCACACTAGTATT ATTCATAAATCCTTTCAGAATATCCTC	*BglII*
NRBF2-GFP_SLIC in pMSCVpuro_GFP_for	GATATTCTGAAAGGATTTATGAATAATACTAGTGT GAGCAAGGGCGAGGAGC	*BglII*
NRBF2-GFP_SLIC in pMSCVpuro_GFP_rev	GTAGAATTCGTTAACCTCGAGAGATCTTTACTTGT ACAGCTCGTCCATGC	*BglII*
GFP-NRBF2_SLIC in pMSCVpuro_GFP_for	TCCTTCTCTAGGCGCCGGAATTAGATCTGCCGCCA CCATGGTGAGCAAGGGCGAGG	*BglII*
GFP-NRBF2_SLIC in pMSCVpuro_GFP_rev	GGTTGAGGGGTCCTTCCATTACTTCACTAGTCTTG TACAGCTCGTCCATGC	*BglII*
GFP-NRBF2_SLIC in pMSCVpuro_NRBF2_for	CTCGGCATGGACGAGCTGTACAAGACTAGTGAAG TAATGGAAGGACCCCTC	*BglII*
GFP-NRBF2_SLIC in pMSCVpuro_NRBF2_rev	GTAGAATTCGTTAACCTCGAGAGATCTTTAATTAT TCATAAATCCTTTCAGAATATC	*BglII*

Reverse primers for HA-NRBF2_SLIC in pMSCVpuro or HA-NRBF2_SLIC in pBABEpuro was identical to reverse primer for NRBF2_SLIC in pMSCVpuro or NRBF2_SLIC in pBABEpuro, respectively.

Oligonucleotides for site directed mutagenesis

Primer name	5’ - 3’ sequence
chNRBF2_Stop codon_for	CAGGGAAATAAGAAGAAGCCATTTCTTG
chNRBF2_Stop codon_rev	CTGCCAACAAGCGGTCTG
NRBF2_BamHI_for	TTGACAGGGACCCAGACACAC
NRBF2_BamHI_rev	AGATCCCCTGAATCTCAG
NRBF2_S15A_for	TCATCAACAGGCCAGACGAGCAGACCGTTTATTAG
NRBF2_S15A_rev	GCCAGGTTGAGGGGTCCT
NRBF2_S50A_for	GCTGACACAGGCAGAGCAGGC
NRBF2_S50A_rev	TTCATGGCTTCAGAAAGATATGCTGC
NRBF2_S56A_for	GGCTCATCTTGCACTGGAATTG
NRBF2_S56A_rev	TGCTCTGACTGTGTCAGC
NRBF2_S101A_for	TCTTCAGACAGCTCACAAACCCTC
NRBF2_S101A_rev	TGGGCAGCTGCATCCTTG
NRBF2_S277A_for	TATGGAGCTCGCTGAGGATATTC
NRBF2_S277A_rev	AGAGGAAGTTCTGGAGATG
NRBF2_S15D_for	TCATCAACAGGACAGACGAGCAGACCGTTTATTAG
NRBF2_S50D_for	GCTGACACAGGACGAGCAGGCTC
NRBF2_S50D_rev	TTCATGGCTTCAGAAAGATATG
NRBF2_S56D_for	GGCTCATCTTGACCTGGAATTGCAAAGG
NRBF2_S101D_for	TCTTCAGACAGATCACAAACCCTC
NRBF2_S277D_for	TATGGAGCTCGATGAGGATATTC

Reverse primers for NRBF2_S15D, S56D, S101D and S277D were identical to reverse primers for NRBF2_S15A, S56A, S101A and S277A.

Oligonucleotides for qRT-PCR

Primer name	5’ - 3’ sequence
chNrbf2_for	GCTATCACTGGAATTACAAAGG
chNrbf2_rev	GCATTCTGCTGAGCTTTCATC
18SrRNA_for	CGGCTACCACATCCAAGGAA
18SrRNA_rev	GCTGGAATTACCGCGGCT
Hprt1_for	AAGTGTTGGATACAGGCCAGA
Hprt1_rev	GGCTTTGTATTTGGCTTTTCC
Ulk1_for	ACACTAGTTCCTGCCATCCC
Ulk1_rev	CATCAAAGTCCATGCGGTCC
Atg13_for	TTGCCCTCAAGACTGTCCAA
Atg13_rev	GAACCAATCTGAACCCGTCG

Becn1_for	AGCTTTTCTGGACTGTGTGC
Becn1_rev	CTTTCTCCACGTCCATCCTGT
Pik3C3_for	CTACAAGAACTCCCGGCAGA
Pik3c3_rev	GATGAGCCTTGGTGAGCTTG
Atg14_for	ACCAAACAACGGGGACTACT
Atg14_rev	ATGCTCCATGTCAGGTCCTT
Uvrag_for	TGGAAAGACAGAAGAAAGCGC
Uvarg_rev	TGCACTTCCTTTGTCCTGTAGA
Map1lc3b_for	CAAGACCAAGTTCCTGGTGC
Map1lc3b_rev	CAAGCGCCGTCTGATTATCT
Pink1_for	TGAAGAACTACCCCTGTACCC
Pink1_rev	GCAAGGTCATCATGGTAGCC
Bnip3_for	GGGGAATTTTCTCAGCAGACTTT
Bnip3_rev	TCCAATGTAGATCCCCAAGCC
Tsc1_for	CTCAATTCTGAACGTGGGCC
Tsc1_rev	GATGTGCAATACCGGCTGAG
Wdr45_for	CAACCAAGACCAAAGCTGCT
Wdr45_rev	CTGCTCGTGGTCAAGATGC
Ppara_for	CCACGAAGCCTACCTGAAGA
Ppara_rev	CATGTATGACAAAAGGCGGGT
Rxra_for	GCTCCTCAGGCAAACACTATG
Rxra_rev	GCAGGTGTAGGTCAGGTCTT
Rarg_for	GGTCACCAGAAATCGATGCC
Rarg_rev	CGTTCCTTACAGCTTCCTTGG
Stat2_for	CCCCATCAGAGCCAACAGG
Stat2_rev	ATGTCCAGCACCTCCTTTCT
Foxo3_for	CTGCGGGCTGGAAGAACT
Foxo3_rev	GCCCGTGCCTTCATTCTG
Jun_for	GAGAACAGACTGTCAGGGCT
Jun_rev	CTCTGTCGCAACCAGTCAAG
Nfkb1_for	GAGCAACCAAAACAGAGGGG
Nfkb1_rev	CACTAGAGGCTCCCGGAAG
Irf7_for	TGATCCTGGTGAAGCTGGAG
Irf7_rev	GGACACACCCTCACGCTG
Pex7_for	CTGGTCTCCTCACATCCCTG
Pex7_rev	TCTGATCTCCTGAGGCTGAAG
Il6_for	TCTGCAAGAGACTTCCATCCA
Il6_rev	GTTGTCACCAGCATCAGTCC
Acox1_for	TCAAGAGAAGCGAGCCAGAG
Acox1_rev	CCAGGAGCGGGAAGAGTTTA

Sesn2_for	GTCAACAAGTTACTGGCGCA
Sesn2_rev	AGCAAGGCCTGGATATGCTC
Ctsf_for	AGATGAGTCCAGCCAAGTCC
Ctsf_rev	ACACATGCCCTGGTTCTTCA

Oligonucleotides for siRNA knockdown

siRNA	Supplier and reference number (#)
ON-TARGETplus Mouse Nrbf2 siRNA SMARTpool	Dharmacon, #L-161736-00-0010
ON-TARGET plus Non-targeting Pool	Dharmacon, #D-001810-10-05

4.1.3 Bacteria strains

***Escherichia coli* strains used in this thesis**

Strain	Genotype	Application
DH5α	F^- endA1 glnV44 thi-1 recA1 relA1 gyrA96 deoR nupG purB20 Φ80dlacZΔM15 Δ(lacZYA-argF)U169, hsdR17(r_K^- m_K^+), λ^-	Propagation of vector DNA
BL21 (DE3)	E. coli str. B F^- ompT gal dcm lon $hsdS_B(r_B^-m_B^-)$ λ(DE3 [lacI lacUV5-T7p07 ind1 sam7 nin5]) $[malB^+]_{K-12}(\lambda^S)$	Bacterial protein expression

4.1.4 Enzymes for molecular biology

Enzyme	Supplier and reference number (#)
Restriction endonucleases	Thermo Fisher Scientific
Klenow Fragment	Thermo Fisher Scientific, #EP0054
Fast AP (Alkaline Phosphatase)	Thermo Fisher Scientific, #EF0654
T4 DNA Ligase	Thermo Fisher Scientific, #EL0014
Phusion™ High-Fidelity DNA Polymerase	Thermo Fisher Scientific, #F-530S
Proteinase K	Thermo Fisher Scientific, # 17916
Taq DNA Polymerase	Thermo Fisher Scientific, #10342020
Q5® High-Fidelity DNA Polymerase	New England Biolabs, #M0493S
Kinase Ligase *DpnI* (KLD) Enzyme Mix	New England Biolabs, #M0554S
LA-*Taq* DNA polymerase	Takara, #RR002A

4.1.5 Antibodies

Primary antibodies

All antibodies used for immunoblotting in this thesis were supplied by Abcam (Cambridge, UK), Bethyl Laboratories (Montgomery, TX, USA), Cell Signaling Technology (Danvers, MS, USA), MBL International (Woburn, MA, USA), Merck Millipore (Burlington, MA, USA), Santa Cruz Biotechnology (Dallas, TX, USA), Sigma-Aldrich (St. Louis, MO, USA), Thermo Fisher Scientific (Waltham, MA, USA), ChromoTek (Planegg-Martinsried, Germany), Proteintech (Rosemont, IL, USA), GE Healthcare (Chalfont St Giles, UK), Biolegend (San Diego, CA, USA), Progen Biotechnik (Heidelberg, Germany), Bio-Rad (Hercules, CA, USA), LI-COR Biosciences (Lincoln, NE, USA) or Jackson ImmunoResearch (Cambridgeshire, UK).

Antibody	Supplier and reference number (#)	Application
Mouse anti-Vinculin	Sigma Aldrich, #V9131	IB
Mouse anti-ACTB	Sigma Aldrich, #A5316	IB
Mouse anti-GAPDH	Abcam, #ab8245	IB
Rat anti-GFP	ChromoTek, #3H9	IB
Goat anti-GST	GE Healthcare, #27-4577-01	IB
Mouse anti-HA	BioLegend, #901501	IB
Rabbit anti-NRBF2	Cell Signaling Technology, #8633	IB, IP, PLA
Rabbit anti-NRBF2	Bethyl Laboratories, #A301-851A	IF
Rabbit anti-BECN1	Santa Cruz Biotechnology, #11427	IB
Rabbit anti-PIK3C3	Thermo Fischer Scientific, #PA1-46456	IB
Rabbit anti-PIK3R4	Cell Signaling Technology, #14580	IB
Rabbit anti-ATG14	MBL International, #PD026	IB
Goat anti-ATG14	Santa Cruz Biotechnology, #164767	IP
Rabbit anti-UVRAG	Cell Signaling Technology, #13115	IB
Rabbit anti-ULK1	Cell Signaling Technology, #8054	IB
Rabbit anti ULK1 pSer757	Cell Signaling Technology, #6888	IB
Rabbit anti-LC3	Cell Signaling Technology, #2775	IB
Rabbit anti-LC3	MBL International, #PM036	IF
Guinea pig anti-SQSTM1/p62	Progen Biotechnik, #GP62-C	IB
Mouse anti-WIPI2	Bio-Rad, #MCA5780GA	IF
Rabbit anti-PPAR alpha	Thermo Fischer Scientific, #PA1-822A	IB
Rabbit anti-PPAR gamma	Cell Signaling Technology, #2430	IB
Rabbit anti-RXR alpha	Proteintech, #21218-1-AP	IB
Mouse anti-phospho-serine	Merck Millipore, #05-1000	PLA

Secondary antibodies

Antibody	Supplier and reference number (#)	Application
Goat anti-mouse IRDye®680RD	LI-COR Biosciences, #925-68070	IB
Goat anti-rabbit IRDye®680RD	LI-COR Biosciences, #925-68071	IB
Goat anti-mouse IRDye®800CW	LI-COR Biosciences, #926-32210	IB
Goat anti-rabbit IRDye®800CW	LI-COR Biosciences, #926-32211	IB
Donkey anti-guinea pig IRDye®680LT	LI-COR Biosciences, #925-68030	IB
Donkey anti-goat IRDye®680LT	LI-COR Biosciences, #926-68024	IB
Goat anti-rabbit Alexa Fluor ® 647	Jackson ImmunoResearch, #111-605-003	IF
Goat anti-mouse Alexa Fluor ® 647	Jackson ImmunoResearch, #115-605-003	IF

4.1.6 Compounds and recombinant proteins

Compound	Supplier and reference number (#)
Bafilomycin A_1	Alfa Aesar, #J61835
Puromycin	InvivoGen, #ant-pr-1
Histidinol	Sigma-Aldrich, #H6647
Bleocin®	Calbiochem, #203408
Telmisartan	Selleckchem, #S1738
GW501516	Selleckchem, #S5615
GW7647	Cayman Chemical, #10008613
Wy14643	Selleckchem, #S8029
MRT6730	Selleckchem, #S7948
bortezomib	Merck Millipore, #5.043.140.001
MG-132	Merck Millipore, #474790
GST-ULK1 [human]	Sigma-Aldrich, #SRP5096
GST-p40PX	Echelon Biosciences, #G0302

4.1.7 Buffers and solutions

1 x TBS	150 mM NaCl; 50 mM Tris
Tris/HCl	0.5 - 1.5 M Tris; pH adjusted to 6.8 - 8.8 with HCl
4% PFA in PBS	PFA dissolved in PBS using NaOH, pH adjusted to 7.0 with HCl

4.1.8 Media and supplements for cell culturing

DMEM (4.5 g/L D-Glucose)	Thermo Fisher Scientific, #41965-039
RPMI 1640	Thermo Fisher Scientific, #21875-091
DMEM/F-12, GlutaMAX™ supplement	Thermo Fisher Scientific, #10565018
DPBS (1x)	Thermo Fisher Scientific, #14190-094
EBSS	Thermo Fisher Scientific, #24010-043
Penicillin/Streptomycin (10,000 U/mL 10,000 µg/mL)	Thermo Fisher Scientific, #15140-122
Trypsin/EDTA solution (0.05% / 1x)	Thermo Fisher Scientific, #25300-054
Fetal Calf Serum (FCS)	Thermo Fisher Scientific, #10270
Chicken Serum (CS)	Sigma-Aldrich, #C5405
Beta-mercaptoethanol	Sigma-Aldrich, #M3148
GlutaMAX	Thermo Fisher Scientific, #35050-038
Insulin-Transferrin-Selenium (ITS) (100 x)	Thermo Fisher Scientific, #41400045
Dexamethasone	Sigma-Aldrich, #D4902

4.1.9 Additional materials

Autoradiography Hypercasette	Amersham, GE Healthcare
X-ray film BioMax® MR	Kodak
Developing solution	AGFA, #G150
Fixation solution	AGFA, #G150
[^{32}P] ATP	Hartmann Analytic, #SRP-301
ATP (10 mM)	Cell Signaling Technology
dNTP mix (10 mM each)	Promega
NucleoSpin® Plasmid purification kit	Macherey-Nagel
NucleoBond® xtra Maxi EF kit	Macherey-Nagel
NucleoSpin® Extract II Gel extraction kit	Macherey-Nagel
NucleoSpin® RNA II Kit	Macherey-Nagel
TA-Cloning® Kit	Thermo Fisher Scientific, #K202040
Lipofectamine® RNAiMAX transfection reagent	Thermo Fisher Scientific, #13778
DuoLink® In Situ Red Starter Kit Mouse/Rabbit	Sigma-Aldrich, #DUO092101
Protein Assay Kit	Bio-Rad
GFP-Trap®	ChromoTek, #gta-200
PtdIns	Avanti Polar Lipids, #840042
Nitrocellulose membrane	GE Healthcare
PVDF membrane (Immobilon-FL)	Merck Millipore, #IPFL00010
High-Capacity cDNA Reverse Transcription Kit	Thermo Fisher Scientific, #4368814
RNAse inhibitor	Thermo Fisher Scientific, #10777-019

GoTaq® qPCR Master Mix	Promega, #A6002
FuGENE® 6	Promega, #E2691
GeneRuler 1 kb DNA ladder	Thermo Fisher Scientific, #SM0314
GeneRuler 100 bp Plus DNA ladder	Thermo Fisher Scientific, #SM0321
DNA Gel loading dye (6x)	Thermo Fisher Scientific, #R0611
PAGERuler TM Prestained Protein Ladder	Thermo Fisher Scientific, #26616
Digitonin	Wako, 043-21376
Mowiol®4-88	Carl Roth, #0713
DAPI	Carl Roth, #6335
Glass cover slips, 10 mm	Paul Marienfeld, #0111500
Freezing Container, Mr. Frosty™	Thermo Fisher Scientific
Gel filtration Calibration Kit LMW/HMW	GE Healthcare
Lysozyme	Carl Roth
0.45 µm PVDF filter unit	Carl Roth
Nunc™ Lab-Tek™ Chambered Coverglasses	Thermo Fisher Scientific
Neubauer counting chamber	Paul Marienfeld
Polybrene	Sigma-Aldrich
Protease Inhibitor Cocktail	Sigma-Aldrich
Protein G sepharose	GE Healthcare, #17061801
Glutathione sepharose	GE Healthcare, 17075601
Superdex 200 Increase 10/300 GL column	GE Healthcare
Tissue culture equipment (dishes, pipettes etc.	Greiner, Sarstedt, Nunc
Dounce homogenizer	Wheaton
HD Green Plus DNA stain	Intas Science Imaging, #ISII-HDGreen Plus
Agarose	Bio-Budget, # 10-35-1020
Dimethyl pimelimidate (DMP)	Sigma-Aldrich, #80490-5G

4.1.10 Technical equipment

Bacteria incubator, Certomat BS-1	Sartorius
Cell culture bench, HERAsafe®	Thermo Fisher Scientific
Cell culture incubator, HERAcell® 240 CO_2	Thermo Fisher Scientific
Centrifuge, Heraeus™ fresco™ 17	Thermo Fisher Scientific
Centrifuge, Heraeus™ pico™ 17	Thermo Fisher Scientific
Centrifuge, Megafuge 40R	Thermo Fisher Scientific
Milligram balance, MSE1203S-100-DE	Sartorius
FPLC ÄKTApurifier	GE Healthcare
PCR cycler, GeneAmp® PCR System 9700	Applied Biosystems
pH Meter, Five Easy	Mettler Toledo

Thermomix comfort	Eppendorf
Spectrophotometer, nanodrop1000	PeqLab
TSP SP2 inverse confocal laser scanning microscope with a Plan APO 63x water objective	Leica
LSM 710 inverse confocal laser scanning microscope with a Plan Apochromat 63x/1.4 oil objective	Zeiss
Microplate reader Synergy MX	BioTek
Nucleofector I	Amaxa Biosystems
Amaxa™ Cell Line Nucleofector™ Kit T	Lonza
Odyssey® Infrared Imaging System I	LI-COR Biosciences
Applied Biosystems 7300 Real Time PCR System	Thermo Fisher Scientific
Ultrasonic homogenizers, Sonoplus HD 2070	Bandelin
Agarose gel electrophoresis chambers	PeqLab
Mini Electrophoresis system, Mini-PROTEAN Tetra	Bio-Rad
Wide-mini Electrophoresis system, SE640	Hoefer
Rotaiting Wheel	Neolab
Skaking unit, Duomax 1030	Heidolph
Wet transfer unit	Bio-Rad
Gel-drying apparatus, model 583	Bio-Rad
Heating block (MBT 250)	Kleinfeld Labortechnik

4.1.11 Software

CorelDraw® X7

ImageJ

Microsoft® Office 2016

Image Studio Light v. 4

SnapGene v. 1.1.3

The PyMOL Molecular Graphics System, Version 2.0.7 Schrödinger, LLC.

SDS (Real-Time PCR) Software v. 1.4

Cytoscape v. 3.2.1 with ClueGO Plugin

Mendeley v. 1.19.1

4.1.12 Websites and databases

http://multalin.toulouse.inra.fr/multalin/

https://blast.ncbi.nlm.nih.gov/Blast.cgi

http://www.expasy.org

http://www.ncbi.nlm.nih.gov

http://www.rcsb.org/pdb/home/home.do

http://www.uniprot.org

http://www.ensembl.org

http://primer3.ut.ee/

4.2 Methods

4.2.1 Methods in molecular biology

4.2.1.1 Generation of chemically competent *E. coli* bacteria

5 mL LB medium were inoculated with the *E. coli* strain and incubated at 37 °C under constant shaking (180 rpm) overnight. The next day, 150 mL LB medium were inoculated with 900 µL of the overnight culture. The culture was grown until an OD_{600} of 0.45 - 0.55. The bacteria suspension was kept on ice for 10 min and then harvested at 2,000 rpm at 4 °C for 10 min. The supernatant was removed and the bacteria were resuspended in 30 mL of TFB I-solution and incubated for 10 min on ice. The bacteria were centrifuged and resuspended in 6 mL ice-cold TFB II-solution. 50 µL portions of this cell suspension were transferred into 1.5 mL reaction tubes and flash frozen with liquid nitrogen. The competent bacteria were stored at -80 °C.

LB medium	20 g LB-medium; ad 1000 mL dH_2O; autoclaved and stored at 4 °C
TFB I	100 mM KCl; 10 mM $CaCl_2 \cdot 2\ H_2O$; 30 mM KOAc, pH 6.0; 15% (v/v) glycerol; adjusted to pH 6.1 with HOAc; autoclaved; addition of 50 mM $MnCl_2 \cdot 4\ H_2O$ (sterile filtered); stored at 4 °C

TFB II	75 mM $CaCl_2 \cdot 2\ H_2O$; 10 mM KCl; 10 mM MOPS; 15% (v/v) glycerol; adjusted to pH 7.0 with KOH; autoclaved; stored at 4 °C

4.2.1.2 Transformation of chemically competent *E. coli* bacteria

An aliquot of the chemically competent bacteria was thawed on ice. An appropriate amount of plasmid DNA or 5 µL of a ligation, site directed mutagenesis or SLIC reaction were added to the bacteria. The mixture was incubated on ice for 15 min, heat-shocked at 42 °C for 45 s and returned to ice for 2 min. Then, 300 µL LB medium were added and the mixture was incubated at 37 °C for 30 min under constant agitation (300 rpm). Subsequently, the bacteria were spread onto LB plates containing an appropriate antibiotic and incubated at 37 °C overnight. Bacteria transformed with the pCR2.1®-TOPO vector were spread on LB/ampicillin/IPTG/X-Gal containing plates for blue/white selection. Single bacteria colonies were used for isolation of plasmid DNA (see 4.2.1.3).

LB agar	20 g agar per 100 mL LB medium; autoclaved and cooled to 60 °C; addition of antibiotic (ampicillin to a final concentration of 100 µg/mL, kanamycin to a final concentration of 50 µg/mL); stored at 4 °C
X-Gal/IPTG plates	LB agar containing ampicillin, supplemented with 10 µg/mL X-Gal and 25 mM IPTG; stored at 4 °C

4.2.1.3 Isolation of Plasmid DNA

5 mL LB medium supplemented with appropriate antibiotics were inoculated with a single bacterial colony at 37 °C under constant shaking (180 rpm) overnight. Cells were centrifuged and the plasmid DNA isolation was performed using the NucleoSpin® Plasmid kit (Macherey-Nagel) according to the manufacturer's instructions. For the production of larger amounts of plasmid DNA, up to 300 mL bacterial culture were used. The plasmid DNA isolation was performed using the NucleoBond® xtra Maxi EF kit (Macherey-Nagel) according to the manufacturer's instructions.

4.2.1.4 Digestion of DNA with restriction endonucleases

Sequence specific cleavage of DNA molecules was performed by incubation with restriction endonucleases (Thermo Fischer Scientific) according to the manufacturer's instructions.

4.2.1.5 Fill-in of 5'-overhangs of dsDNA

Fill-in of 5'-overhangs of dsDNA resulting from restriction endonuclease digestion was performed by Klenow fragment (Thermo Fisher Scientific). Digested dsDNA was incubated with 2 U Klenow fragment and dNTPs at 37 °C for 15 min. DNA molecules were separated by agarose gel electrophoresis (see 4.2.1.7) and isolated by gel extraction (see 4.2.1.8).

4.2.1.6 Dephosphorylation of vector DNA

To prevent re-ligation, linearized vector DNA harboring blunt ends generated by digestion with restriction nucleases was dephosphorylated prior to ligation at the 5`- and 3'-positions using alkaline phosphatase (FastAP, Thermo Fisher Scientific). Therefore, FastAP was directly added to linearized vector DNA after digestion with restriction endonucleases and incubated according to the manufacturer's instructions. DNA molecules were separated by agarose gel electrophoresis (see 4.2.1.7) and isolated by gel extraction (see 4.2.1.8).

4.2.1.7 Agarose gel electrophoresis of nucleic acids

After digestion of DNA molecules by restriction endonucleases or after polymerase chain reactions (see 4.2.1.16) the produced DNA fragments were separated by agarose gel electrophoresis. Gels were prepared by dissolving 0.8 - 2% agarose (w/v) in TAE buffer by heating in a microwave. HD Green DNA stain was added and the solution was filled into a gel casting platform. The DNA samples were mixed with 6 x DNA loading buffer and loaded onto the gel. As reference, a DNA molecular weight standard was used (Thermo Fisher Scientific). The electrophoresis was performed in electrophoresis chambers (PeqLab) containing TAE buffer at 120 - 240 V.

TAE buffer (50x)	2 M Tris; 1 M HOAc; 50 mM EDTA; adjusted to pH of 8.5 with NaOH

4.2.1.8 Extraction of DNA fragments from agarose gels

Extraction of DNA fragments from agarose gels was performed using the NucleoSpin® Extract II Gel extraction kit (Macherey-Nagel) according to the manufacturer's instructions. DNA was eluted with dH_2O.

4.2.1.9 Photometric determination of DNA and RNA concentrations

DNA and RNA concentrations were determined using the Nanodrop1000 (PeqLab) according to the manufacturer's instructions. The concentration and purity of DNA and RNA were estimated by the following formulas:

1 A_{260} unit ≈ 50 µg/mL for dsDNA	pure DNA: $A_{260}/A_{280} \geq 1.8$
1 A_{260} unit ≈ 40 µg/mL for ssRNA	pure RNA: $A_{260}/A_{280} \geq 2.0$

4.2.1.10 Ligation of DNA fragments

For the ligation of linearized vectors and DNA fragments (inserts) the T4 DNA ligase was used (Thermo Fisher Scientific), which catalyzes the formation of phosphodiester bonds between 5'-phosphate and 3'-hydroxyl termini in dsDNA. Ligation reactions were performed with a molar ratio of 1:3 (vector : insert DNA). Used DNA amounts were calculated by the following formula:

$$f = \frac{vector\ length\ (bp)}{insert\ length\ (bp)} \times \frac{concentration\ of\ insert}{concentration\ of\ vector} \times \frac{1}{3}$$

The ligation reactions were incubated at RT for 1 h or at 16 °C overnight and directly used for transformation of chemically competent bacteria (see 4.2.1.2).

4.2.1.11 DNA sequence analysis

Sequencing of DNA molecules was performed by Microsynth Seqlab (Göttingen, Germany) using the Sanger sequencing technique [149].

4.2.1.12 Isolation of genomic DNA from eukaryotic cells

Genomic DNA as template for genomic screening PCR was isolated from approximately 5 x 10^6 DT40 cells. Therefore, cells were centrifuged, the pellet was resuspended in 50 µL buffer K and incubated for 1 h at 56 °C. After inactivation of proteinase K for 15 min at 95 °C the prepared genomic DNA solution was directly used as PCR template using LA-*Taq* (see 4.2.1.16.1) or stored at -20 °C.

Buffer K 10 mM Tris/HCl, pH 8.0; 50 mM KCl; 0.45% NP-40; 0.45% Tween® 20; 100 µg/mL proteinase K

4.2.1.13 Isolation of total RNA from eukaryotic cells

Total RNA was isolated from approximately 1 x 10^6 cells using the NucleoSpin® RNA II Kit (Macherey-Nagel) according to the manufacturer's instructions. Isolated RNA was either directly used for reverse transcription reaction (see 4.2.1.14) or stored at -80 °C.

4.2.1.14 Reverse transcription (RT) reaction

First strand cDNA was generated using the High-Capacity cDNA Reverse Transcription Kit (Thermo Fisher Scientific) according to the manufacturer's instructions. 1 µg of isolated total RNA and Random Hexamer Primers, additional RNAse inhibitor (Thermo Fisher Scientific) and standard cycling conditions (10 min at 25 °C, 120 min at 37 °C, 5 min at 85 °C) were used for amplification. Generated cDNAs were directly used for qRT-PCR or stored at -20 °C.

4.2.1.15 Real-time quantitative reverse transcription PCR (qRT-PCR)

Quantitative real-time PCR analysis was performed using the Applied Biosystems 7300 Real Time PCR System (Thermo Fisher Scientific) and GoTaq® qPCR Master Mix (Promega). 25 ng of total cDNA (see 4.2.1.14) were amplified in triplicates in the presence of 500 nM primers with a standard temperature profile (2 min at 50 °C, 10 min at 95 °C, 40 cycles of 15 s at

95 °C and 1 min 60 °C) followed by a dissociation run (15 s at 95 °C, 1 min at 60 °C, gradual increase of 1 °C/min up to 95 °C).

Threshold (C_T) values were computed automatically. Amplification efficiencies (E) of designed primer pairs were obtained by measurement of template cDNA serial diluted by factor 10. C_T values for each dilution step were plotted against the dilution factor, linear regression was computed and amplification efficiencies were calculated from the ascent of compensation lines by the following formula:

$$E = 10^{\frac{1}{\text{slope}}}$$

Absolute copy numbers of respective genes were normalized to absolute copy numbers of *Hprt1* as reference gene and relative gene expression was calculated by the following formula:

$$ratio = \frac{(E_{target\ gene})^{\Delta C_T\ target\ gene\ (control-sample)}}{(E_{reference\ gene})^{\Delta C_T\ reference\ gene\ (control-sample)}}$$

4.2.1.16 Polymerase chain reaction (PCR)

The polymerase chain reaction enables the exponential amplification of DNA fragments *in vitro*. Short synthetic oligonucleotides (primers), which are complementary to the 5'- (forward primer) and the 3'- regions (reverse primer) of the donor DNA (template) serve as starting points for the DNA polymerase [150,151]. A PCR consist of three distinct steps (denaturation, annealing, elongation), which are performed at different temperatures and are repeated for several cycles. Generally, both primers (forward and reverse) were set up in a 10 µM master mix, which was used for PCR. To avoid non-specific DNA amplification, all PCRs were performed as hot start PCR by keeping the reactions on ice and subsequently transferring them to a preheated PCR cycler at 95 °C.

4.2.1.16.1 Amplification of genomic DNA

Amplification of genomic DNA fragments larger than 1 kb for the generation of knockout targeting vectors or for subsequent screening PCR was performed by long range PCR using the LA-*Taq* DNA polymerase (Takara).

PCR reaction for amplification of genomic DNA

2.0 µL	genomic DNA
2.5 µL	10 x LA-*Taq* buffer
0.5 µL	dNTP mix (10 mM each)
2.0 µL	$MgCl_2$ (25 mM)
0.5 µL	primer mix (10 µM each)
0.08 µL	LA-*Taq*
ad 25 µL	dH_2O

PCR program for genomic (screening) PCR

step	**description**	**T [°C]**	**time**	
1	initial denaturation	98	2 min	
2	denaturation	98	30 s	35 x
3	annealing	T_m - 5 °C	30 s	
4	elongation	72	30 s / kb	
5	final elongation	72	10 min	
6	cooling	12	∞	

4.2.1.16.2 Amplification of cDNA

Amplification of protein coding cDNA from eukaryotic cells was done by Phusion™ DNA polymerase (Thermo Fisher Scientific). This enzyme displays a 3' → 5' exonuclease activity and thereby enables accurate DNA amplification. The used cDNA templates were generated by reverse transcription (see 4.2.1.14) of isolated total RNA (see 4.2.1.13).

PCR reaction for amplification of cDNA

5-50 ng	cDNA template
10 µL	5 x Phusion reaction buffer
1.0 µL	dNTP mix (10 mM each)
1.0 µL	primer mix (10 µM each)
0.5 µL	Phusion™ High-Fidelity DNA polymerase (2 U/µL)
ad 50 µL	dH_2O

PCR program for amplification of cDNA

step	description	T [°C]	time	
1	initial denaturation	98	30 s	
2	denaturation	98	30 s	30 x
3	annealing	T_m - 5 °C	30 s	
4	elongation	72	30 s / kb	
5	final elongation	72	10 min	
6	cooling	12	∞	

4.2.1.16.3 Site-directed mutagenesis PCR

For site-directed mutagenesis of DNA sequences was performed by *in vitro* amplification of the complete cDNA-containing vector using synthetic oligonucleotides containing the desired mutations in combination with the Q5® site-directed mutagenesis kit (New England Biolabs) according to the manufacturer's instructions. Generally, mutagenesis primers were designed adjoining and non-overlapping and the forward primer contained the desired mutations. After completed PCR amplification template DNA isolated from dam positive *E. coli* cells was digested for 1 h at 37 °C by *DpnI* restriction endonuclease, which specifically cleaves non-mutated, dam methylated DNA. 1 µL of the PCR reaction was incubated with kinase-ligase-*DpnI* (KLD) reaction mix for 5 min at room temperature (RT). Subsequently, chemically competent bacteria were transformed with 5 µL of the reaction mix. For verification of accurate DNA modification, plasmid DNA was isolated (see 4.2.1.3) and analyzed by DNA sequencing (see 4.2.1.11).

PCR reaction for Site-directed mutagenesis PCR

1 - 25 ng	template DNA
12.5 µL	Q5® Hot Start High-Fidelity 2 x Master Mix
1.25 µL	primer mix (10 µM each)
ad 25 µL	dH_2O

step	description	T [°C]	time	
1	initial denaturation	98	30 s	
2	denaturation	98	10 s	25 x
3	annealing	T_m - 5 °C	30 s	
4	elongation	72	30 s / kb	
5	final elongation	72	10 min	
6	cooling	12	∞	

4.2.1.17 Cloning of PCR products

PCR products harboring 3'-adenine overhangs produced by *Taq* DNA polymerases, were directly cloned into pCR2.1®-TOPO vector by TA-Cloning® Kit (Thermo Fisher Scientific) following the manufacturer's instructions. The multiple cloning site is located within the coding region of the α-peptide of β-galactosidase, which is interrupted by successful integration of PCR products, thus allowing for blue/white screening of positive transformants (see 4.2.1.2). For cloning of PCR products without 3'-adenine overhangs produced by polymerase displaying exonuclease activity like Phusion™ DNA polymerase, the PCR reactions were inactivated by -80 °C for 20 min, 0.2 µL *Taq* DNA polymerase (Thermo Fisher Scientific) and fresh dNTPs were added and additionally incubated at 72 °C for 10 min, prior to TA-cloning®.

4.2.1.18 Sequence and ligation-independent cloning (SLIC)

The sequence and ligation-independent cloning technique was used to replace traditional cloning by restriction endonucleases and ligation of DNA fragments [152]. The original SLIC protocol was performed with minor modifications. Inserts containing approximately 30 bp overlap to adjoining sequences were generated by PCR (see 4.2.1.16) using the proof-reading Phusion™ DNA polymerase and vector backbones were digested by restriction endonucleases (see 4.2.1.4). After clean-up of DNA fragments by agarose gel electrophoresis (see 4.2.1.7) and gel extraction (see 4.2.1.8), single strand synthesis was performed by incubation with Klenow Fragment (Thermo Fisher Scientific) for 30 min at 37 °C, followed by heat inactivation for 15 min at 75 °C. Annealing reactions were

performed at 1:1 molar ratios of insert and vector DNA. 5 µL of the reaction mixture were directly used for transformation of chemically competent bacteria (see 4.2.1.2).

4.2.2 Methods in cell biology

4.2.2.1 Cell culturing

All cell lines used in this thesis were cultivated in a cell incubator at 37 °C, 5% CO_2 and a humidified atmosphere. Handling was performed under a laminar flow cell culture bench. Fetal calf serum (FCS) and chicken serum (CS) were heated to 56 °C for 30 min prior to use for inactivation of complement factors. Cell number was determined using a Neubauer counting chamber. Cells were pelleted using a refrigerated centrifuge for 3 min at 1200 rpm and 4 °C unless otherwise indicated.

4.2.2.1.1 Cell lines

HEK293 (ATCC Number: CRL-1573)

The HEK293 cell line was established by transformation of human embryonic kidney (HEK) cells with adenovirus type 5 DNA [153]. During this thesis, cells expressing BECN1-GFP, GFP, NRBF2-GFP or GFP-NRBF2 were generated by retroviral transduction (see 4.2.2.6) with cDNA encoding for the corresponding genes.

DG75 (ATCC Number: CRL-2625)

DG75 cells are human B lymphocytes, originally derived from the pleural effusion of a child with a primary abdominal lymphoma. This cell line differs from lymphoblastoid cell lines in its growth characteristics and morphology and displays IgM-kappa immunoglobulins on the cell surface [154]. During this thesis, cells expressing BECN1-GFP or GFP were generated by retroviral transduction with cDNA encoding for the corresponding genes.

DT40 (ATCC Number: CRL-2111)

The chicken DT40 B cell line is derived from a bursal lymphoma induced by avian leucosis virus (ALV), originally induced by a viral infection of a 1 day old chicken with Rous associated virus 1 (RAV-1) [155]. DT40 cells express surface IgM and undergo continued IgL gene conversion during culturing [156]. DT40 cells display several unique features like a high ratio of targeted to random integration of foreign DNA [157]. During this thesis *NRBF2*+/- and *NRBF2*-/- cells were generated. Additionally, the NRBF2 knockout cell lines were retrovirally transduced with empty pMSCVpuro vector (DT40 *NRBF2*-/- vector) or cDNA encoding for human NRBF2 (DT40 *NRBF2*-/- hNRBF2). Cells were obtained from the Leibniz Institute German Collection of Microorganisms and Cell Cultures (DSMZ, #ACC 636).

Alpha mouse liver 12 (AML12) cells (ATCC Number: CRL-2254)

The AML12 (alpha mouse liver 12) cell line was established from hepatic cells from transgenic mice overexpressing human transforming growth factor (TGF) alpha [158]. The cells were kindly provided by Prof. Beller (Institute for Mathematical Modeling of Biological Systems, Heinrich Heine University Düsseldorf, Germany).

Mouse embryonic fibroblasts (MEFs)

Wild-type and *nrbf2* KO MEFs containing an insertion of a gene-trap vector in the *Nrbf2* gene were kindly provided by Prof. Zhenyu Yue (Icahn School of Medicine at Mount Sinai, New York, USA) and have been described previously [54].

During this thesis, *nrbf2* KO cells were retrovirally transduced with empty pMSCVpuro vector (MEF *nrbf2* KO vector) or cDNA encoding for N-terminally HA-tagged human wild-type NRBF2 (MEF *nrbf2* KO HA-NRBF2 WT) or mutated versions were all five identified phospho-acceptor sites have been exchanged for alanine (MEF *nrbf2* KO HA-NRBF2 5S-A) or aspartate (MEF *nrbf2* KO HA-NRBF2 5S-D). These cells were used for size exclusion chromatography experiments. Additionally, *nrbf2* KO cells were retrovirally transduced with empty pBABEpuro vector (MEF *nrbf2* KO vector) or cDNA encoding for untagged

human wild-type NRBF2 (MEF *nrbf2* KO NRBF2 WT) or mutated versions were all five identified phospho-acceptor sites have been exchanged for alanine (MEF *nrbf2* KO NRBF2 5S-A) or aspartate (MEF *nrbf2* KO NRBF2 5S-D). These cells were used for determination of the autophagic flux per immunoblot or immunofluorescence or for measurement of *in vitro* or *in vivo* PIK3C3 activity.

Wild-type and *ulk1/2* KO MEFs were prepared from 13.5 days old post coitus embryos and immortalized by transfection with a plasmid containing SV40 genomic DNA [159].

Platinum-E (Plat-E)

Plat-E cells is a potent retrovirus packaging cell line based on the highly transfectable HEK293T cell line. These cells express the viral structural genes *gag*, *pol* and *env* which are under the control of an EF1α promotor and can be used for the high-titer production of replication-incompetent retroviruses [160]. Plat-E cells represent the third generation of packaging cell lines and allow the generation of Moloney murine leukemia virus (MMLV)-derived retroviral particles. Plat-E cells were kindly provided by Toshio Kitamura (Institute of Medical Science, University of Tokyo, Japan).

4.2.2.1.2 Cell line specific culturing conditions

DT40 B lymphocytes and derivatives were cultured in RPMI 1640 containing 10% FCS, 1% CS, 3 mM L-glutamine, 50 µM β-ME, 50 U/mL penicillin, and 50 µg/mL streptomycin. DG75 B lymphocytes and derivatives were cultured in RPMI 1640 containing 10% FCS, 50 U/mL penicillin and 50 µg/mL streptomycin. HEK293 cells and derivatives, MEF cells and derivatives and Plat-E cells were cultured in DMEM containing 10% FCS, 50 U/mL penicillin and 50 µg/mL streptomycin. AML12 cells were cultured in DMEM/F-12 containing 10% FCS, 40 ng/mL dexamethasone, 1 x Insulin-Transferrin-Selenium (ITS), 50 U/mL penicillin, and 50 µg/mL streptomycin. The adherent HEK293, MEF, AML12 and Plat-E cell lines were kept at densities up to 90%. Splitting was performed every 2-3 days by DPBS and trypsin/EDTA solution. The suspension was diluted 1:4 to 1:15. The suspension cell lines DT40 and DG75

were kept at densities below 1 x 10^6 cells/mL and were spitted 1:5 to 1:50 every 2-3 days. For amino acid starvation, cells were washed once with DPBS and incubated in EBSS for the indicated times. For stimulation of PPARs, medium was supplemented with pharmacological PPAR activators at the indicated concentrations and cells were incubated for 24 h.

4.2.2.2 Freezing and thawing of eukaryotic cells

Cells were pelleted and resuspended in freezing medium (90% (v/v) FCS; 10% (v/v) DMSO). 1 mL cell suspension was transferred into a cryo-tube and immediately cooled down to -80 °C with a freezing rate of approximately 1 °C/min. For long time storage, the cells were transferred into liquid nitrogen. For thawing, the cells were warmed to 37 °C, transferred to 10 mL culture medium, centrifuged and resuspended in fresh medium.

4.2.2.3 Transfection of DT40 lymphocytes by electroporation

Transfection of DT40 cells with knockout targeting vectors was performed by electroporation. Therefore, approximately 1 x 10^7 cells were centrifuged, washed once with DPBS and resuspended in 90 µL nucleofector solution T. After addition of 10 µL linearized plasmid (1 µg/µL) the suspension was transferred to an electroporation cuvette, incubated for 10 min on ice and electroporation was done using program B-23 of an Nucleofector I (Amaxa Biosystems). Subsequently, cells were transferred to 20 mL rewarmed medium. After additional 24 h, cells were centrifuged, resuspended in 80 mL of medium supplemented with either 80 µg/mL Bleocin® alone or with Bleocin® in combination with 1 mg/mL Histidinol and transferred to four 96-well dishes (200 µL/well). After 5 - 10 days, visible colonies of stably transfected cells were transferred to 24-well dishes and analyzed by genomic screening PCR (see 4.2.1.16.1).

4.2.2.4 siRNA-mediated knockdown in MEF cells

RNA interference experiments were performed using Lipofectamine® RNAiMAX transfection reagent (Thermo Fisher Scientific) according to the manufacturer's instructions. MEF wild-type cells were seeded one day prior to transfection. On day of transfection, cells were treated with 50 nM *Nrbf2* (Dharmacon) or control siRNA (Dharmacon), respectively. After 24 h, cells were seeded for proximity-ligation assay (see 4.2.2.7) and analyzed after additional 48 h.

4.2.2.5 Transfection of Plat-E cells for the production of recombinant viruses

Plat-E cells were used as packaging cell line for the production of recombinant, replication-incompetent retroviruses for subsequent transduction of target cell lines (see 4.2.2.6). Plat-E cells were grown on 6 cm dishes and adjusted to about 60% confluency at the day of transfection. The transfection mixture of 200 µL serum-free target cell medium, 15 µL FuGENE6® (Promega), 1.9 µg pMSCV based retroviral expression vector was prepared in separate reaction tube and incubated for 15 min at RT. For transduction of HEK293, DG75 or DT40 cells, virus particles had to be pseudotyped by addition of 1.0 µg pVSV-G vector to the transfection mixture. The Plat-E medium was replaced with 3.5 mL of full target cell medium and the transfection mixture was added dropwise. Cells were incubated 48 h for the production of recombinant (VSV-G pseudotyped) retroviral particles.

4.2.2.6 Retroviral transduction of target cells

Retroviral supernatant was centrifuged for 4 min at 300 x g. For suspension cells, 1 x 10^6 cells were resuspended in 3 mL of retroviral supernatant and transferred to 6 cm dishes containing 1.5 mL full target cell medium supplemented with 4.5 µL of freshly prepared polybrene solution (3 mg/mL polybrene in DPBS; sterile filtered). For adherent cells, 5 x 10^4 cells were seeded in a 6 cm dish the day before transduction. Medium was changed to 1.5 mL polybrene-supplemented full target cell medium and 3 mL of retroviral supernatant were added. After 24 h medium was exchanged for full target cell medium and additional 24 h later, medium was exchanged for selection medium containing puromycin (0.5 µg/mL

for DT40 cells and 2.5 µg/mL for DG75, HEK293 and MEF cells). All retroviral infections were performed according to S2 standards and safety instructions.

4.2.2.7 Confocal laser scanning microscopy, immunofluorescence and proximity ligation assay (PLA)

DG75 cells stably expressing BECN1-GFP or GFP were centrifuged, resuspended in RPMI at a density of 2.5 - 4 x 10^6 cells/mL and transferred to chambered cover glasses (Thermo Fischer Scientific). After sedimentation, cells were immediately analyzed by confocal laser scanning microscopy using a Leica TSP SP2 inverse confocal laser scanning microscope with a Plan APO 63x water objective. GFP fluorescence was excited using a 488 nm laser line of an argon laser and emission was detected at 495 - 630 nm.

For immunofluorescence, MEF cells were grown on glass cover slips one day prior to stimulation. Fixation was done with 4% formaldehyde in DPBS for 15 min on ice, followed by quenching with 50 mM NH_4Cl for 15 min at RT and permeabilization with 50 µg/ml digitonin for 5 min. Samples were blocked with 3% BSA in DPBS and incubated with primary antibodies diluted 1:100 for 1 h. After incubation with secondary antibody (diluted 1:500) in the dark, samples were washed two times with 0.2% Tween® 20 in DPBS. Cells were embedded in Mowiol® 4-88 containing 1 µg/ml DAPI. Imaging was performed with a Zeiss LSM 710 inverse confocal laser scanning microscope with a Plan Apochromat 63x/1.4 oil objective. Quantification of images was done with Fiji [161]. Signals and nuclei were counted for single images and the ratio signal to nuclei was calculated.

The proximity ligation assay (PLA) was performed as previously described [18] using the DuoLink® system (Sigma-Aldrich). Sample preparation was performed analogously to immunofluorescence. Primary antibodies were diluted 1:200 and incubated for 1 h at RT. Secondary antibody probing, ligation and amplification were performed according to the manufacturer's instructions. Z stack imaging was performed using a Leica TSP SP2 inverse confocal laser scanning microscope with a Plan APO 63x water objective. Stacks were merged with maximum intensities and signals were quantified using Fiji [161].

4.2.3 Methods in biochemistry

4.2.3.1 Preparation of cleared cellular lysates (CCLs)

For preparation of cleared cellular lysates (CCLs) for immunoblot analyses, adherent cells were harvested by scraping and centrifugation and suspension cells by centrifugation. Cell pellets were washed once with DPBS and resuspended in an appropriate volume of ice-cold lysis buffer (LB). Cells were incubated for 30 min on ice and vortexed every 5 min. Insoluble fragments and nuclei were removed by centrifugation for 10 min at 18,000 x g and 4 °C. The supernatant was transferred to a new reaction tube and total protein concentration was determined (see 4.2.2.3). For preparation of CCLs for immunopurifications, CHAPS was used instead of Triton™ X-100 as detergent in the lysis buffer.

Immunoblot LB	20 mM Tris/HCl, pH 7.5; 150 mM NaCl; 0.5 mM EDTA; 1% (v/v) Triton™ X-100; 1 mM Na_3VO_4; 10 µM Na_2MoO_4; 2.5 mM NaPP; 10 mM NaF and protease inhibitor cocktail
Immunopurification LB	20 mM Tris/HCl, pH 7.5; 150 mM NaCl; 0.5 mM EDTA; 0,3% (w/v) CHAPS; 1 mM Na_3VO_4; 10 µM Na_2MoO_4; 2.5 mM NaPP; 10 mM NaF and protease inhibitor cocktail

4.2.3.2 Preparation of S100 cytoplasmic extracts

S100 cytoplasmic extracts were prepared for size exclusion chromatography (see 4.2.3.7). Therefore, cells were harvested, centrifuged and the cell pellets were resuspended in Roeder A buffer. After 10 min incubation at RT, cells were disrupted with 10 strokes in a 1 ml tight Wheaton douncer. NaCl concentration was adjusted to 150 mM and lysates were centrifuged at 18,000 x g for 15 min at 4 °C. Supernatants were filtered through a 0.45 µm PVDF filter unit and total protein concentration was determined (see 4.2.3.3). S100 cytoplasmic extracts were directly used for size exclusion chromatography or stored at -80 °C.

Roeder A buffer	10 mM HEPES, pH 7; 10 mM KCl; 1.5 mM $MgCl_2$; 0.5 mM DTT and protease inhibitor cocktail

4.2.3.3 Determination of total protein concentrations

Determination of total protein concentration was performed according to the method of Bradford, which is a spectroscopic assay for aqueous protein solutions. Upon protein binding the absorbance maximum of the dye Coomassie® Brilliant Blue G-250 shifts from 465 nm to 595 nm [162]. This assay was performed in 96-well format. Samples were set up in duplicates by mixing 10 µL of CCLs (dilution range 1:10 to 1:100) with 200 µL Bradford reagent (Protein Assay Kit; Bio-Rad; diluted 1:5). After 5 min incubation at RT the absorbance of each sample was detected at 595 nm (Biotek, Synergy MX) and protein concentration was calculated by comparison to a BSA standard curve from 0 to 400 µg/mL BSA in DPBS.

4.2.3.4 Immunopurification (IP), chemical antibody-crosslinking and co-affinity purification (co-AP)

For immunopurification of GFP- or HA-tagged proteins, CCLs were incubated with either GFP-Trap® or anti-HA agarose at 4 °C overnight with rotation. For immunopurification of untagged proteins, CCLs were incubated with corresponding antibodies at 4 °C overnight with rotation. The next day, protein G sepharose was added and samples were additionally incubated for 2 h at 4 °C with rotation. Immunopurified proteins were washed 3 times with lysis buffer and analyzed by immunoblotting (see 4.2.3.6). Chemical crosslinking of antibodies to protein G sepharose was done by incubation with 0.2 M triethanolamine, pH 8.2, containing 3 mg/mL dimethyl pimelimidate (DMP) at 4 °C overnight with rotation. The next day, unreacted DMP was quenched by incubation with 10 mM ethanolamine, pH 8.2, for 1 h at 4 °C overnight with rotation. After washing three times with DPBS, antibodies chemically crosslinked to protein G sepharose were used directly for immunopurification or stored a 4 °C. For co-affinity purification experiments, recombinant GST-fusion proteins bound to glutathione sepharose (see 4.2.3.8) were incubated with CCLs at 4 °C overnight with rotation. The next day, samples were washed 3 times with lysis buffer and analyzed by immunoblotting. Unless otherwise indicated, 2 mg total protein were used for immune- or co-affinity purifications.

4.2.3.5 SDS polyacrylamide gel electrophoresis (SDS-PAGE)

One-dimensional, discontinuous polyacrylamide gel electrophoresis (PAGE) enables separation of proteins from CCLs or immunopurifications according to their molecular weight (MW). The use of sodium dodecyl sulfate (SDS) causes denaturation of proteins and confers a negative surface charge [163,164]. Laemmli gels are composed of an upper stacking gel, which concentrates the protein samples, and a lower separating gel, where the separation process occurs. The polyacrylamide gel matrix is formed by crosslinking polymerization of acrylamide monomers with N,N'-methylene-bisacrylamide in the presence of radical starter APS and polymerization catalyst TEMED. For stacking gels, the final acrylamide concentration was 5%, whereas for separating gels acrylamide concentrations from 8% to 15% were used, depending on the MW of the respective proteins. CCLs after determination of protein concentration were adjusted 25 µg total protein per 20 µL using lysis buffer and 6 x SDS sample buffer. Samples obtained from immuno- or affinity purifications were mixed with an appropriate volume of 2 x SDS sample buffer. Samples were heated to 95 °C for 5 min and gels were loaded. A MW standard (Thermo Fisher Scientific) was used. Protein separation was carried out in SDS running buffer either at a constant current of 40 mA per mini gel (Bio-Rad) or of 100 mA per wide mini gel (Hoefer). Subsequently, gels were subjected to immunoblot analysis (see 4.2.3.6).

Stacking gel	1.0 M Tris/HCl, pH 6.8; 5% acrylamide; 0.74% (w/v) SDS; 0.1% TEMED; 0.1% APS
Separating gel	1.0 M Tris/HCl, pH 8.8; 6-15% acrylamide; 0.38% (w/v) SDS; 0.1% TEMED; 0.1% APS
SDS running buffer	250 mM Tris; 19 M glycine; 0.1% (w/v) SDS
2 x SDS sample buffer	125 mM Tris/HCl; 17.2% (v/v) glycerol; 4.1% (w/v) SDS; 2% (v/v) β-ME; 0.02% (w/v) bromophenol blue
6 x SDS sample buffer	375 mM Tris/HCl; 25.8% (v/v) glycerol; 12.3% (w/v) SDS; 6% (v/v) β-ME; 0.06% (w/v) bromophenol blue

4.2.3.6 Immunoblot analysis and densitometry

After completed SDS-PAGE, proteins were electrophoretically transferred onto polyvinylidene fluoride (PVDF) membranes for the subsequently performed detection by protein-specific antibodies. Blotting was performed in transfer buffer using a wet transfer unit (Bio-Rad) according to the manufacturer's instructions. PVDF membranes were activated prior to use by incubation in MeOH for 1 min. Proteins from SDS gels were transferred at a constant voltage of 100 V for 1 h at 4 °C. After completed transfer, the PVDF membranes were incubated in blocking solution for 1 h under constant agitation to prevent unspecific antibody binding. Afterwards, membranes were washed three times with TBS-T for 5 min and incubated with primary antibodies (1:1,000 in TBS-T containing 0.05% NaN_3) for 1 h at RT or at 4 °C over night under constant agitation. Membranes were washed three times with TBS-T for 5 min and incubated with appropriate IRDye® 680- or IRDye® 800-conjugated secondary anti-IgG antibodies (LI-COR Biosciences; diluted 1:10,000 to 1:20,000 in TBS-T) for 1 h at RT under constant agitation. Again, membranes were washed three times with TBS-T for 5 min and dried between gel blotting papers. Dry membranes were analyzed using an Odyssey® Infrared Imaging System I (LI-COR Biosciences) and densitometry was performed using Image Studio Light Version 4 (LI-COR Biosciences).

Transfer buffer	39 mM glycine; 43.58 mM Tris
TBS-T	0.05% (v/v) Tween® 20 in TBS
Blocking solution	5% (w/v) non-fat dried milk in TBS-T

4.2.3.7 Size exclusion chromatography

For size exclusion chromatography, 2 mg total protein or S100 cytoplasmic extracts were applied onto a *Superdex 200 Increase 10/300 GL* column (GE Healthcare). The column was calibrated with Thyroglobulin (669 kDa), Ferritin (440 kDa), Aldolase (158 kDa) and RNaseA (14 kDa). Proteins were eluted with washing buffer (50 mM Tris; 150 mM NaCl) at a flow rate of 0.5 mL/min. 0.5 ml fractions were collected. For quantification of protein levels in

each fraction, immunoblotting and densitometry were performed (see 4.2.3.6). Values are ratios to the input and were normalized to the fraction with the highest signal intensity.

4.2.3.8 Expression of recombinant proteins

pGEX-5x3 and pET-15b vectors encoding for NRBF2 variants were transfected in *E.coli* BL21. Bacteria were grown in SB medium to an optical density (OD_{600}) of 0.6 and protein expression was induced by addition of 1 mM IPTG. Bacteria were incubated at RT and mild agitation for 6 h and harvested by centrifugation at 5,000 rpm. For purification of GST fusion proteins, bacteria were lysed in bacterial LB. After 5 min incubation on ice, 0.5 mg/ml lysozyme was added and the suspension was additionally incubated for 30 min on ice before sonification and centrifugation at 10,000 rpm and 4 °C for 30 min. Lysates were incubated with glutathione sepharose at 4 °C overnight with rotation. The next day reactions were washed 3 times with bacterial lysis buffer and affinity-purified proteins were stored at -80 °C. Purification of 6xHis fusion proteins were performed in cooperation with the Institute of Biochemical Plant Physiology, Heinrich Heine University Düsseldorf, Germany. For purification, bacteria were resuspended in bacterial LB and cells were lysed by passing through a pre-cooled French pressure cell at 20,000 psi (1 psi = 6.9 kPa). Insoluble cell debris was separated by ultracentrifugation at 229,600 x g for 60 min and 4 °C. Phenylmethylsulfonyl fluoride (PMSF) was added at 0.002% (w/v) to the supernatant before loading at 4 °C on a 5 ml HisTrap HP column connected to an ÄKTAprime plus (both GE Healthcare Life Sciences). The column was washed with 50 mL lysis buffer, followed by 40 mL lysis buffer supplemented with 50 mM, 100 mM and 150 mM imidazole, respectively. The 6xHis fusion proteins were eluted in 40 mL elution buffer (lysis buffer containing 200 mM imidazole). The eluted proteins were concentrated (10-kDa-NMWL, Amicon Ultra-15, Merck) and buffer was changed to 50 mM Tris, pH 7.6; 300 mM NaCl and 0.002% (w/v) PMSF using a PD-10 column (GE Healthcare Life Sciences). Finally, the protein sample was centrifuged at 229,600 x g for 30 min at 4 °C to remove potential aggregates. The protein samples were stored at -80 °C.

SB medium	35 g/L tryptone; 20 g/L yeast extract; 5 g/L NaCl

Bacterial LB for GST fusion proteins	50 mM Tris, pH 7.5; 300 mM NaCl; 5 mM EDTA; 5 mM EGTA; 0.01% (v/v) Igepal; protease inhibitor cocktail
Bacterial LB for 6xHis fusion proteins	50 mM Tris, pH 7.6; 300 mM NaCl; 5% (w/v) glycerol; protease inhibitor cocktail; DNaseI (10 µg/mL)

4.2.3.9 *In vitro* kinase assay

For *in vitro* phosphorylation, 1 mg bacterially expressed GST or 6xHis fusion proteins were used as substrate and were incubated with either crude cellular lysates of HEK293 cells or 0.5 µg recombinant GST-ULK1. Reactions were performed in kinase assay reaction buffer supplemented with 0.1 mM [gamma-^{32}P]ATP (Hartmann Analytic) for 30 min at 37 °C. The reactions were stopped by the addition of SDS sample buffer and samples were subjected to SDS-PAGE (see 4.2.3.5). After Coomassie staining and drying of the gel (see 4.2.3.10), autoradiography was performed for the indicated times (see 4.2.3.11).

Kinase assay reaction buffer	50 mM Tris, pH 7.5; 0.1 mM EGTA; 0.1 mM DTT; 5 mM MgAc

4.2.3.10 Coomassie staining and drying of polyacrylamide gels

Visualization of protein bands after SDS-PAGE was achieved by Coomassie staining. Therefore, polyacrylamide gels were incubated in staining solution for 30 min at RT under gentle agitation. Gels were washed several times in destaining solution until protein bands were clearly visible.

Staining solution	50% (v/v) MeOH; 10% (v/v) HOAc; 0.5% (w/v) Coomassie® Brilliant Blue G-250
Destaining solution	20% (v/v) MeOH; 10% (v/v) HOAc

To obtain sharper signals during autoradiography, coomassie-stained polyacrylamide gels were dried prior to exposure to X-ray films. Therefore, gels were placed on a blotting paper covered with cellophane foil and placed in a gel-drying apparatus (Bio-Rad).

4.2.3.11 Autoradiography of polyacrylamide gels

Coomassie stained and dried polyacrylamide gels were placed in an autoradiography Hypercassette (GE Healthcare) exposed to X-ray film BioMax® MR (Kodak) for the indicated times. Until development, film cassette were stored at −80 °C. Development of X-ray films was done by incubation for 1 min in developing (AGFA) and fixation solution (AGFA).

4.2.3.12 *In vitro* PIK3C3 activity assay

The *in vitro* PIK3C3 activity assay has been described previously [38]. Briefly, class III PtdIns3K complex was immunopurified from 2 mg CCL using anti-ATG14 antibody. Immunopurified proteins were washed 3 times with lysis buffer, once with 2.5 x substrate buffer, resuspended in 1 x substrate buffer supplemented with 250 µg/mL PtdIns (Avanti Polar Lipids) and kept on ice for 10 min. After additional 5 min incubation at RT, kinase reactions were initiated by addition of 10 mM ATP (Cell Signaling Technology). Reactions were stopped after 30 min incubation at RT by spotting on nitrocellulose membrane (GE Healthcare). Membranes were blocked with 1% milk powder in DPBS for 1 h and incubated with 0.5 µg/ml of GST-p40PX (Echelon) in DPBS containing 3% BSA and 0.1% (v/v) Tween® 20 for 2 h. After 4 times washing with DPBS containing 3% BSA and 0.1% (v/v) Tween® 20, the membrane-bound amount of GST-p40PX was detected by development with anti-GST and IRDye®680-conjugated secondary antibody.

2.5 x substrate buffer	75 mM Tris, pH 7.5; 125 mM NaCl; 12.5 mM $MnCl_2$

4.2.3.13 Mass spectrometry (MS)

4.2.3.13.1 Mass spectrometric analysis of interacting proteins

These experiments were performed in cooperation with the Molecular Proteomics Laboratory, BMFZ, Heinrich Heine University Düsseldorf, Germany.

The samples for liquid chromatography (LC)-MS/MS analysis were concentrated by SDS-PAGE. After silver staining, corresponding protein bands were cut out, destained and dried in a vacuum centrifuge. Following two separate incubation steps with 10 mM DTT in 50 mM NH_4HCO_3 and 55 mM iodoacetamide in 50 mM NH_4HCO_3, samples were again dried in a vacuum centrifuge and either directly digested overnight at 37 °C by trypsin solution or stored at -20 °C.

Peptide extraction from gel samples was done by addition of extraction solution and subsequent incubation for 15 min in an ultrasonic bath. Supernatant was transferred to a new reaction tube, residual samples were resuspended again in extraction solution and mixtures were sonicated. Supernatant was removed, combined with the previous one and dried in a vacuum centrifuge. Samples were either resuspended in 0.1% TFA for LC-MS/MS analysis or stored at -20 °C.

For LC, an Ultimate 3000 liquid chromatography system (Dionex/Thermo Fisher Scientific) was used. Removal of contaminations and pre-separation of peptides was achieved on a precolumn (Acclaim PepMap C18, 100 µm inner diameter, 3 µm particle size, 100 Å pore size, 2 cm length, Thermo Fisher Scientific). Sample separation was performed on the main analytical column (Acclaim PepMap C18, 75 µm inner diameter, 2 µm particle size, 100 Å pore size, 25 cm length, Thermo Fisher Scientific) and separated by a 60 min gradient. Following LC, samples were ionized via a nanoelectrospray ion source and analyzed by a hybrid ion trap-orbitrap mass spectrometer (Orbitrap Elite, Thermo Fisher Scientific). The ion source was operated at 1.4 kV and capillary temperature was maintained at 275 °C. Single-charged ions were excluded from fragmentation and data acquisition was performed in a top 15 data-dependent mode, where the fifteen most intensive signals of an overview scan were selected, isolated and fragmented again.

Raw data were analyzed with MaxQuant v. 1.3.0.5 [165] and spectra were matched against human UniProtKB/SwissProt database (date 06/2013). Further analysis was performed with Perseus v. 1.4.0.20. Proteins, which were not identified in all replicates were removed. Differential interaction partners were identified by *t* test (*P* value ≤ 0.05).

4.2.3.13.2 Mass spectrometric analysis of phosphorylation status

These experiments were performed in cooperation with the Institute of Cardiovascular Physiology, Heinrich Heine University Düsseldorf, Germany.

In vitro kinase assays were performed as described above (see 4.2.3.9) with minor modifications. An amount of 5 mg GST fusion protein and 1 µg recombinant GST-ULK1 were used. Instead of [^{32}P]ATP, 0.5 mM non-radioactive ATP was used. After 30 min incubation, samples were subjected to mass spectrometry.

Acetone precipitation of protein samples was performed for 4 h at -20 °C. After incubation, the proteins were resuspended in 40 mM ammonium bicarbonate and digested with trypsin (Promega, trypsin:protein ratio 1:100) over night at 37 °C. Instead of acetone precipitation, one sample was treated by ethyl acetate extraction [166] after digestion. Peptide samples were concentrated in vacuum. Peptide separation was performed on an UltiMate3000 LC system (Thermo Fisher Scientific). After concentration on a 100 µm ID reversed-phase (RP) precolumn (in-house packed, ReproSil-Pur C18-AQ 3 µm resin, Dr. Maisch GmbH), peptides were loaded on a 75 µm ID x 18 cm column (in-house packed, ReproSil-Pur C18-AQ 3 µm resin, Dr. Maisch GmbH) with solvent A (0.1% formic acid) and were separated with a binary gradient (solvent B: 0.1% (v/v) formic acid in 84% (v/v) acetonitrile) at a flow rate of 230 nL/min: 2-40% solvent B in 65 min and 40-98% solvent B in 5 min.

Peptides were directly eluted into the nanoelectrospray ion source of an LTQ orbitrap instrument (Thermo Fisher Scientific). The ion source was operated at 1.5 V and the capillary temperature was maintained at 200 °C. Data acquisition was performed in data dependent mode. First, a full scan (m/z 350-2000, automatic gain control target value of 1e^6, resolution r = 60,000 at m/z 400) was performed in the orbitrap analyzer. MS/MS

spectra of the ten most intense multiple charged ions were sequentially acquired in the linear ion trap by collision induced dissociation (normalized collision energy 35%, automatic gain control 5,000 ions). A dynamic exclusion of 30 s reduced repeated sequencing events. Multistage activation was enabled using neutral loss masses of 98, 65, 49 and 32.6 Da.

Raw data were analyzed with MaxQuant v. 1.5.3.30 [165]. MS/MS spectra were matched against protein sequences of generated fusion proteins and human ULK1 (Swiss-Prot 2016_08) with default search parameters unless otherwise stated. The search included phosphorylation of serine, threonine and tyrosine, oxidation of methionine and acetylation of protein N-termini as variable modifications. Phosphorylated peptides were considered as validated if a score greater than 40 and a posterior error probability score (PEP) less than 0.01 were given. Only phosphorylation sites with a localization probability score over 0.75 were accepted as unambiguous sites.

4.2.3.14 Gene expression analysis by microarray

These experiments were performed in cooperation with the Genomics & Transcriptomics Laboratory, BMFZ, Heinrich Heine University Düsseldorf, Germany.

Total RNA preparations were checked for RNA integrity by Agilent 2100 Bioanalyzer quality control. All samples in this study showed high quality RNA Integrity Numbers (RIN: mean = 9.9). RNA was further analysed by photometric Nanodrop measurement and quantified by fluorometric Qubit RNA assays (Life Technologies).

Synthesis of biotin labeled cDNA was performed according to the manufacturers´ protocol (WT Plus Reagent Kit; Affymetrix, Inc.). Briefly, 100 ng of total RNA were converted to cDNA. After amplification by *in vitro* transcription and 2nd cycle synthesis, cDNA was fragmented and biotin labeled by terminal transferase. Finally, end labeled cDNA was hybridized to Affymetrix Mouse Gene 2.0 ST Gene Expression Microarrays for 16 h at 45 °C, stained by streptavidin/phycoerythrin conjugate and scanned as described in the manufacturers´ protocol.

Data analyses on Affymetrix CEL files were conducted with GeneSpring GX software (Vers. 12.5; Agilent Technologies). Probes within each probeset were summarized by GeneSprings´ ExonRMA16 algorithm after quantile normalization of probe level signal intensities across all samples to reduce inter-array variability [167]. Input data pre-processing was concluded by baseline transformation to the median of all samples.

To further improve signal-to-noise ratio, a given probeset had to be expressed above background (i.e. fluorescence signal of a probeset was detected within the 20th and 100th percentiles of the raw signal distribution of a given array) in all three replicates in at least one of two, or both conditions to be subsequently analyzed in pairwise comparisons.

Differential gene expression was statistically determined by moderated *t* tests. If applicable, resulting *P*-values were corrected for multiple testing (Benjamini-Hochberg FDR). The significance threshold was set to $P = 0.05$ or $P_{(corr)} = 0.05$, respectively. GeneOntology (GO) analyses were done using the DAVID Functional Annotation Tool (http://david.abcc.ncifcrf.gov/) [168] testing for enrichment of differentially expressed transcripts in distinct functional GO categories / KEGG pathways. Significant GO term or pathway enrichment were determined at an EASE score of $P < 0.1$.

5 Results

5.1 Identification of NRBF2 as part of the class III PtdIns3K complex and characterization of its role in autophagy

5.1.1 Mass spectrometric identification of BECN1-interacting proteins

Molecular signaling networks are characterized by a complex organization and a large interconnectivity of the individual proteins. A frequently used way to regulate cellular signal transduction is the assembly and subsequent breakup of signaling proteins into larger complexes [169]. Extensive crosstalk between different signaling pathways enables a dynamic and fast regulation of diverse cellular processes. This also applies for the connection of autophagy and apoptosis signaling cascades, where the PtdIns3K-Bcl-2 interaction represents an important signaling node for both pathways (see 2.1.2.2).

This work aimed for the identification of novel regulatory proteins of the autophagy signaling network based on the class III PtdIns3K complex. Potential candidates identified by mass spectrometric analysis were further characterized for their specific roles in autophagy. To accomplish this task, a label-free protein enrichment and subsequent identification by mass spectrometry was performed. BECN1 as essential subunit of the class III PtdIns3K complex was generated as a GFP fusion protein to be used as a bait and subsequent enrichment of interacting proteins was performed by the GFP-Trap® system (ChromoTek). For further detection of cell-type dependent differences, BECN1-GFP was expressed in an epithelial (HEK293) and a lymphatic (DG75) human cell line. To discriminate unspecific binding, free GFP was used as control. The successful expression of these proteins was verified and the results are depicted in figure 5.1.

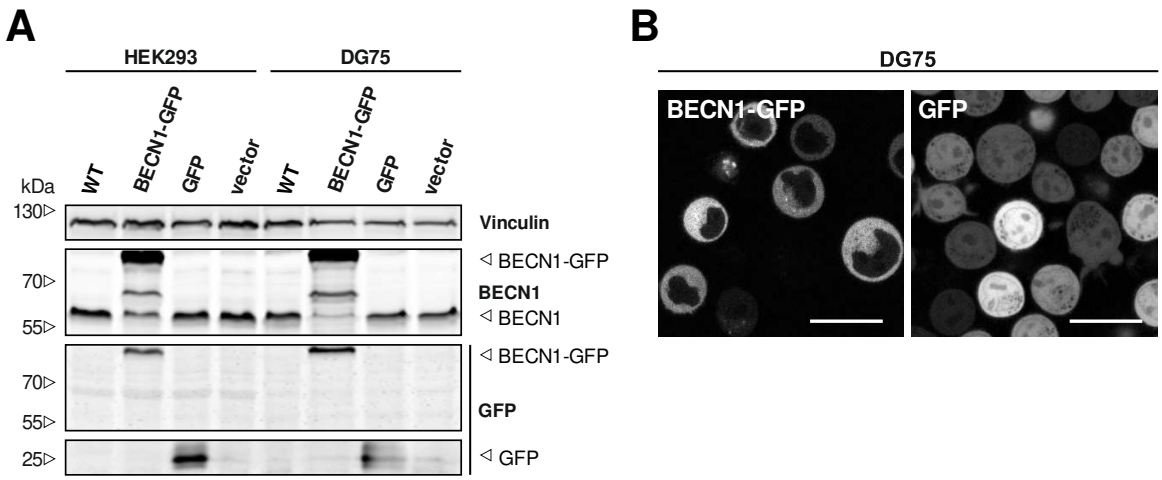

Figure. 5.1: The human cell lines HEK293 and DG75 stably express BECN1-GFP. (A) Wild type (WT) HEK293 and DG75 cells were retrovirally transfected with either empty vector or cDNA encoding for BECN1-GFP or GFP. Cleared cellular lysates were prepared and analyzed by immunoblotting for vinculin, BECN1 and GFP. (B) DG75 cells retrovirally transfected with cDNA encoding for either BECN1-GFP or GFP were transferred to chambered cover glasses and directly used for detection of GFP fluorescence by confocal microscopy. Imaging was performed using an inverse confocal laser scanning microscope. Scale bar: 20 µm.

Immunoblot analysis for GFP displayed a single protein band above 70 kDa for cells transfected with cDNA encoding for BECN1-GFP. This band correlates with the calculated theoretical molecular mass of ca. 81 kDa of the BECN1-GFP fusion protein. Expression of free GFP was detectable in cells transfected with cDNA encoding for GFP, indicated by a protein band detected at 25 kDa. Additional analysis for BECN1 confirmed expression of endogenous BECN1 in each cell line, demonstrated by corresponding bands above 55 kDa. In addition, cells transfected with BECN1-GFP displayed a strong signal, corresponding again to the BECN1-GFP fusion protein. In these samples, additional bands were detected below 70 kDa and the signal for endogenous BECN1 seemed reduced (Fig 1 A). Additional analysis of GFP-fluorescence by confocal microscopy was done exemplarily for DG75 cells. Localization of BECN1-GFP is restricted to the cytosol and no fluorescence signal was detected in the nuclei. On the contrary, free GFP was detected ubiquitously inside the cells (Fig 5.1 B).

After the expression of BECN1-GFP and free GFP was validated in both cell lines, samples for mass spectrometric analysis were prepared. Therefore, cells were incubated in full

medium (DMEM and RPMI for HEK293 and DG75 cells, respectively) or in starvation medium lacking serum (EBSS) as pro-autophagic stimulus. This treatment was performed for 1 h on DG75 and for 2 h on HEK293 cells. Subsequently, cleared cellular lysates were prepared, 25 mg total protein was used for GFP immunopurifications and the samples were analyzed by mass spectrometry (Molecular Proteomics Laboratory, BMFZ, Heinrich Heine University Düsseldorf). For statistical evaluation, experiments were performed in triplicates and the obtained mass spectrometric results and a further validation of identified interacting proteins is shown in figure 5.2.

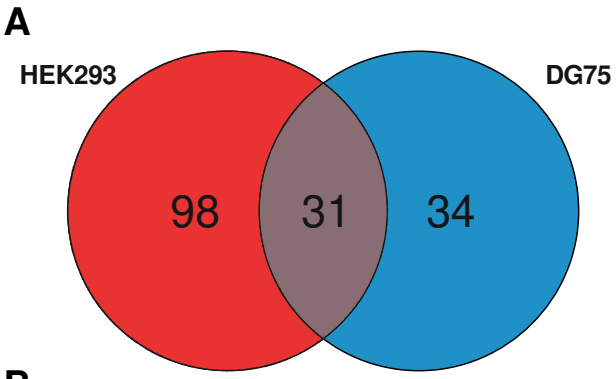

B

		HEK293		DG75	
protein name	gene symbol	fold change	t-test significance	fold change	t-test significance
Beclin 1-associated autophagy-related key regulator	*ATG14*	3128	*** (2.61E-04)		
Tuberous sclerosis 1 (Hamartin)	*TSC1*	42	** (8.43E-03)		
Tuberous sclerosis 2 (Tuberin)	*TSC2*	16	** (1.44E-03)		
Phosphoinositide 3-kinase regulatory subunit 4	*PIK3R4*	54965	*** (3.47E-05)	10792	** (8.94E-03)
Phosphatidylinositol 3-kinase catalytic subunit type 3	*PIK3C3*	15552	*** (5.32E-04)	2169	*** (6.34E-03)
Beclin 1	*BECN1*	15008	*** (1.85E-04)	3605	** (3.28E-04)
UV radiation resistance-associated protein	*UVRAG*	1626	*** (9.15E-05)	1160	** (1.27E-03)
Nuclear receptor-binding factor 2	*NRBF2*	700	*** (5.41E-04)	121	** (5.97E-03)
Run domain Beclin-1 interacting and cystein-rich containing protein	*RUBCN*	152	*** (5.47E-04)	104	* (1.61E-02)
14-3-3 protein zeta / delta	*YWHAQ*			6.4	* (1.39E-02)
14-3-3 protein theta	*YWHAZ*			1.55	* (4.6E-02)

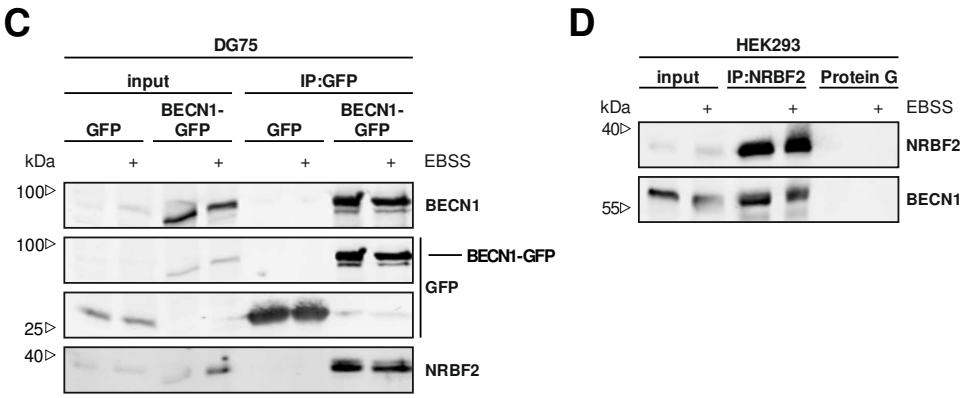

Figure. 5.2: Identification and validation of BECN1-interacting proteins. (A) Number of proteins significantly enriched by BECN1-GFP purification for HEK293 and DG75 cells after medium treatment Results are depicted as Venn diagrams. 98 proteins were identified exclusively for HEK293 cells and 34 exclusively for DG75 cells. An overlap of 31 proteins was identified for both cell

lines. (B) Based on low p-values in combination with high fold change ratios between BECN1-GFP and GFP, a hierarchic list of identified proteins was created considering all identified proteins. (C) DG75 cells retrovirally transfected with cDNA encoding either for BECN1-GFP or GFP were incubated for 1 h in full medium (RPMI) or starvation medium (EBSS). Cleared cellular lysates were prepared, GFP immunopurifications were performed overnight and samples were analyzed by immunoblotting for BECN1, GFP and NRBF2. (D) Wild-type HEK293 cells were incubated for 2 h in full medium (DMEM) or starvation medium (EBSS). Cleared cellular lysates were prepared, NRBF2 immunopurifactions using antibody covalently coupled to protein G sepharose were performed overnight and samples were analyzed by immunoblotting for BECN1 and NRBF2.

Mass spectrometric analysis identified a total number of 163 proteins, which were significantly enriched by pulldown of BECN1-GFP from cells treated with medium. Of these, 98 proteins were identified exclusively in lysates from HEK293 cells, 34 exclusively in lysates from DG75 cells, and 31 for both cell lines (Fig 5.2, A). By arranging identified proteins according to low p-values in combination with high fold change ratios between BECN1-GFP and GFP, a hierarchic list was created (Fig 5.2, B). Identification of established BECN1-interacting proteins was achieved in both cell lines. The class III PtdIns3K complex members PIK3R4, PIK3C3, BECN1, UVRAG and RUBCN were identified as strongest interacting proteins, and solely for ATG14 no significant enrichment was detected in DG75 samples. Among the other identified proteins, nuclear receptor-binding factor 2 (NRBF2) displayed the highest enrichment scores in both cell lines and was therefore chosen for further characterization for its role in autophagy. So far, NRBF2 has been identified by a large-scale proteomic analysis of autophagy interaction networks [170], but no further characterization has been carried out in that report. Among others, the regulators of mTORC1-signaling hamartin (TSC1) and tuberin (TSC2) or distinct members of the 14-3-3 scaffold and adapter protein family [171] were identified exclusively in HEK293 or DG75 cells, respectively. For further biochemical validation of the detected BECN1-NRBF2 interaction, co-immunopurification experiments were performed. Purification of GFP-tagged BECN1 from DG75 cells expressing BECN1-GFP resulted in a clear co-purification of NRBF2 (Fig 5.2, C). Validation of the BECN1-NRBF2 protein interaction by immunopurification of endogenous NRBF2 from HEK293 cells also confirmed these results. Anti-NRBF2 antibody covalently coupled to protein G sepharose was able to co-purify BECN1, which was not the case for protein G sepharose without antibody (Fig 5.2, D).

5.1.2 Generation of a NRBF2 knockout DT40 cell line and characterization of NRBF2 as positive regulator of autophagy

To study the importance of a specific protein in a cellular context, the generation of a corresponding genetic knockout cell system is often favored [172]. For further characterization of NRFB2 and its functional role in autophagy, such a genetic knockout approach was performed in this thesis. For that, the DT40 cell system was used, since other systems like ZFNs and TALENs were not applicable and the CRISPR/Cas9 system was not established at that time. The DT40 cell line is a chicken B cell line derived from an avian leucosis virus (ALV) induced bursal lymphoma [155]. One unique feature that enables their use as a tool for the generation of cellular knockout systems is an elevated ratio of targeted to random recombination events and thereby the specific integration of foreign DNA [157]. The applied genetic targeting strategy and the subsequent screening of DT40 clones for NRBF2 deficiency is depicted in figure 5.3.

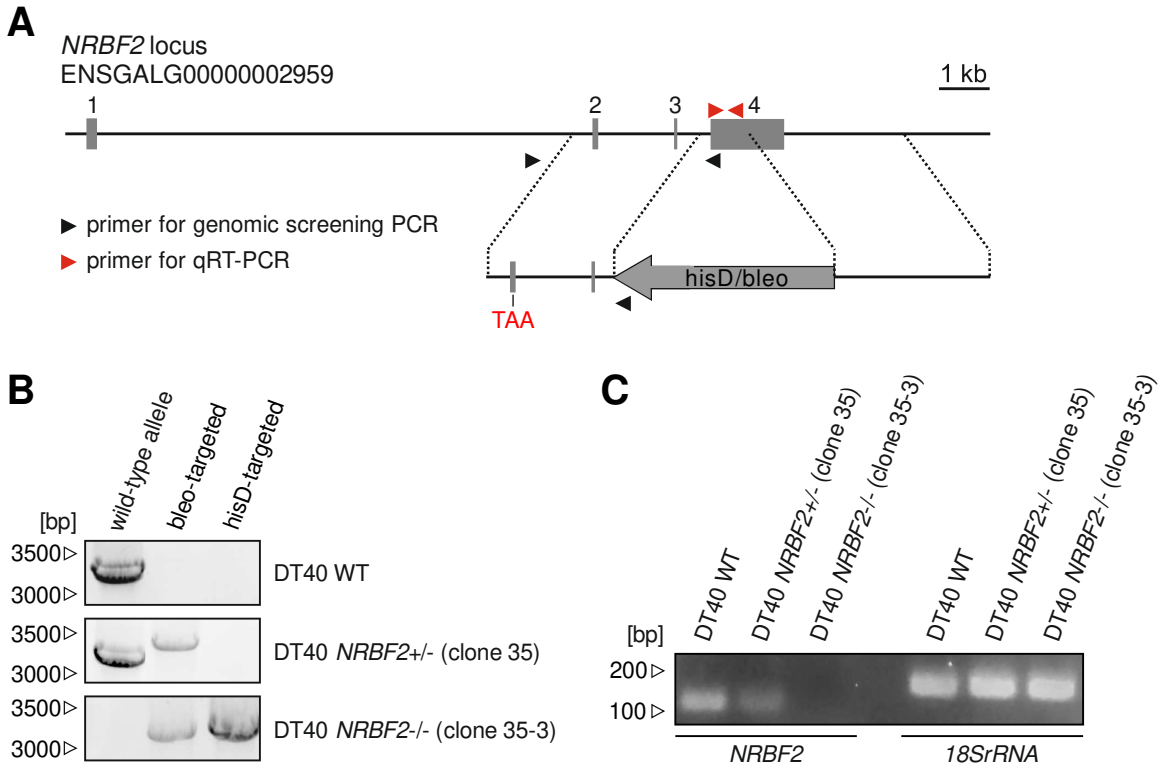

Figure. 5.3: Targeting strategy and screening of DT40 cells genetically deficient for NRBF2. (A) Targeting vectors were designed to replace parts of exon 4 of both alleles of chicken *NRBF2* (ENSGALG00000002959) gene by insertion of a bleomycin (bleo) or histidinol (hisD) resistance cassette. Additionally, a premature stop codon was integrated in exon 2. Locations of primers for genomic screening PCR and qRT-PCR are annotated. (B) Successful targeting of both *NRBF2* alleles was tested by genomic screening PCR using primers for wild-type, bleo- or hisD-targeted alleles.

One heterozygous clone (35) was subjected to a next round of transfection and selection, resulting in the establishment of one homozygous clone (35-3) lacking both *NRBF2* wild-type alleles. (C) Presence of *NRBF2* mRNA in wild-type, heterozygous targeted and homozygous targeted DT40 cells was analyzed by qRT-PCR. *18SrRNA* was used as control.

The used targeting plasmids were designed to replace a 756 bp region at the 5' end of exon 4 of chicken *NRBF2* gene by two resistance cassettes. Additionally, a premature stop codon was integrated in exon 2. To favor homologous recombination events, up- and downstream sequences of the targeted DNA region were amplified and placed flanking the resistance cassettes in the targeting plasmids (Fig 3 A). Wild-type DT40 cells were transfected with the first targeting vector by electroporation and cultured under corresponding antibiotic selection. After detection of successful integration of the first resistance cassette, a second round of transfection and selection was performed using the second targeting plasmid. Confirmation of successful replacement of the wild-type allele was assessed by genomic screening PCR (Fig 3 B). In addition, absence of *NRBF2* mRNA was controlled by real-time quantitative reverse transcription PCR (qRT-PCR, Fig 3 C). Conclusively, a NRBF2-deficient DT40 cell line was generated successfully and was used for further analysis of the physiological role of NRBF2.

A standard method to monitor the overall autophagic flux is to measure the conversion from the cytosolic form of LC3 (LC3-I) into its membrane-associated form LC3-II, e.g. by immunoblotting [173]. Thus, cellular LC3-II levels correlate with the number of autophagosomes present at a defined time point. To further differentiate the obtained results with regard to effects related to synthesis or degradation processes, starvation is used as pro-autophagic stimulus and the V-ATPase inhibitor bafilomycin A_1 ($BafA_1$) is used to block lysosomal degradation processes [174]. For the detection of effects specifically related to NRBF2 deficiency, *NRBF2*-/- DT40 cells were retrovirally transfected with either empty vector of cDNA encoding for human NRBF2. These cells were used for analysis of LC3-turnover (Fig 5.4).

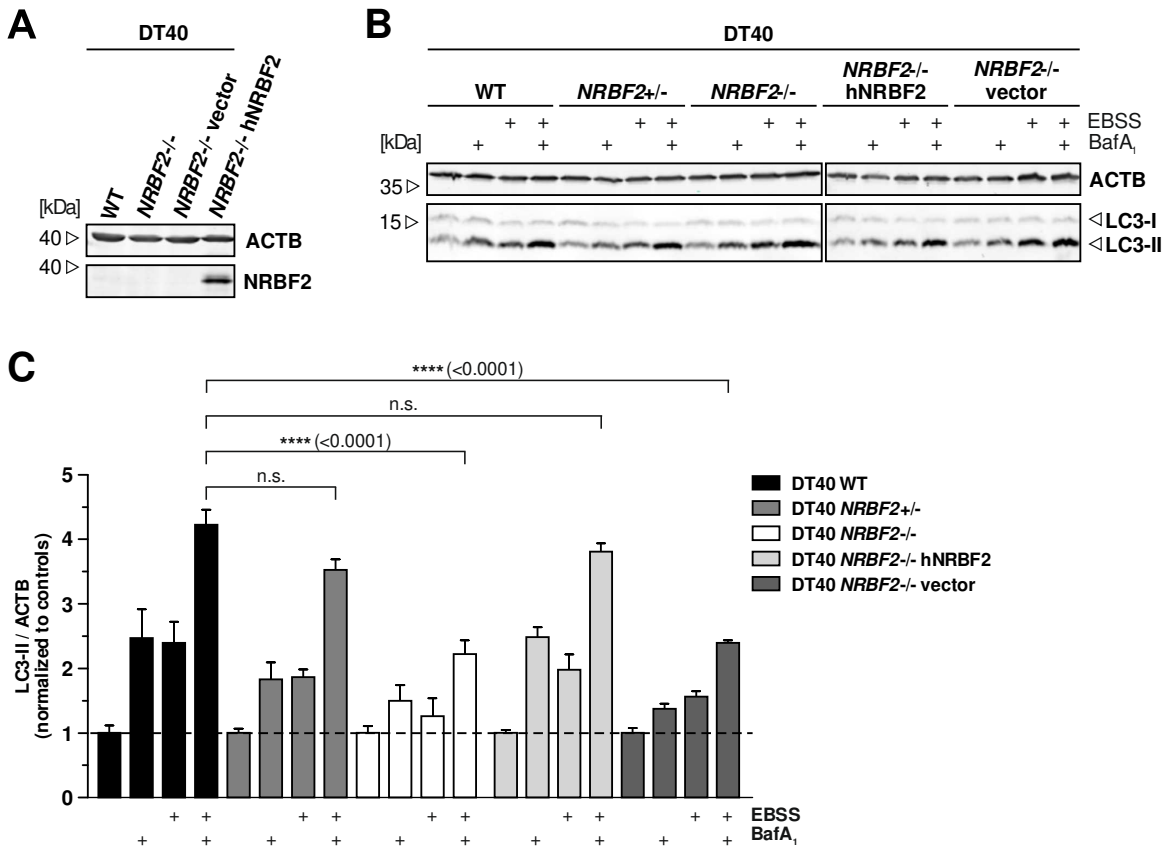

Figure 5.4: Measurement of autophagic capacity in DT40 cells lacking NRBF2. (A) DT40 wild-type (WT) or *NRBF2*-/- cells either untransfected or retrovirally transfected with empty vector or cDNA encoding for human NRBF2 were analyzed for NRBF2 expression by immunoblotting. Cleared cellular lysates were prepared and analyzed for actin and NRBF2. Detection of endogenous chicken NRBF2 in DT40 wild-type cells with applied antibody is not possible. (B) The annotated cell lines were incubated for 1 h in full medium (RPMI) or starvation medium (EBSS) in the absence or presence of 10 nM bafilomycin A_1 ($BafA_1$). Cleared cellular lysates were prepared and analyzed for ACTB and LC3. (C) Signal intensities of immunoblots were quantified. Diagrams show fold changes calculated by dividing each normalized ratio (protein to loading control) by the average of the normalized ratios of the control samples (medium conditions without $BafA_1$). Results are mean ± SEM. Statistical analysis was done by one-way ANOVA (corrected by Tukey's multiple comparisons test), n.s. not significant, ****P < 0.0001. n = 3. Only significant differences for EBSS/$BafA_1$ are annotated. A complete list of P values for all calculated significant differences can be found in the addendum.

Antibody-based detection of endogenous NRBF2 from DT40 wild-type cells was not possible. Amino acid sequence alterations of chicken NRBF2 hampered antibody binding, whereas human NRBF2 was detected successfully after reconstitution (Fig 5.4 A). The immunoblot analysis displayed two distinct signals for LC3, the upper one at 15 kDa corresponding to the cytosolic form (LC3-I) and the lower one to its lipidated form (LC3-II).

A functional autophagic flux, characterized by the respective increase of LC3-II following $BafA_1$ or EBSS treatment, could be detected for each cell line (Fig 5.4, B). For a better evaluation, quantification of signal intensities and normalization to the respective medium conditions was done (Fig 5.4, C). Here, an influence of NRBF2 deficiency on the maximal amplitude of LC3-II accumulation represented by combination treatment with EBSS and $BafA_1$ was detected. Absence of NRBF2 causes a reduction of about 50% of normalized LC3-II levels for EBSS + $BafA_1$ treatment compared to wild-type cells. Cells lacking one functional *NRBF2* allele already displayed a significant reduction of LC3-II compared to wild-type DT40 cells. Reconstitution with cDNA encoding for human NRBF2 reversed the observed alterations and no significant differences were detected anymore. In contrast, vector transfected cells still displayed the phenotype caused by NRBF2 deficiency.

Taken together, these experiments following the identification of NRBF2 as a novel BECN1-interacting protein indeed attributed a role to NRBF2 as a positive regulator of starvation-induced autophagy. Additional experiments for a detailed elucidation of how exactly NRBF2 affects the autophagic flux or which structural domains of NRBF2 mediate the interactions with the class III PtdIns3K complex were planned. However, three independent groups simultaneously published comprehensive analyses of NRBF2 and its involvement in autophagy [53–55]. Accordingly, two alternative aspects of NRBF2 signaling were investigated in more detail:

1) the involvement of NRBF2 in the transcriptional control of autophagy-related and other genes

2) posttranslational modification of NRBF2 by phosphorylation.

5.2 NRBF2 interacts with the nuclear receptor PPAR alpha and is involved in the transcriptional control of various genes

5.2.1 NRBF2 interacts with the nuclear receptor PPAR alpha

Rat NRBF2 was initially characterized in a yeast two-hybrid screen as an interacting partner of nuclear receptors, displaying a gene-activating function [175]. Later on, a human homolog was identified and named comodulator of PPAR and RXR (COPR2) [176], albeit the name COPR2 did not prevail. In 2010, the previously mentioned large-scale proteomic analysis of autophagy interaction networks by Behrends et al. located NRBF2 as a member of the autophagy regulation network [170]. Subsequently, Lee and coworkers reported that the nuclear receptors peroxisome proliferator-activated receptor-alpha (PPAR alpha) and the farnesoid X receptor (FXR) regulate gene expression of a large set of autophagy related genes. They observed an activation of PPAR alpha in the liver of fasted mice and furthermore, a reversal of suppressed autophagy in the fed state by pharmacological activation of PPAR alpha [129]. Moreover, two other research groups independently demonstrated that pharmacological activation of PPAR beta/delta and PPAR gamma also causes an increase in autophagy related marker proteins (BENC1 and LC3-II) and enhances autophagy dependent degradation processes [177,178]. These findings led to the hypothesis that the execution and transcriptional regulation of autophagy are possibly interconnected by NRBF2.

Thus, the second part of this thesis aimed for a further elucidation if NRBF2 indeed functions as a link between short time (e.g. execution of autophagic flux) and long time (e.g. transcription of autophagy related genes) control of autophagy. The postulated interaction of NRFB2 and nuclear receptors and a putative role for NRBF2 in transcriptional regulation was explored in further experiments. Therefore, results of the original yeast two-hybrid experiments were validated by several co-immunopurification approaches. In addition, the subcellular localization of NRBF2 and putative influences of PPAR-stimulation on protein and gene expression was monitored.

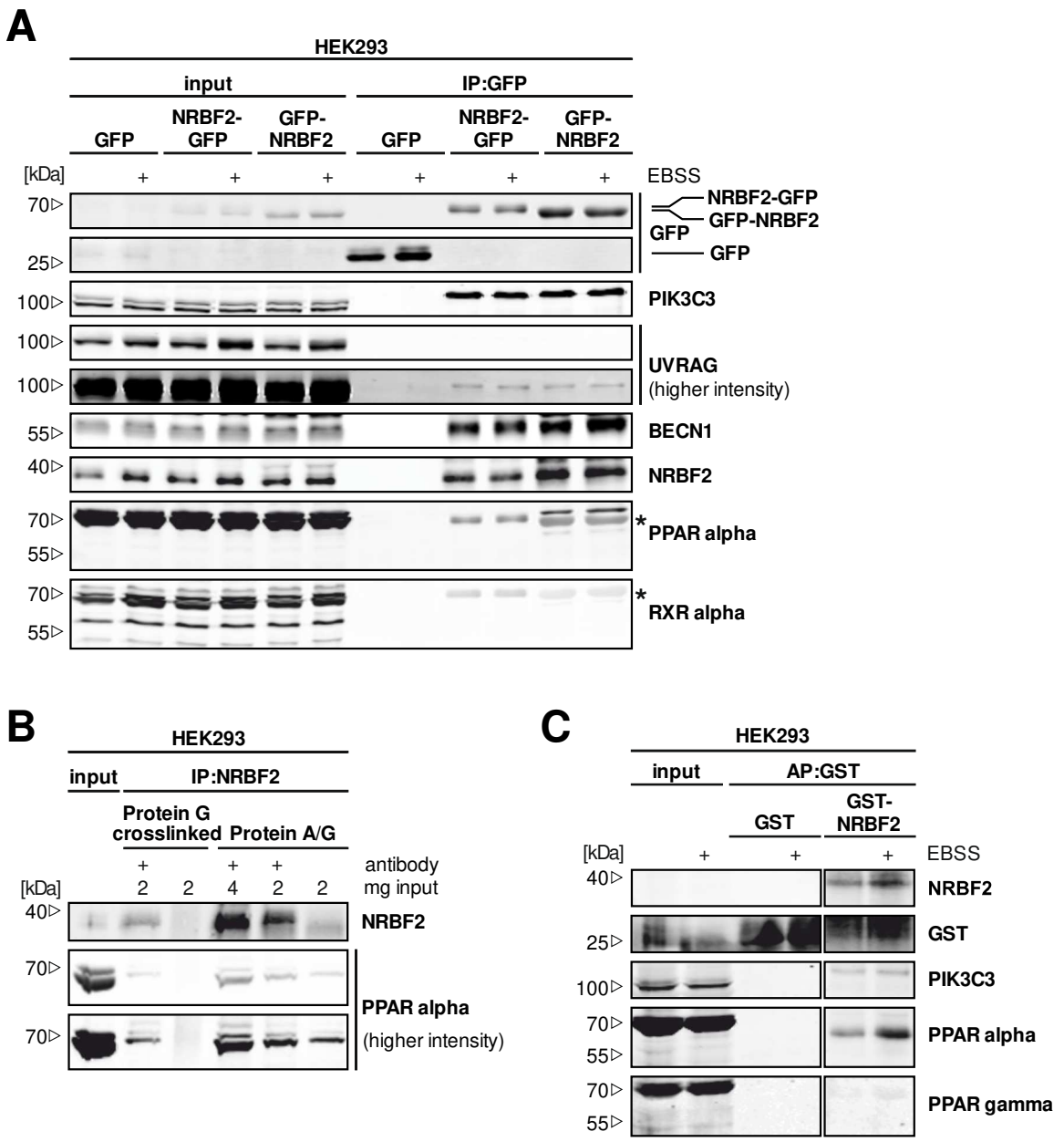

Figure 5.5: NRBF2 interacts with the nuclear receptor PPAR alpha. (A) HEK293 cells retrovirally transfected with cDNA encoding for either GFP or NRBF2 harboring a C-terminal (NRBF2-GFP) or an N-terminal GFP tag (GFP-NRBF2) were incubated for 2 h in full medium (DMEM) or starvation medium (EBSS). Cleared cellular lysates were prepared, GFP immunopurifactions were performed overnight and samples were analyzed by immunoblotting for GFP, PIK3C3, UVRAG, BECN1, NRBF2, PPAR alpha and RXR alpha. Asterisks indicate unspecific bands. (B) Cleared cellular lysates of wild-type HEK293 cells were prepared and NRBF2-immunopurifactions were performed overnight. The NRBF2 antibody was either covalently coupled to protein G sepharose or mixed with protein A/G sepharose without crosslinking. Samples were analyzed by immunoblotting for NRBF2 and PPAR alpha. (C) Cleared cellular lysates of wild-type HEK293 cells were prepared and incubated overnight with GST-only or GST-NRBF2, respectively. Samples were analyzed by immunoblotting for NRBF2, GST, PIK3C3, PPAR alpha and PPAR gamma.

Co-immunopurification experiments using lysates from HEK293 cells transfected with either GFP, NRBF2-GFP or GFP-NRBF2 showed successful co-purification of the class III PtdIns3K complex proteins PIK3C3, UVRAG, BECN1 and NRBF2 for both fusion proteins. No co-immunopurification was detectable for free GFP. Notably, only GFP-NRBF2 was able to co-purify PPAR alpha, but not RXR alpha (Fig 5.5 A). Immunopurification of endogenous NRBF2 from wild-type HEK293 cells with or without crosslinking of the antibody again resulted in successful co-purification of PPAR alpha (Fig 5.5, B). Finally, interaction of NRBF2 with PPAR alpha, but not with PPAR gamma was confirmed by co-affinity purification from lysates of wild-type HEK293 cells using recombinant GST-NRBF2 (Fig 5.5, C).

A further requirement for a transcription factor to control gene expression is a temporal nuclear localization to enable interaction with either DNA or DNA-bound regulatory proteins [179]. To enable this localization, nuclear import can occur either by active or by passive transport [180]. Therefore, the subcellular localization of NRBF2 was investigated by confocal microscopy (Fig 5.6).

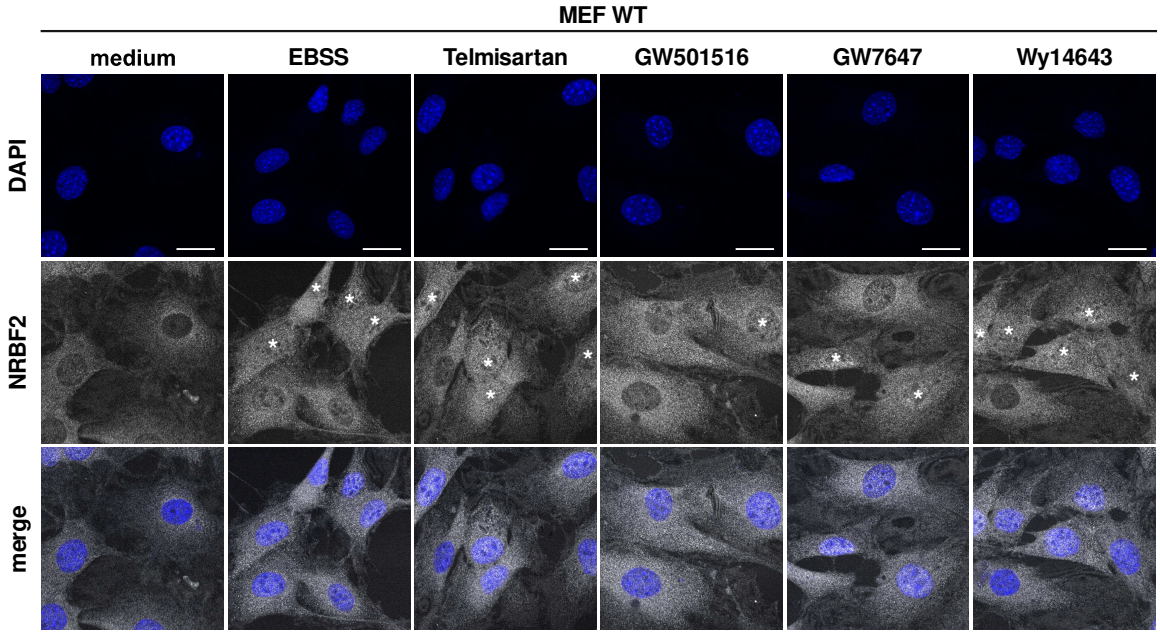

Figure5.6: Subcellular localization of NRBF2 by immunofluorescence. Wild-type MEFs were grown on glass cover slips overnight and incubated either in full medium (DMEM), in starvation medium (EBSS) for 2 h or in medium supplemented with pharmacological activators for PPAR gamma (Telmisartan, 20 µM), PPAR beta/delta (GW501516, 20 µM) or PPAR alpha (GW7647, 1 µM and Wy14643, 100 µM) for 24 h. Cells were fixed, permeabilized and immunostained for NRBF2 and nuclei were stained with DAPI. Imaging was performed using an inverse confocal laser scanning microscope. Asterisks indicate strong nuclear accumulation of NRBF2. Scale bar: 50 µm.

Wild-type MEF cells were incubated in full medium, EBSS or medium supplemented with pharmacological activators of PPAR gamma (Telmisartan), beta/delta (GW501516) and alpha (GW7647 and Wy14643). After staining of endogenous NRBF2 these cells were analyzed by confocal microscopy. Signal intensity of NRBF2-immunostaining was not very high. Nevertheless, NRBF2 signal was detected in the cytoplasm and to a lower extent in the nucleus after treatment with full medium. Administration of either EBSS-starvation or PPAR-stimulation caused an increase in nuclear localization of NRBF2 (Fig 6).

5.2.2 NRBF2-is involved in the regulation of protein and gene expression

Following the detection of the interaction between NRBF2 and PPAR alpha and the nuclear localization of NRBF2, the physiological relevance of these findings was examined. As stated under 5.2.1, several groups reported upregulation of the autophagy related proteins BECN1 and LC3-II after pharmacological stimulation of PPAR activity. To test a putative involvement of NRBF2 in these processes, the described pharmacological activation of PPARs was performed during cell culturing of diverse cell lines and effects on ULK1, BECN1 and LC3 protein levels were monitored. In a first experiment, the murine hepatocyte cell line alpha mouse liver 12 (AML12), which is an established physiological model for PPAR-activation [129], was used. Subsequently, effects of PPAR-activation were transferred to MEF cells deficient for NRBF2 in order to highlight effects specifically mediated by NRBF2. Results of these experiments are displayed in figure 5.7.

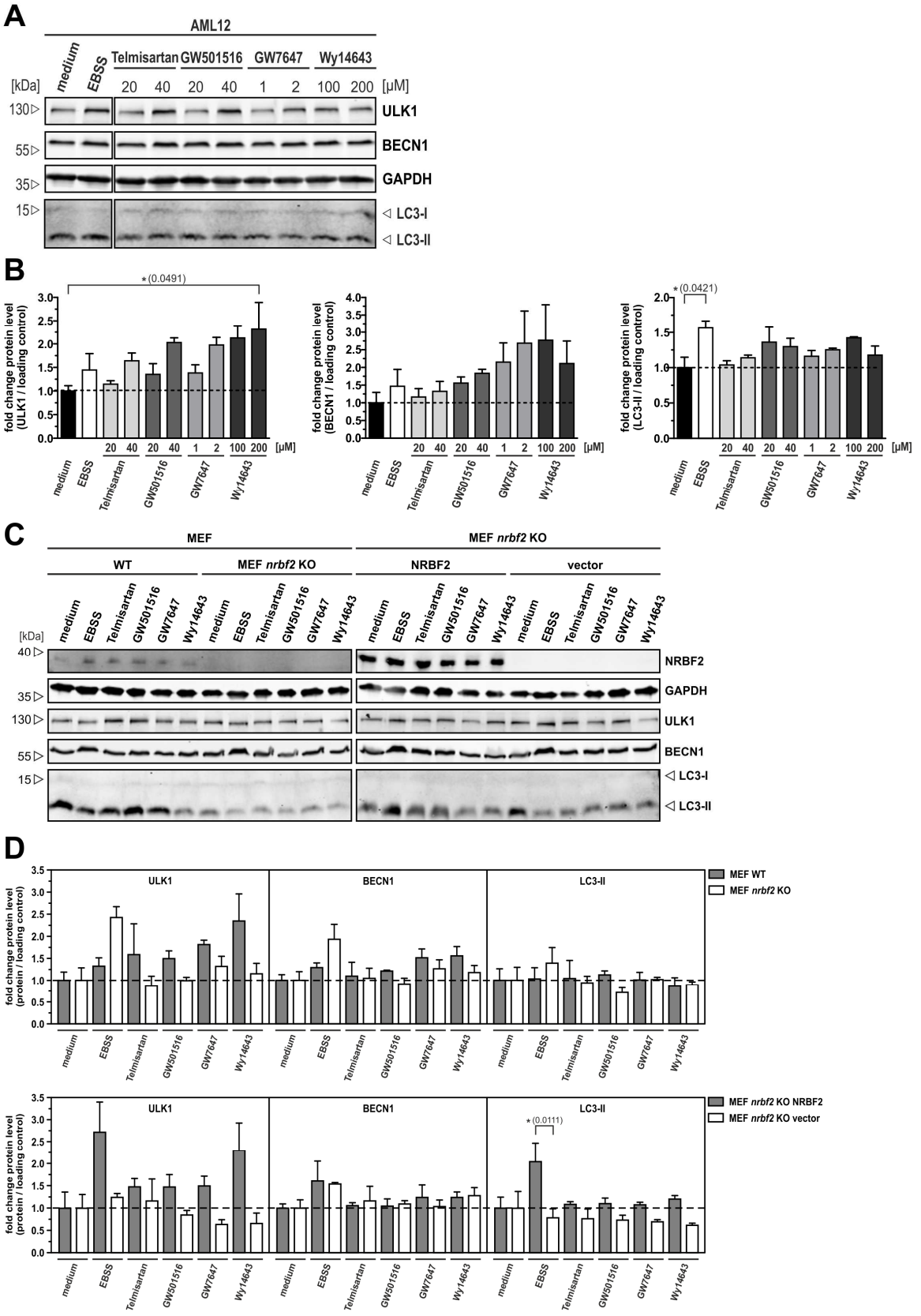

Figure 5.7: Regulation of autophagy related protein levels after pharmacological activation of the PPAR family is partially NRBF2-dependent. (A) AML12 cells were incubated either in full medium (DMEM:F12), in starvation medium (EBSS) for 2 h or in full medium supplemented with pharmacological activators for PPAR gamma (Telmisartan), PPAR beta/delta (GW501516) or PPAR

alpha (GW7647 and Wy14643) at the indicated concentrations for 24 h. Cleared cellular lysates were prepared and analyzed by immunoblotting for ULK1, BECN1, GAPDH and LC3. (B) Signal intensities of immunoblots were quantified. Diagrams show fold changes calculated by dividing each normalized ratio (protein to loading control) by the average of the normalized ratio of the control sample (medium conditions). Results are mean ± SEM. Statistical analysis was done by one-way ANOVA (corrected by Tukey's multiple comparisons test), *P < 0.05. n = 3. (C) MEF wild-type (WT) or *nrbf2* KO cells either untransfected or retrovirally transfected with empty vector or cDNA encoding for human NRBF2 were analyzed for NRBF2 expression by immunoblotting. Cleared cellular lysates were prepared and analyzed for actin and NRBF2. (D) Same experimental setup like for (A) was performed for MEF wild-type (WT) or *nrbf2* KO cells either untransfected or retrovirally transfected with empty vector or cDNA encoding for human NRBF2. Here, only one concentration was used for PPAR activation (20 µM Telmisartan, 20 µM GW501516, 1 µM GW7647 and 100 µM Wy14643). (D) Signal intensities of immunoblots were quantified. Diagrams show fold changes calculated by dividing each normalized ratio (protein to loading control) by the average of the normalized ratios of the control samples (medium conditions). Results are mean ± SEM. Statistical analysis was done by one-way ANOVA (corrected by Tukey's multiple comparisons test), *P < 0.05. n = 3. Only selected significant differences are annotated. A complete list of P values for all calculated significant differences can be found in the addendum.

AML12 cells were incubated for 24 h in medium supplemented with two different concentrations of each PPAR agonists. Following immunoblot analysis for protein expression of ULK1, BECN1 and LC3 (Fig 5.7, A), the quantified and normalized signal intensities displayed a clearly visible upregulation for ULK1 and BECN1 protein level, albeit no significant differences could be obtained for BECN1. LC3-II protein levels were only slightly affected (Fig 5.7, B). To transfer these observations to a NRBF2-specific model system, NRBF2 deficient MEF cells were retrovirally transfected with either empty vector or cDNA encoding for human NRBF2. Expression was confirmed by immunoblotting (Fig 5.7, C). The same experimental setup like before was now applied for the two pairs of cell lines (MEF wild-type and *nrbf2* KO or MEF *nrbf2* KO transfected with NRBF2 or empty vector). Based on titration experiments for each PPAR-agonist in MEF cells (data not shown), one concentration was chosen for each pharmacological PPAR activator: 20 µM for Telmisartan (PPAR gamma), 20 µM for GW501516 (PPAR beta/delta) and 1 µM and 100 µM for GW7647 and Wy14643, respectively, (PPAR alpha). Differences for LC3-II and ULK1 protein expression were observed after immunoblot analysis (Fig 5.7, D). Quantification and normalization of signal intensities confirmed these observations and further revealed a NRBF2-dependent difference in protein expression. Alterations of ULK1 protein levels

were detected for both cell line pairs. In both cases, cells expressing NRBF2 displayed a stronger upregulation of protein expression after PPAR stimulation compared to cells deficient for NRBF2, where also a slight downregulation of protein expression compared to medium conditions was detectable. This opposed regulation pattern was also identified with regard to LC3-II by comparison of reconstituted and vector transfected cells. However, significant differences could only be calculated sporadically. For BECN1, varying protein levels, but no general NRBF2-dependent regulation pattern was detected (Fig 5.7, E).

Since stimulating effects of PPAR activation on protein expression of various ATGs were confirmed and more importantly, a specific NRBF2-dependent effect underlying these processes was indicated, the effect of NRBF2 on global gene regulation was investigated. Therefore, a microarray approach using *nrbf2* KO MEFs transfected with either empty vector or cDNA encoding for wild-type NRBF2 in combination with full medium and starvation treatment for 4 h was performed. Total mRNA was isolated and samples were analyzed by Affymetrix microarray (Genomics & Transcriptomics Laboratory, BMFZ, Heinrich Heine University Düsseldorf). Obtained results are shown in figure 5.8.

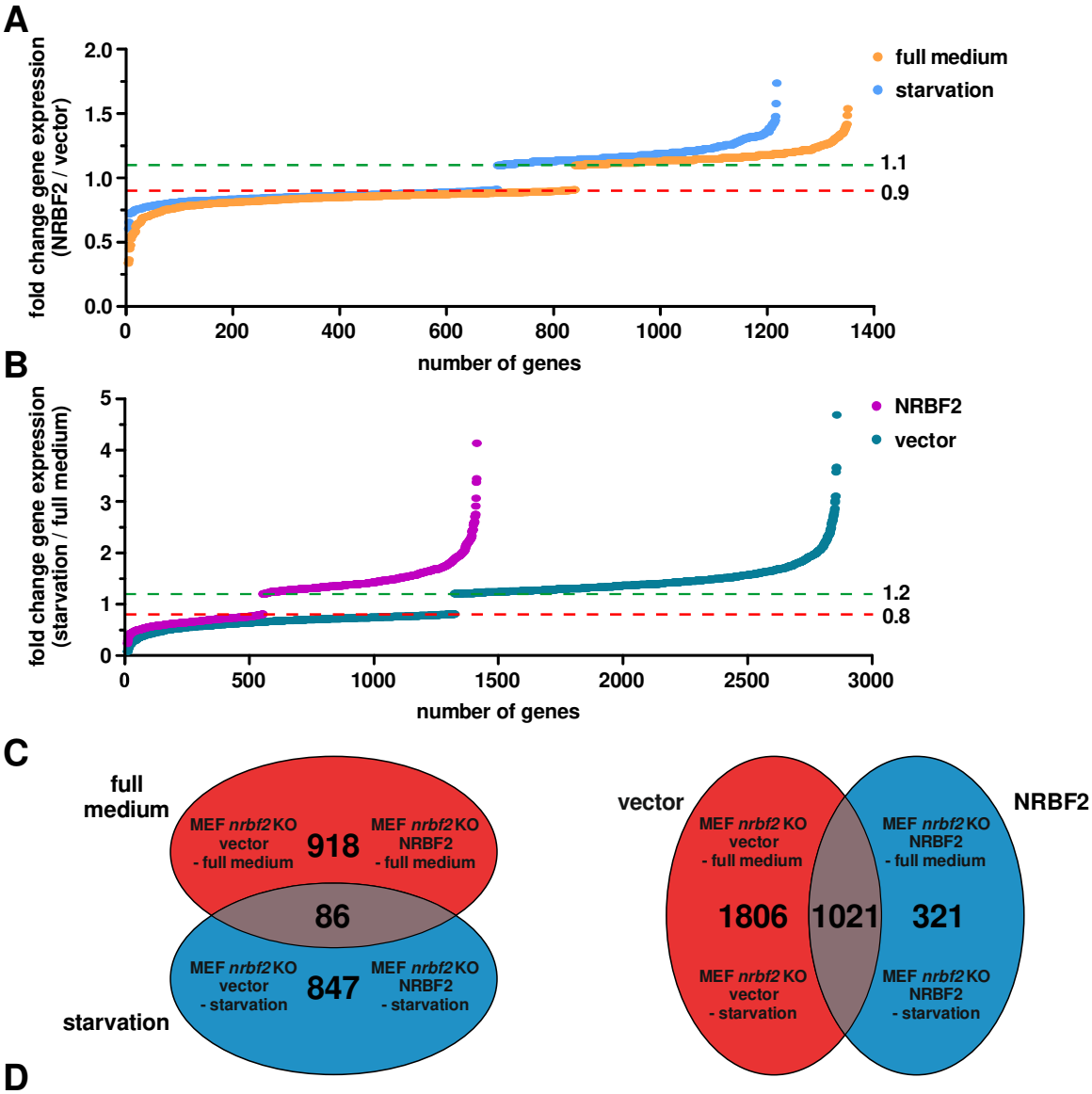

D

		full medium		starvation	
protein name	gene symbol	fold change	t-test significance	fold change	t-test significance
Signal transducer and activator of transcription 2	*Stat2*	0.74	*** (1.18E-04)		
Interferon regulatory factor 7	*Irf7*	0.65	*** (1.24E-04)		
Peroxisomal targeting signal 2 receptor (Peroxin-7)	*Pex7*	1.21	* (3.89E-02)	1.31	** (5.77E-03)
Interleukin 6	*Il6*			1.41	** (7.95E-03)

		vector		NRBF2	
protein name	gene symbol	fold change	t-test significance	fold change	t-test significance
Autophagy-related protein 13	*Atg13*	1.69	** (1.47E-03)		
Retinoic X receptor alpha	*Rxra*	1.72	*** (9.96E-04)		
Retinoic acid receptor gamma	*Rarg*	1.23	** (3.45E-03)		
Transcription factor AP-1	*Jun*	0.61	*** (3.45E-04)		
Nuclear factor NF-kappa-B p105 subunit	*Nfkb1*	0.68	*** (9.75E-04)		
Unc-51 like autophagy activating kinase 1	*Ulk1*	1.56	*** (3.02E-05)	1.52	** (1.43E-03)
Phosphatidylinositol 3-kinase catalytic subunit type 3	*Pik3c3*	1.60	*** (4.62E-04)	1.43	*** (3.29E-04)
Beclin 1-associated autophagy-related key regulator	*Atg14*	2.63	*** (4.97E-06)	2.23	*** (2.74E-05)
UV radiation resistance associated gene	*Uvrag*	1.44	*** (4.81E-05)	1.38	*** (6.06E-04)
Microtubule-associated protein 1 light chain 3B	*Map1lc3b*	1.74	*** (1.24E-05)	1.67	*** (4.16E-05)
BCL-2 interacting protein 3	*Bnip3*	2.98	*** (3.96E-07)	2.44	*** (4.43E-07)
WD repeat domain phosphoinositide-interacting protein 4	*Wdr45*	1.67	*** (1.13E-04)	1.37	*** (9.84E-05)
Tuberous sclerosis 1 (Hamartin)	*Tsc1*	1.41	*** (3.81E-06)	1.66	*** (7.17E-04)
Interleukin 6	*Il6*	0.35	*** (5.82E-05)	0.53	** (1.21E-03)
Forkhead box protein O3	*Foxo3*	1.45	** (3.70E-03)	1.31	** (2.00E-03)
PTEN-induced putative kinase 1	*Pink1*			1.48	** (1.09E-03)
Cathepsin F	*Ctsf*			1.51	*** (1.48E-04)

Figure 5.8: Influence of NRBF2 on global gene expression. Number of identified regulated genes by comparison of (A) NRBF2 expressing and NRBF2 deficient MEF cells under full medium or starvation conditions or (B) starvation and full medium treatment for NRBF2-expressing or NRBF2-deficient cells. Genes display minimal regulation of 10% (A) or 20% (B), respectively. The number of identified genes accounts for identification numbers assigned by the manufacturer of the microarray chip (Affymetrix). Not all of these identifiers have corresponding GenBank® identification numbers, which explains variations between the total numbers of identified genes by microarray (A and B) and the regulated genes depicted by Venn diagrams (C), where solely GenBank® identifiers were employed. (C) Venn diagrams displaying number of regulated genes which were significantly differentially expressed in the scenarios described under A and B. (D) Experiments were performed in triplicates and based on low p-values in combination with high fold change ratios between the scenarios described under (A) and (B), hierarchic lists of identified regulated genes were created considering all identified regulated genes.

The performed microarray analysis comprised detailed information about differential gene regulation for the comparison of the following scenarios: 1) genes differentially regulated between NRBF2 expressing and NRBF2 deficient cells (evaluated for full medium and starvation treatment), and 2) genes differentially regulated between full medium and starvation treatment (evaluated for NRBF2 expressing and NRBF2 deficient cells). For the first scenario, over 1200 genes were identified to be differentially regulated (Fig 5.8, A). In Venn diagrams, a total number of 1851 differentially regulated genes was identified, 918 of them exclusively for full medium treatment, 847 exclusively for administration of starvation and 86 genes as an overlap of both conditions. Maximal amplitudes of the detected regulations were up to factor two, but the majority of the identified genes was up- or downregulated only by ca. 30%. With regard to the second scenario, an elevated number of 2700 differentially regulated genes was detected for vector transfected cells. Here, the maximal amplitudes were increased to factor five. Again, illustration as Venn diagrams displayed the specific distribution of identified gens. Here, a total number of 3148 differentially regulated genes was identified, 1806 exclusively for vector transfected cells, 321 exclusively for cells reconstituted with NRBF2 and 1021 genes as overlap of both cell lines.

Based on low p-values in combination with high fold change values the most prominent candidates were chosen and arranged in hierarchic lists (Fig 5.8, D). For the first scenario (NRBF2 expressing versus deficient cells), only few genes matched these criteria, namely

Stat2, *Irf7*, *Pex7* and *Il6*. For the second scenario (full medium versus starvation conditions), more genes could be selected, among these many directly related to autophagy (*Atg13*, *Ulk1*, *Map1lc3b*, *Pik3c3*, *Atg14*, *Uvrag*, *Bnip3*, *Wdr45*, *Tsc1* and *Pink1*), to transcriptional processes (*Rxra*, *Rarg*, *Jun*, *Nfkb1* or *Foxo3*) and other genes (*Il6* and *Ctsf*).

For further validation of the results obtained by microarray and for a comprehensive analysis of influences by PPAR stimulation, qRT-PCR experiments were performed [181]. The examined genes were chosen on basis of the performed microarray. *Becn1* was included in order to allow for comparison to the previously performed experiments regarding regulation of protein level, *Ppara* was included as NRBF2-interaction partner and putative mediator of gene responses, and *Acox1* and *Sesn2* were included as further positive controls for PPAR alpha regulated gene expression [129].

Due to the high number of genes to be investigated, qRT-PCR primer pairs were designed individually and detection of amplified PCR products was achieved by BRYT Green® chemistry. Since the quantification accuracy of qRT-PCR experiments crucially depends on the exact exponential doubling of the amplified PCR-products [182], the individually designed primer pairs had to be tested for proper applicability in advance to the actual gene expression measurements. This is exemplarily shown for *Atg13* in figure 5.9.

A

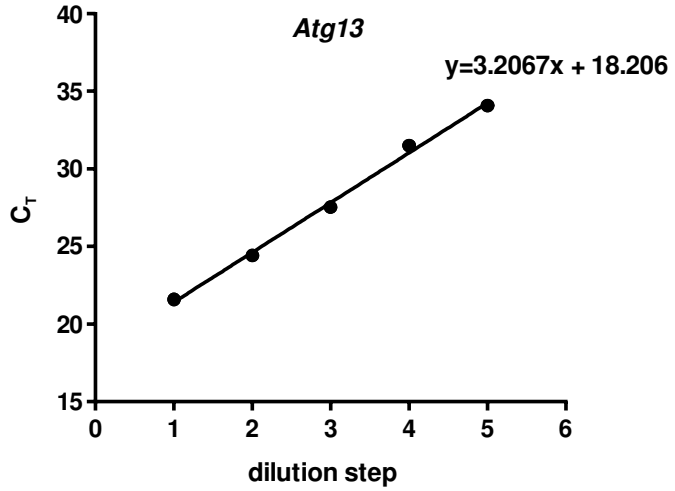

B

gene	amplification efficiency (E)
Hprt1	1.961
Ulk1	1.911
Atg13	2.050
Becn1	1.965
Pik3c3	2.071
Atg14	2.133
Uvrag	2.016
Map1lc3b	1,940
Pink1	2.007
Bnip3	2.053
Tsc1	1.901
Wdr45	2.058
Ppara	-
Rxra	2.009
Rarg	2.080
Stat2	1.941
Foxo3	2.107
Jun	2.025
Nfkb1	2.069
Irf7	1.923
Pex7	1.993
Il6	1.894
Acox1	2.135
Sesn2	1.989
Ctsf	2.127

Figure 5.9: Evaluation of primer efficiency for qRT-PCR. (A) Measurement of C_T values for Atg13 primer pair and serial dilution of template cDNA was performed and linear regression was calculated. (B) Amplification efficiencies for all designed primers were calculated based on the ascent of compensation lines after serial dilution.

The evaluation of primer efficiency was performed by qRT-PCR using serial dilutions of template cDNA by factor 10. After measurement, the calculated threshold (C_T) values for each dilution step were plotted against the dilution factor and linear regression was computed. Based on the ascent of compensation lines the amplification efficiencies (E) were calculated for each primer pair. Depending on the relative abundancy of some genes, no C_T values could be obtained for the maximal dilution steps. Anyhow, calculation of amplification efficiencies was not hampered. Solely for *Ppara* no primer efficiency could be calculated and therefore an optimal efficiency of 2 was assumed. Thus, all individually designed primers could be used for further gene expression studies by qRT-PCR.

In a first qRT-PCR experiment the relative gene expression of all chosen genes was tested for cells expressing and lacking NRBF2. In a next step, influence of starvation conditions was assessed in both cell lines (Fig 5.10). Fold change values of gene expression were calculated according to Pfaffl's method [182].

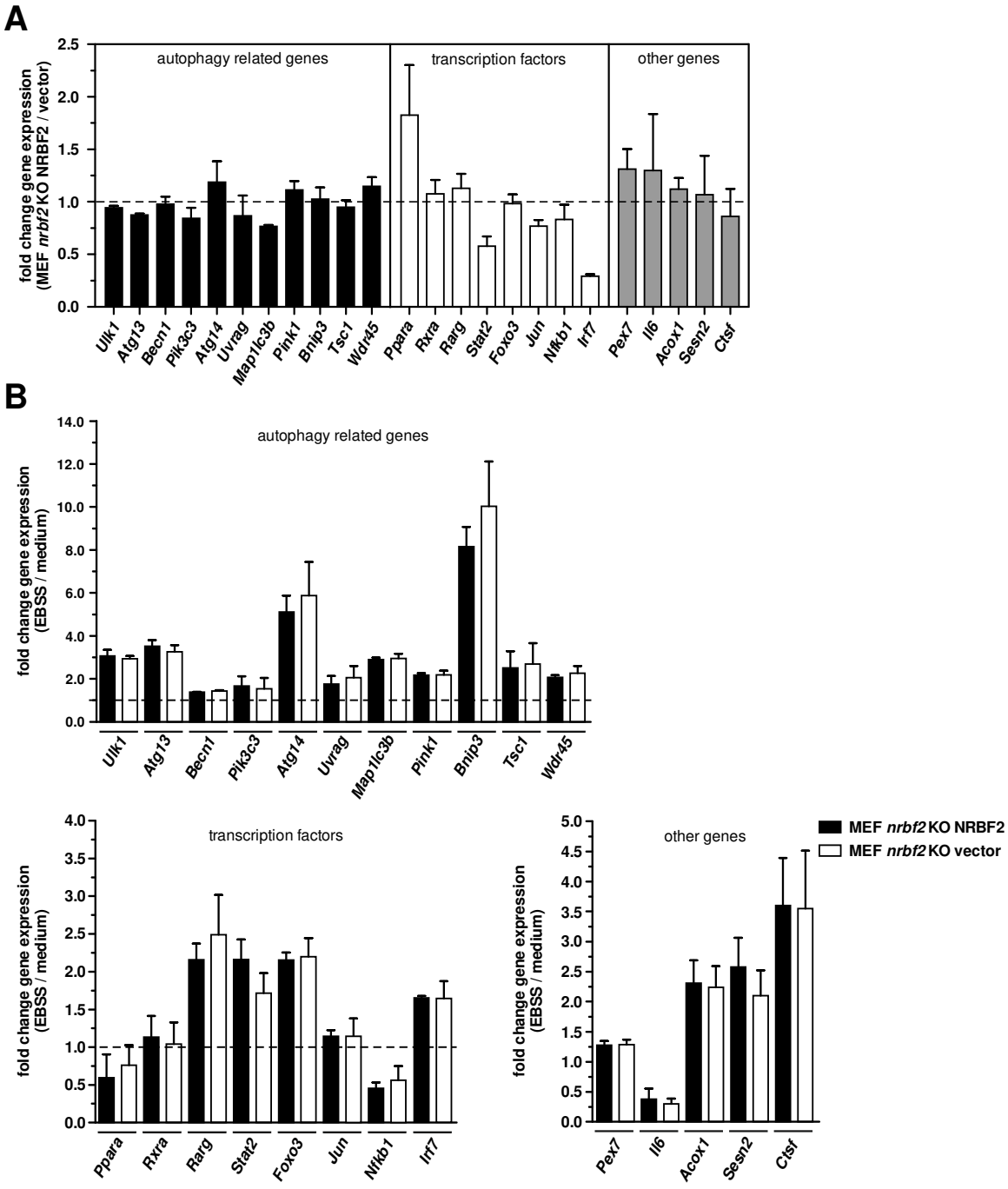

Figure 5.10: Expression profiling of selected genes by qRT-PCR. (A) *nrbf2* KO MEFs retrovirally transfected with empty vector or cDNA encoding for human NRBF2 were incubated in full medium (DMEM). Total mRNA was isolated, reverse transcribed into cDNA and used for qRT-PCR. Diagram displays fold change of gene expression by comparison of NRBF2-expressing and NRBF2-deficient

cells. (B) Same experimental setup was performed, only cells were additionally incubated for 4 h in starvation medium (EBSS). Diagrams display fold change of gene expression by comparison of starvation and full medium treatment. For both experiments, genes were arranged according to their cellular functions. Results are mean ± SEM. Statistical analysis was done by Student *t* test (2-tailed, 2-sample assuming unequal variances), no significant differences were obtained. n = 3.

Most of the investigated autophagy related genes were only slightly affected by NRBF2 deficiency. For *Ulk1*, *Atg13*, *Pik3c3*, *Uvrag* and *Map1lc3b* lack of NRBF2 caused an upregulation displaying the strongest effect for *Map1lc3b*, whereas *Atg14*, *Pink1* and *Wdr45* were slightly downregulated. For the investigated transcription factors, lack of NRBF2-expression caused a strong downregulation of *Ppara*, whereas *Rxra* and *Rarg* displayed only a mild decrease. In contrast, an upregulation was observed for *Stat2* and *Irf7* and to a lower extent also for *Jun* and *Nfkb1*. For the other investigated genes, only *Ctsf* was slightly upregulated by lack of NRBF2-expression, whereas all other genes (*Pex7*, *Il6*, *Acox1* and *Sesn2*) displayed a mild decrease in gene expression (Fig 5.10, A). The expansion of this experimental setup to further incorporate effects caused by administration of starvation is displayed in figure 5.10 B. Here, all examined genes, except for *Rxra,* were somehow regulated by amino acid starvation, but in any case no significant differences could be calculated for the comparison of NRBF2-expressing and NRBF2-deficient cells. Autophagy related genes displayed a general upregulation to varying degrees. Most of the transcription factors and other genes were also upregulated by starvation, except for *Rxra*, which was not affected. *Ppara* and to a stronger extent *Nfkb1* and *Il6* displayed a clear downregulation. The genes used as positive controls (*Acox1*, *Sesn2* and *Ctsf*) were also upregulated by starvation.

By comparison of results obtained by qRT-PCR experiments and the ones obtained by microarray, similar regulation tendencies were found for the effect of either NRBF2-deficieny or administration of starvation, whereas the absolute values differed slightly. Thus, an effect on gene expression by starvation was shown and confirmed previous observations. Further investigation of PPAR-stimulated gene expression with regard to influencing effects of NRBF2 were performed in MEF cells expressing or lacking NRBF2 similar to previous experiments.

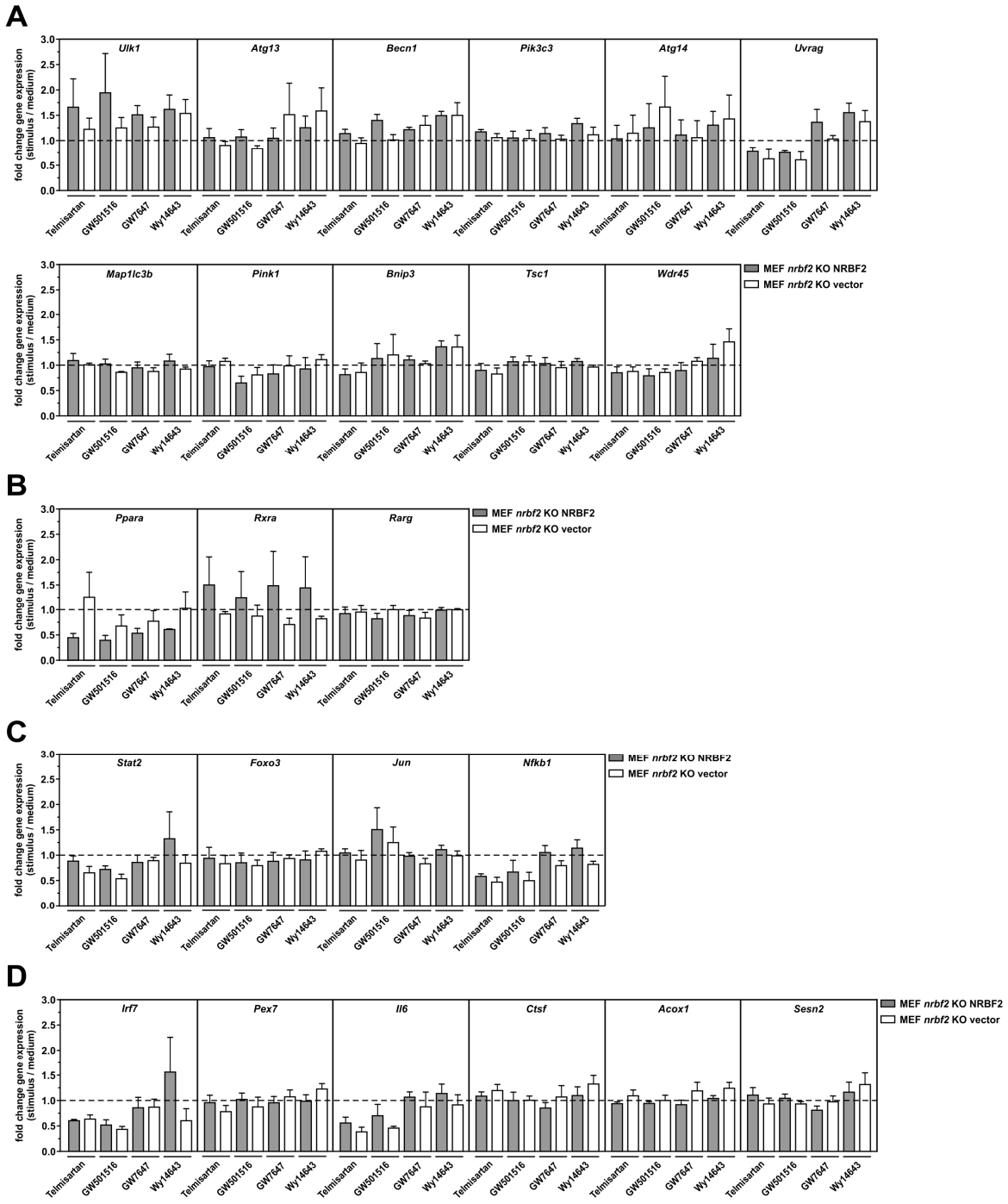

Figure 5.11: PPAR-stimulated gene expression with regard to NRBF2 deficiency. *nrbf2* KO MEFs retrovirally transfected with empty vector or cDNA encoding for human NRBF2 were incubated for 24 h in medium supplemented with pharmacological activators of PPAR gamma (Telmisartan, 20 µM), PPAR beta/delta (GW501516, 20 µM) or PPAR alpha (GW7647, 1 µM and Wy14643, 100 µM). Total mRNA was isolated, reverse transcribed into cDNA and used for qRT-PCR. Diagrams display fold change of gene expression by comparison of PPAR-stimulation to medium conditions. Genes were arranged according to their cellular functions as autophagy related (A), nuclear receptors (B), general transcription factors (C) and other genes (D). Results are mean ± SEM. Statistical analysis was done by Student *t* test (2-tailed, 2-sample assuming unequal variances), no significant differences were obtained. n = 3.

In most cases, changes in gene expression were detected, yet a general regulation pattern was not obvious. Overall, the amplitude of observed effects was considerably lower compared to gene expression stimulated by starvation. In addition, variations between single measurements hampered the calculation of significant differences. No regulation was detectable for *Pik3c3*, *Map1lc3b*, *Tsc1*, *Rarg*, *Foxo3*, *Pex7* and *Ctsf*. In contrast, several genes were affected by stimulation of any PPAR family member, namely *Ulk1*, *Atg13*, *Becn1*, *Uvrag*, *Ppara*, *Rxra*, *Nfkb1* and *Irf7*. Here, effects caused by activation of PPAR alpha by Wy14643 were most prominent. *Bnip3*, *Wdr45* and to a lower extent *Acox1* and *Sesn2* were regulated solely following activation of PPAR alpha, whereas *Stat2* and *Il6* were influenced by activation of either PPAR beta/delta or gamma. *Pink1* was moderately regulated by stimulation of PPAR beta/delta, whereas no gene was regulated solely following activation of PPAR gamma. Only for *Ppara* and *Rxra* a general and furthermore opposed regulation pattern was detectable. Here, *Ppara* was downregulated in cells expressing NRBF2 following any treatment, which was attenuated for cells lacking NRBF2. In contrast, *Rxra* was upregulated in NRBF2-expressing cells and slightly downregulated by NRBF2 deficiency.

In summary, several effects of PPAR-activation on gene expression were observed, frequently affected by NRBF2-deficency. However, a general regulation pattern was not obvious.

5.3 ULK1 regulates the class III PtdIns3K complex via the phosphorylation of NRBF2

5.3.1 Identification of a ULK1-dependent phosphorylation of NRBF2

As described above and shown by other groups, NRBF2 is a member of the class III PtdIns3K complex and acts as a modulator of autophagy. However, its exact function is still controversially discussed [53–55]. Regulation of a protein's function, which is a necessary requirement for the adaptation to rapidly changing conditions, is a vital cellular regulation mechanism and in many cases achieved by post-translational modification (PTM) of proteins [183]. Lately, NRBF2 research focused on the aspect whether and to what extent the activity of NRBF2 is controlled by phosphorylation, which accounts for the most common type of PTM experimentally observed [184]. Evidence for an mTORC1-mediated phosphorylation of NRBF2 as a modulation of the autophagic machinery was recently presented by Ma and colleagues [185].

ULK1 is the main autophagy-initiating kinase with a constantly growing list of substrates identified as downstream components of the autophagy signaling network [186]. Among these, the class III PtdIns3K complex components PIK3C3, BECN1, ATG14 and AMBRA1 are phosphorylated and thereby activated for their specific roles in autophagosome biogenesis [36–39]. The last part of this thesis focused on the existence and the possible influence of NRBF2-phosphorylation executed by the autophagy-initiating kinase ULK1.

To test the hypothesis that ULK1 also phosphorylates NRBF2 and thereby further regulates the activity of the class III PtdIns3K complex, *in vitro* kinase assays using recombinant NRBF2 as substrate were performed (Fig 5.12).

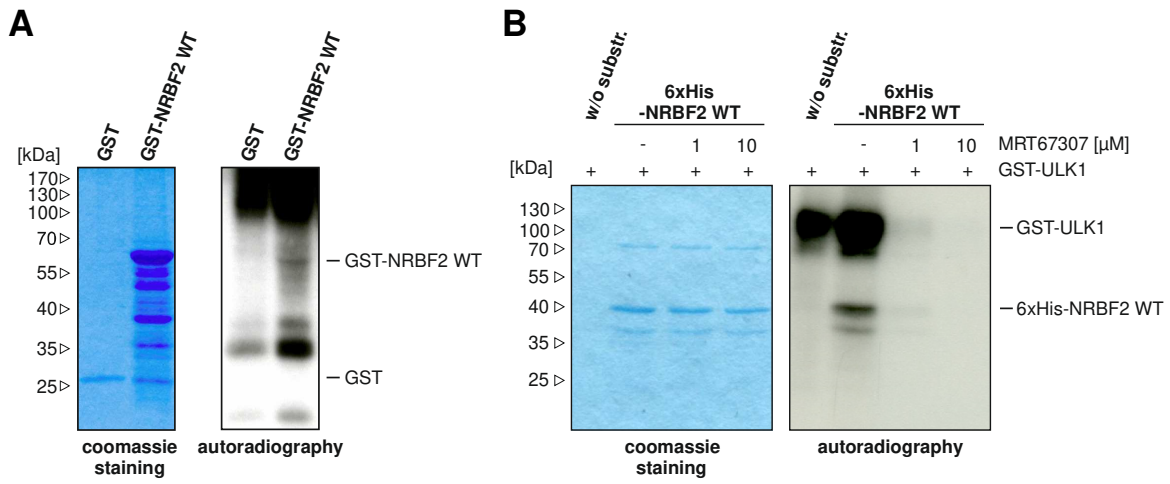

Figure 5.12: ULK1 phosphorylates NRBF2 *in vitro*. (A) *In vitro* kinase assays using GST-only or GST-NRBF2 WT as substrates and crude cellular lysates from HEK293 cells as kinase were performed. Coomassie staining of the gel (left panel) and autoradiography (48 h exposure; right panel) are shown. (B) *In vitro* kinase assays were performed using 6xHis-NRBF2 WT as substrate and recombinant GST-ULK1 as kinase. The ULK1 inhibitor MRT67307 was added at the indicated concentrations. Coomassie staining of the gel (left panel) and autoradiography (6 h exposure; right panel) are shown.

The initial testing of a general cellular NRBF2 phosphorylation was done by utilization of crude cellular lysates of HEK293 cells as "phosphorylating agent" and GST-NRBF2 or GST-only as substrates in an *in vitro* kinase assay. Purity of the used GST-NRBF2 was very low, as many additional bands were detected after coomassie staining. Nevertheless, a weak phosphorylation signal for NRBF2 was observed (Fig 5.12, A). In a next step, only recombinant GST-ULK1 as kinase and 6xHis-tagged NRBF2 were used for *in vitro* kinase assay. Again, a phosphorylation of NRBF2 was detected, this time by a clearly visible signal after autoradiography. Furthermore, NRBF2 phosphorylation was nearly completely inhibited by application of the ULK1 inhibitor MRT67307 [187] (Fig 5.12, B).

To gain more information about this detected ULK1-dependent phosphorylation of NRBF2, a mass spectrometric phosphorylation analysis was performed (Institute of Cardiovascular Physiology, Medical Faculty, Heinrich Heine University Düsseldorf) and the obtained results were validated again by *in vitro* kinase assay (Fig 5.13).

A

proteins	position within protein	localization probability	posterior error probability	score	number of phospho (STY)	amino acid	phospho (STY) probabilities
Q96F24	15	1.000	4.38E-04	73.72	1	S	GILEVMEGPLNLAHQQS(1)R
Q96F24	50	0.999	2.41E-06	115.09	1	S	LT(0.001)QS(0.999)EQAHLSLELQR
Q96F24	56	1.000	1.77E-06	127.07	1	S	LTQSEQAHLS(1)LELQR
Q96F24	101	0.889	8.08E-04	63.93	1	S	AQQNT(0.004)DKDAAAHLQT(0.097)S(0.889)HKPS(0.006)AEDAEGQS(0.002)PLS(0.002)QK
Q96F24	277	1.000	6.31E-30	158.65	1	S	DIPIPNLPPLDFPSPELPLMELS(1)EDILK

B

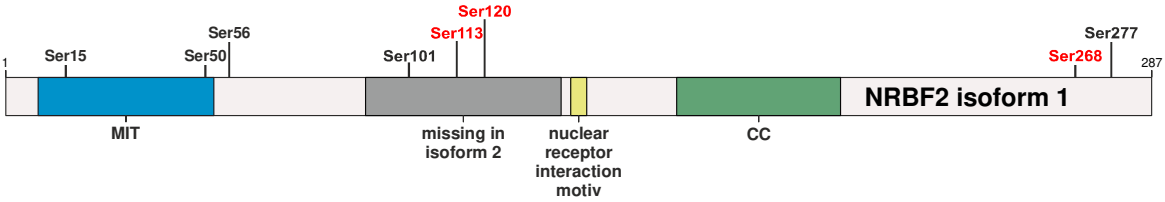

C

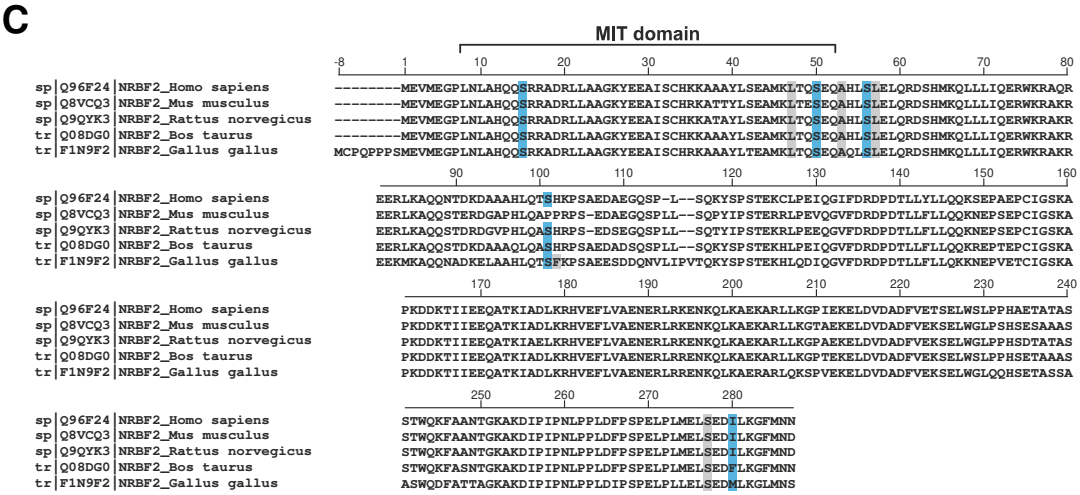

D

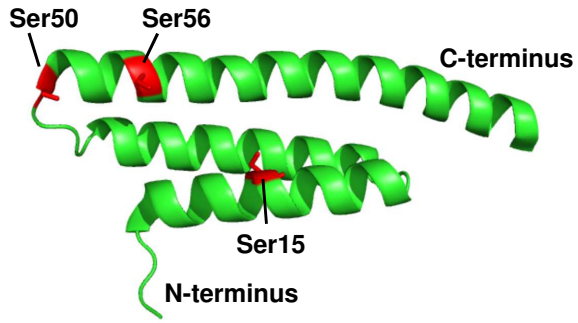

E

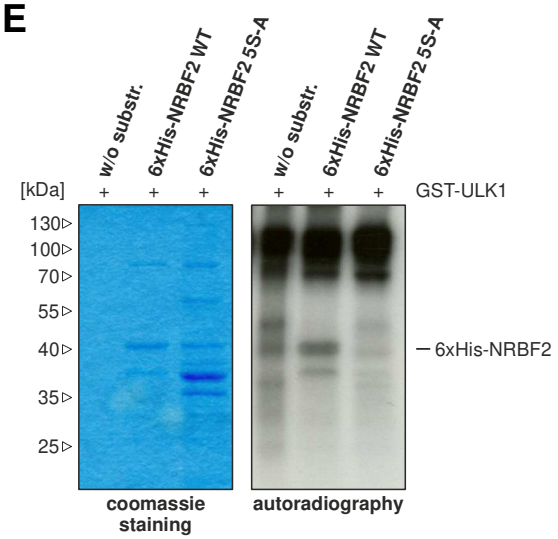

Figure 5.13: Identification and validation of candidate phospho-acceptor sites in NRBF2. (A) *In vitro* kinase assays were subjected to mass spectrometry. Identified phosphor-acceptor sites and scores are listed. (B) Schematic representation of NRBF2. Structural domains and identified phosphosites are annotated (phospho-acceptor sites identified within this work are annotated in black, previously identified phospho-acceptor sites in red). (**C**) Alignment of NRBF2 protein sequences from various eukaryotic species (amino acid numbering of human NRBF2). Identified phosphor-acceptor sites are conserved between species and are highlighted by blue background;

amino acids fitting to the ULK1 consensus sequence requirements are highlighted in grey. NRBF2 MIT domain (amino acids 8 to 52) is annotated. (**D**) Crystal structure model of NRBF2 MIT domain (PDB entry 4ZEY). Ser15, Ser50 and Ser56 are highlighted in red. (**E**) *In vitro* kinase assays using 6xHis-NRBF2 WT or 6xHis-NRBF2 5S-A as substrates and recombinant GST-ULK1 as kinase were performed. Coomassie staining of the gel (left panel) and autoradiography (13 h exposure; right panel) are shown (5S-A: serine to alanine quintuple mutant).

Five serine residues within NRBF2 harboring a phospho-group following *in vitro* phosphorylation were identified by mass spectrometry: Ser15, Ser50, Ser56, Ser101, and Ser277 (amino acids numbered according to human NRBF2, Fig 5.13, A). A schematic representation of NRBF2 domain organization including all five identified phospho-acceptor sites is depicted in figure 5.13, B. Additional phospho-acceptor sites have previously been identified [185,188–190] (Fig 5.13, B). All identified phospho-acceptor sites, except for Ser101 in mouse, are conserved between different eukaryotic species. Regarding a reported ULK1 consensus motif (i.e. bulky and hydrophobic amino acids at the -3, +1 and +2 position) [37], three of the identified sites (Ser50, Ser55, Ser277) fulfill these requirements partially. Of note, chicken NRBF2 protein sequence harbors additional eight and three amino acids at the N-terminus and within the protein sequence, respectively (Fig 5.13, C). Two of the identified sites, Ser50 and Ser56, are located at an accessible position between two helical elements at the C-terminal end of the α-helical microtubule interacting and trafficking molecule (MIT) domain. These locations were annotated in a crystal structure model of NRBF2 MIT domain (PDB entry 4ZEY, Fig 5.13, D). A mutated version of NRBF2 where all serine residues were exchanged for alanine (5S-A: serine to alanine quintuple mutant) was generated and the identified phosphorylated residues were confirmed in *in vitro* kinase assays. ULK1-dependent phosphorylation of NRBF2 5S-A was largely abolished (Fig 5.13, E).

Results obtained by *in vitro* methods can be affected by a set of factors that differ from physiological situations, like presence or absence of certain reaction components. This is why data from *in vitro* experiments can be used as evidence for certain theories, but a validation by independent and most favorably by *in vivo* methods is generally aimed for. An *in vivo* detection of posttranslational protein modifications, especially of

phosphorylation events, is a challenging task. In most cases, phospho-specific antibodies are used for these purposes, but their generation is tedious and therefore they are available only for a limited number of proteins [191]. In order to validate the results obtained by *in vitro* kinase assay, the ULK1-dependent phosphorylation of NRBF2 in intact cells was monitored by an adapted version of the proximity ligation assay (PLA). This method enables the detection of protein-protein interactions or, in this case, of protein modifications by antibody-recognition combined with an exponential signal amplification by PCR using fluorescently labelled nucleotides [192]. Here, anti-NRBF2 and anti-phospho-serine antibodies were used and the results are shown in figure 5.14.

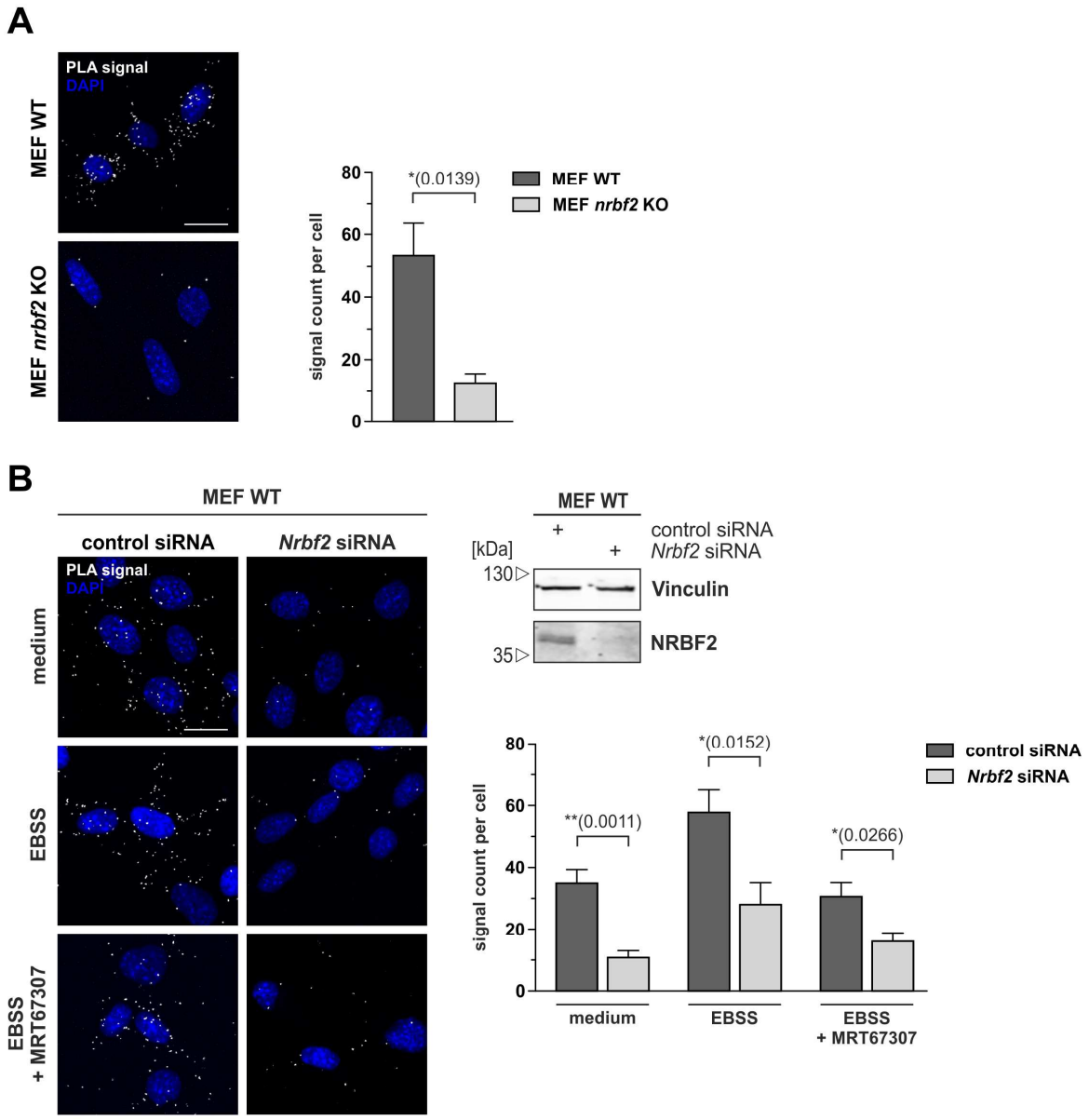

Figure 5.14: Evidence for ULK1-mediated phosphorylation of NRBF2 in intact cells. (**A**) Wild-type or *nrbf2* KO MEFs were seeded onto glass cover slips. Next day cells were used for proximity ligation

assay with anti-NRBF2 and anti-phospho-serine antibodies. Nuclei were stained with DAPI (left panel). Signals and nuclei per image were counted and the signal:nuclei ratio was calculated (right panel). Results are mean ± SEM. Statistical analysis was done by Student *t* test (2-tailed, 2-sample assuming unequal variances), **P* < 0.05. (**B**) Wild-type MEFs were transfected with 50 nM of either non-targeting control siRNA or *Nrbf2* siRNA for 72 h. Successful knockdown of NRBF2 was confirmed by immunoblotting for vinculin and NRBF2 (upper right panel). 24 h after transfection, MEFs were seeded onto glass cover slips. After additional 48 h, cells were incubated for 1 h in full medium (DMEM), starvation medium (EBSS) or in starvation medium containing 10 µM of the ULK1 inhibitor MRT67307. Proximity ligation assay was performed analogously to (A) (left panel). Signals and nuclei per image were counted and the signal:nuclei ratio was calculated (lower right panel). Results are mean ± SEM. Statistical analysis was done by Student *t* test (2-tailed, 2-sample assuming equal variances), **P* < 0.05, ***P* < 0.01. In both experiments, a minimum of five images was analyzed. Scale bar: 20 µm.

To evaluate the general applicability of this method, wild-type and *nrbf2* KO MEF cells cultured under full medium conditions were compared. A significant reduction of PLA signal count was observed in *nrbf2 KO* MEFs (Fig 5.14, A). For further exclusion of factors like genetic variations between the used cell lines, the PLA was repeated using wild-type MEF cells transfected with either non-targeting control siRNA or *Nrbf2* siRNA. An efficient knockdown was confirmed by immunoblotting. Once more, a clear reduction in PLA signal count was observed in cells with decreased NRBF2 expression compared to cells transfected with non-targeting siRNA. This reduction was significant for all treatments. Importantly, the PLA results clearly show an increase in NRBF2 phosphorylation in starved, autophagic cells. Furthermore, since PLA signals were clearly reduced by application of the ULK1 inhibitor MRT67307, at least a partial control of NRBF2 phosphorylation status by ULK1 was reasoned.

5.3.2 NRBF2 phospho-status regulates the composition of the class III PtdIns3K complex I

Previous reports stated that NRBF2 stimulates autophagic capacity by enhancing the lipid kinase activity of the class III PtdIns3K complex I via dimerization of two monomeric forms. The dimerization itself is thought to be mediated by self-oligomerization of NRBF2 [52]. To evaluate if the identified phosphorylation of NRBF2 by ULK1 affects the class III PtdIns3K complex assembly, size exclusion chromatography experiments were performed.

Therefore, *nrbf2 KO* MEFs either transfected with empty vector or cDNA encoding for human HA-tagged wild-type NRBF2, the non-phosphorylatable 5S-A version of NRBF2, or a phospho-mimicking serine to aspartate 5S-D version of NRBF2 were analyzed under full medium conditions. As prerequisite for these experiments, the expression of the above-mentioned NRBF2-versions was examined by immunoblotting. The results depicted in figure 5.15 confirm expression of all NRBF2 variants, although a slightly different migration pattern was observed for the 5S-A mutant.

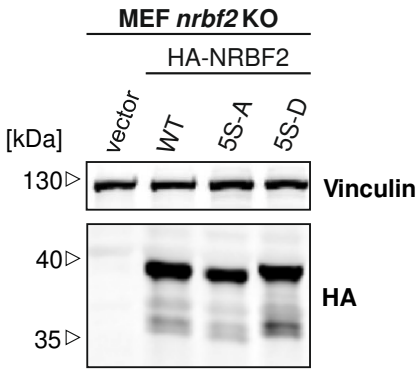

Figure 5.15: Expression of mutant NRBF2 variants. Cleared cellular lysates of *nrbf2 KO* MEFs retrovirally transfected with either empty vector or cDNA encoding for human HA-tagged wild-type NRBF2, NRBF2 5S-A or NRBF2 5S-D were prepared and analyzed by immunoblotting for vinculin or HA.

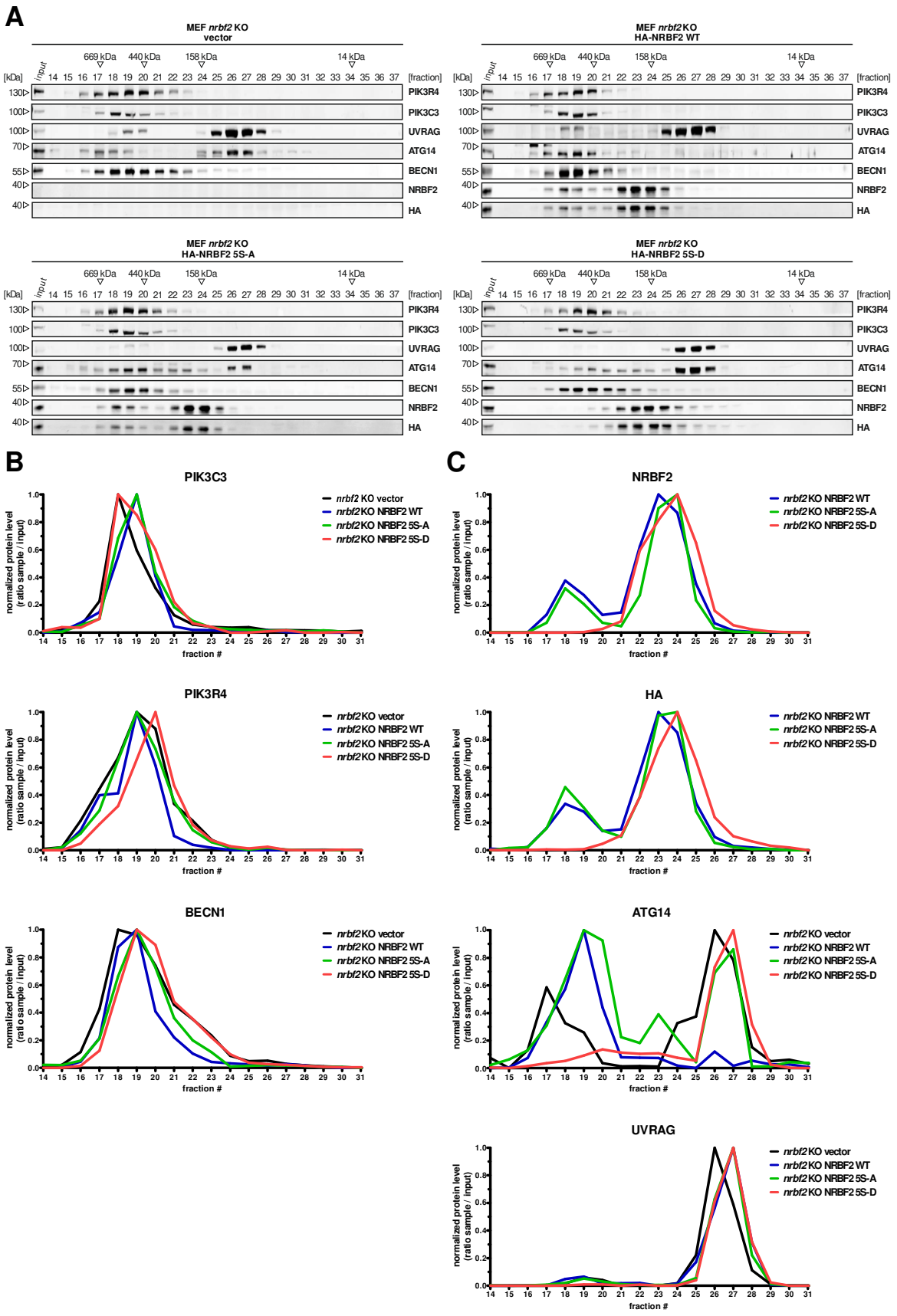

Figure 5.16: NRBF2 affects assembly of class III PtdIns3K complex. (A) S100 extracts of *nrbf2 KO* MEFs transfected with either empty vector or cDNA encoding for human HA-tagged wild-type NRBF2, NRBF2 5S-A or NRBF2 5S-D incubated in full medium (DMEM) were prepared and separated

by size exclusion chromatography on a *Superdex 200 Increase* column. Obtained fractions were analyzed by immunoblotting for the indicated proteins. (B-C) Band intensities of immunoblots were quantified and identical proteins are displayed per diagram. The PtdIns3K core complex components PIK3C3, PIK3R4 and BECN1 are depicted in (B). The additional PtdIns3K complex components NRBF2 (detection by anti-NRBF2 and anti-HA), ATG14 and UVRAG are depicted in (C). Diagrams show protein levels for each fraction. Values are ratios of the input and are normalized to the fraction containing the highest amount of the analyzed protein.

The PtdIns3K core complex components PIK3C3, PIK3R4 and BECN1 can be observed at a molecular mass range corresponding to 400-670 kDa for all tested cell lines, regardless of loss or mutation of NRBF2 (Fig 5.16, B; fractions 16-22). In contrast, the additional class III PtdIns3K complex I or complex II components ATG14 and NRBF2 or UVRAG, respectively, displayed several alterations. Firstly, for wild-type and the 5S-A version of NRBF2 two major "populations" were detected. A smaller one co-eluding with the PtdIns3K core complex at high molecular mass ranges and a more prominent one at molecular masses below 160 kDa. Notably, the NRBF2 5S-D variant eluted exclusively at low molecular masses and was not detected in fractions corresponding to the PtdIns3K core complex. Anti-HA and anti-NRBF2 antibodies were used for the detection of NRBF2 versions, but no differences were detected (Fig 5.16, C, first two panels). Secondly, migration of ATG14 is dependent on the presence or the phosphorylation status of NRBF2. In cells expressing wild-type NRBF2, ATG14 co-eluded exclusively in fractions corresponding to the PtdIns3K core complex. NRBF2-deficency caused a division of the ATG14 population. A smaller part shifted to slightly higher molecular mass ranges, but the major part of ATG14 was detected below 160 kDa. Presence of the two NRBF2-phospho mutants caused different variations of the above-described scenarios. Presence of the NRBF2 5S-A version caused ATG14 to again co-elute with the PtdIns3K core complex below 600 kDa, but a second population was detected below 160 kDa similar to NRBF2 deficient cells. Presence of the NRBF2 5S-D version shifted the ATG14 population nearly exclusively to the low molecular mass ranges, only small amounts of ATG14 were detected around 400 kDa hence at lower molecular mass than the PtdIns3K core complex (Fig 5.16, C, third panel). Thirdly, for cells deficient for NRBF2 or expressing either the wild-type or the 5S-A variant of NRBF2, the PtdIns3K core complex contains only little amounts of UVRAG, whereas the most prominent UVRAG population was detected below 160 kDa. Presence of the NRBF2 5S-D version caused a

complete absence of UVRAG from the PtdIns3K core complex (Fig 5.16, C, fourth panel). With regard to the oligomerization status of the class III PtdIns3K complex, no indication for an involvement of NRFB2 phosphorylation was detected. The monomeric and the dimeric forms are thought to migrate at 440 kDa and 669 kDa, respectively [52]. Here, a continuous transition between these two stages was observed.

For further clarification, size exclusion chromatography experiments using lysates of ULK1/2 double-deficient MEFs were performed (Fig 5.17). In these cells, NRBF2 is present, but no ULK1-dependent phosphorylation can occur.

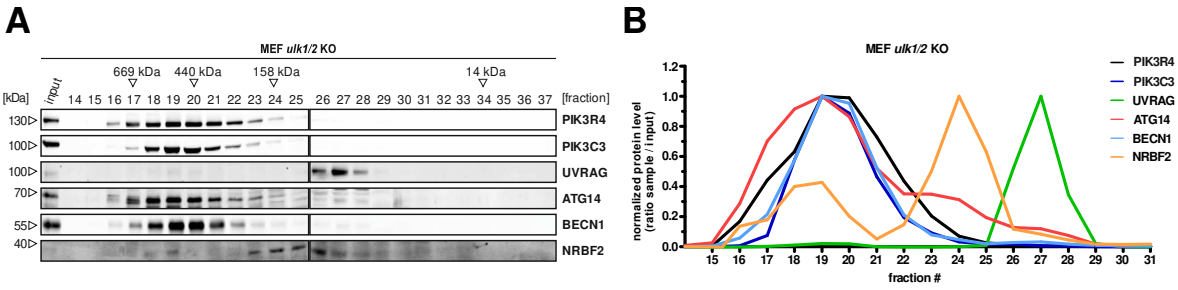

Figure 5.17: Size exclusion chromatography experiments for ULK1/2 deficient cells. (**A**) S100 extract of *ulk1/2* KO MEFs incubated in full medium (DMEM) was prepared and separated by size exclusion chromatography on a *Superdex 200 Increase* column. Obtained fractions were analyzed by immunoblotting for the indicated proteins. (B) Band intensities of immunoblots were quantified, and the diagram shows protein levels for each fraction. Values are ratios of the input and are normalized to the fraction containing the highest amount of the analyzed protein.

For these cells, ATG14 was detectable in a broad molecular mass range from above 600 kDa to lower than 400 kDa and thus again co-eluted with the PtdIns3K core complex, similar to MEF cells expressing wild-type or the 5S-A version of NRBF2 (compare Fig 5.16).

5.3.3 The phosphorylation status of NRBF2 does not affect the overall autophagic flux, but the specific PIK3C3 activity

After modulating effects of NRBF2 phosphorylation for the composition of the class III PtdIns3K complex were observed, additional experiments were performed to analyze how these phosphorylations events affect the autophagic flux in general. It has to be considered that the role of NRBF2 has been controversially discussed in previous reports [53–55]. The

presence of a regulatory NRBF2 phosphorylation might be helpful in connecting these divergent results. Here, the analysis of autophagic flux was done either by analysis of LC3 and p62/SQSTM1 turnover by immunoblotting (Fig 5.18) or by immunofluorescence of LC3 puncta formation (Fig 5.19). In both cases, starvation was used as pro-autophagic stimulus and bafilomycin A_1 was used to block lysosomal degradation processes (compare 1.1.2).

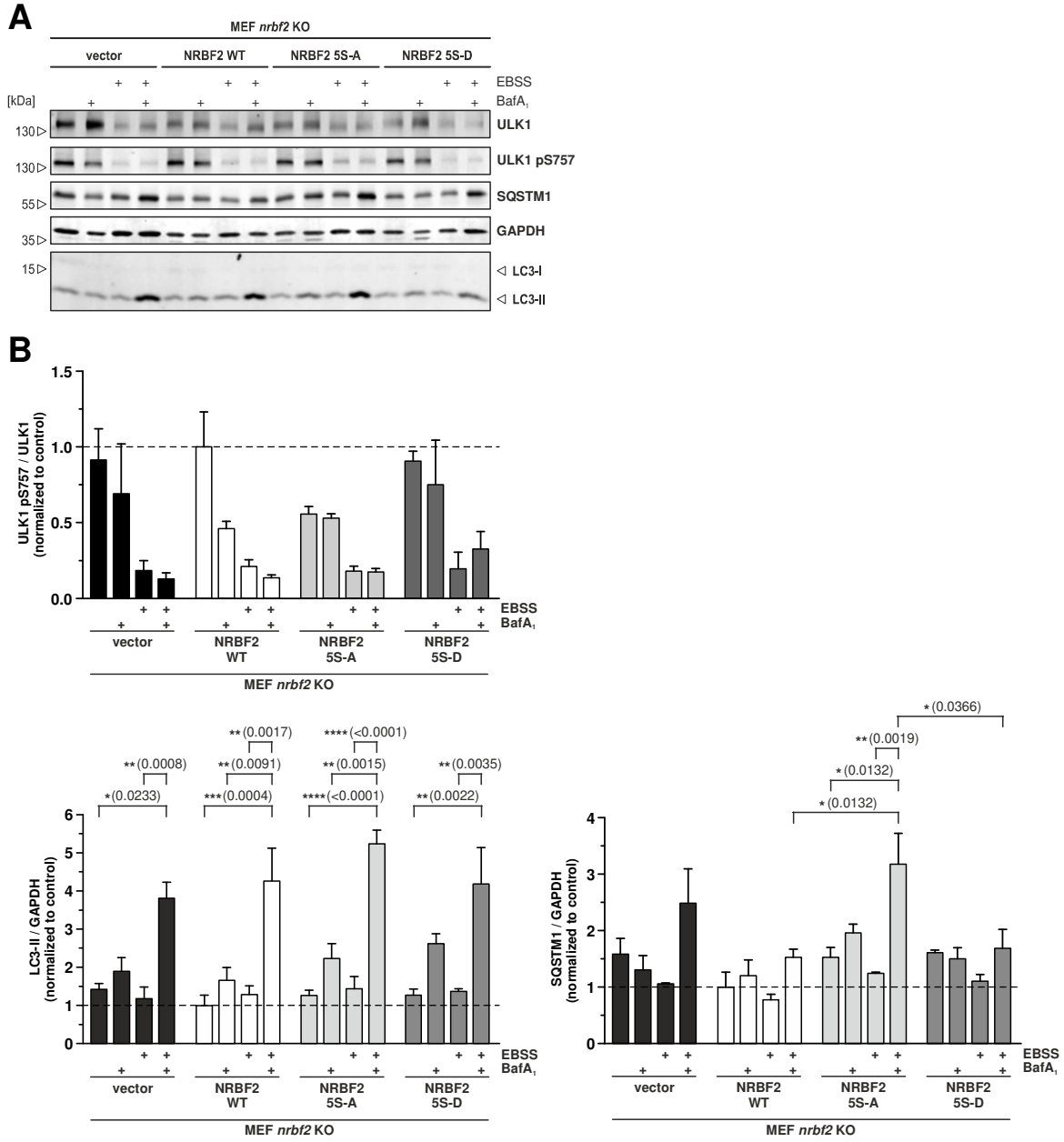

Figure 5.18: Impact of mutated NRBF2 versions on autophagic flux by LC3 and SQSTM1-turnover. (A) *nrbf2 KO* MEFs retrovirally transfected with empty vector or cDNA encoding for the indicated NRBF2 variants were incubated for 2 h in full medium (DMEM) or starvation medium (EBSS) in the presence or absence of 40 nM bafilomycin A_1 ($BafA_1$). Cleared cellular lysates were prepared and analyzed by immunoblotting for ULK1, ULK1 phospho-Ser757, SQSTM1, LC3 and GAPDH. (B) Band intensities of immunoblots were quantified. Diagrams show fold changes calculated by dividing

each normalized ratio (protein to loading control) by the average of the normalized ratios of the control sample (NRBF2 WT treated with medium). Results are mean ± SEM. Statistical analysis was done by one-way ANOVA (corrected by Tukey's multiple comparisons test), *P < 0.05, **P < 0.01, ***P < 0.001, ****P < 0.0001. n = 3. Only selected significant differences are annotated. A complete list of P values for all calculated significant differences can be found in the addendum.

Activation of ULK1 by starvation was confirmed by detection of decreased Ser757 phosphorylation, which represents an inhibitory phosphorylation mediated by mTORC1 [27]. Comparison of LC3-II levels only revealed significant differences for different treatment of the same cell lines and no differences among cell lines. SQSTM1 turnover displayed higher similarities between cells expressing wild-type and 5S-D version of NRBF2 and between NRBF2 5S-A-expressing and NRBF2-deficient cells. Accordingly, sporadic significant differences were found within the NRBF2 5S-A-expressing cells and between them and wild-type and 5S-D-expressing cells (Fig 5.18, B).

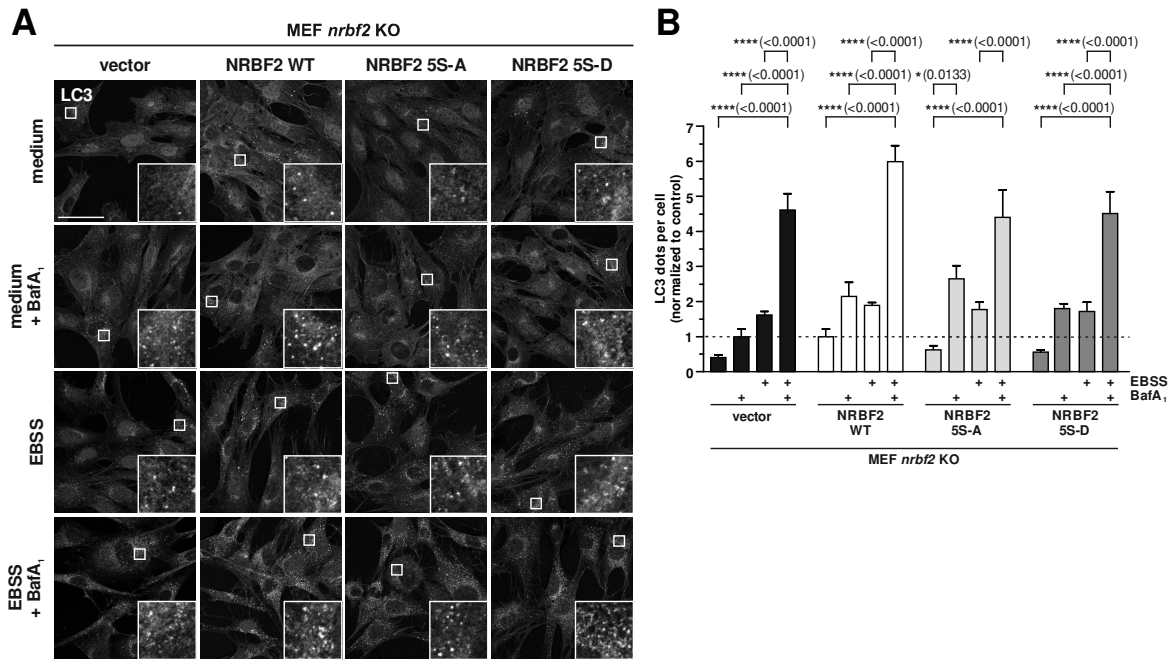

Figure 5.19: Impact of mutated NRBF2 versions on autophagic flux by LC3 immunofluorescence. (A) *nrbf2 KO* MEFs retrovirally transfected with empty vector or cDNA encoding for the indicated NRBF2 variants were grown on glass cover slips overnight and incubated for 2 h in full medium (DMEM) or starvation medium (EBSS) in the presence or absence of 40 nM bafilomycin A_1 ($BafA_1$). Cells were fixed, permeabilized and immunostained for LC3. Imaging was performed using an inverse confocal laser scanning microscope. Scale bar: 50 µm. (B) A minimum of 100 cells per condition was analyzed and quantification was done using Fiji. Diagrams show number of dots per

cell normalized to the control sample (NRBF2 WT treated with medium). Results are mean ± SEM. Statistical analysis was done by one-way ANOVA (corrected by Tukey's multiple comparisons test), *P < 0.05, ****P < 0.0001. n = 3. Only selected significant differences are annotated. A complete list of P values for all calculated significant differences can be found in the addendum.

Analogously to the performed immunoblot experiments, several significant differences could be detected for different treatments within the same cell lines with regard to LC3 puncta formation. Again, no reasonable differences were found between different cell lines and the observed overall autophagic flux for cells expressing NRBF2-mutants was similar to cells expressing wild-type NRBF2 (Fig 5.19, B).

Since the influence exerted by the ULK1-dependent NRBF2-phosphorylation on the class III PtdIns3K complex assembly did not manifest in an altered autophagic activity, the specific PIK3C3 activity was investigated in more detail. Therefore, an *in vitro* PIK3C3 activity assay was utilized in a first approach (Fig 5.20). Additionally, analysis of WIPI2 accumulation *in vivo* was performed (Fig 5.21).

For the *in vitro* PIK3C3 activity assay, the class III PtdIns3K complex I was immunopurified from cells using anti-ATG14 antibodies. After addition of phosphatidylinositol (PtdIns) and ATP, the *in vitro* PtdIns3P production was indirectly assessed by immunoblotting for the PtdIns3P-binding protein GST-p40PX [38]. In a first approach, the experimental setup was tested in wild-type MEF cells and then applied for cells expressing the different NRBF2 versions.

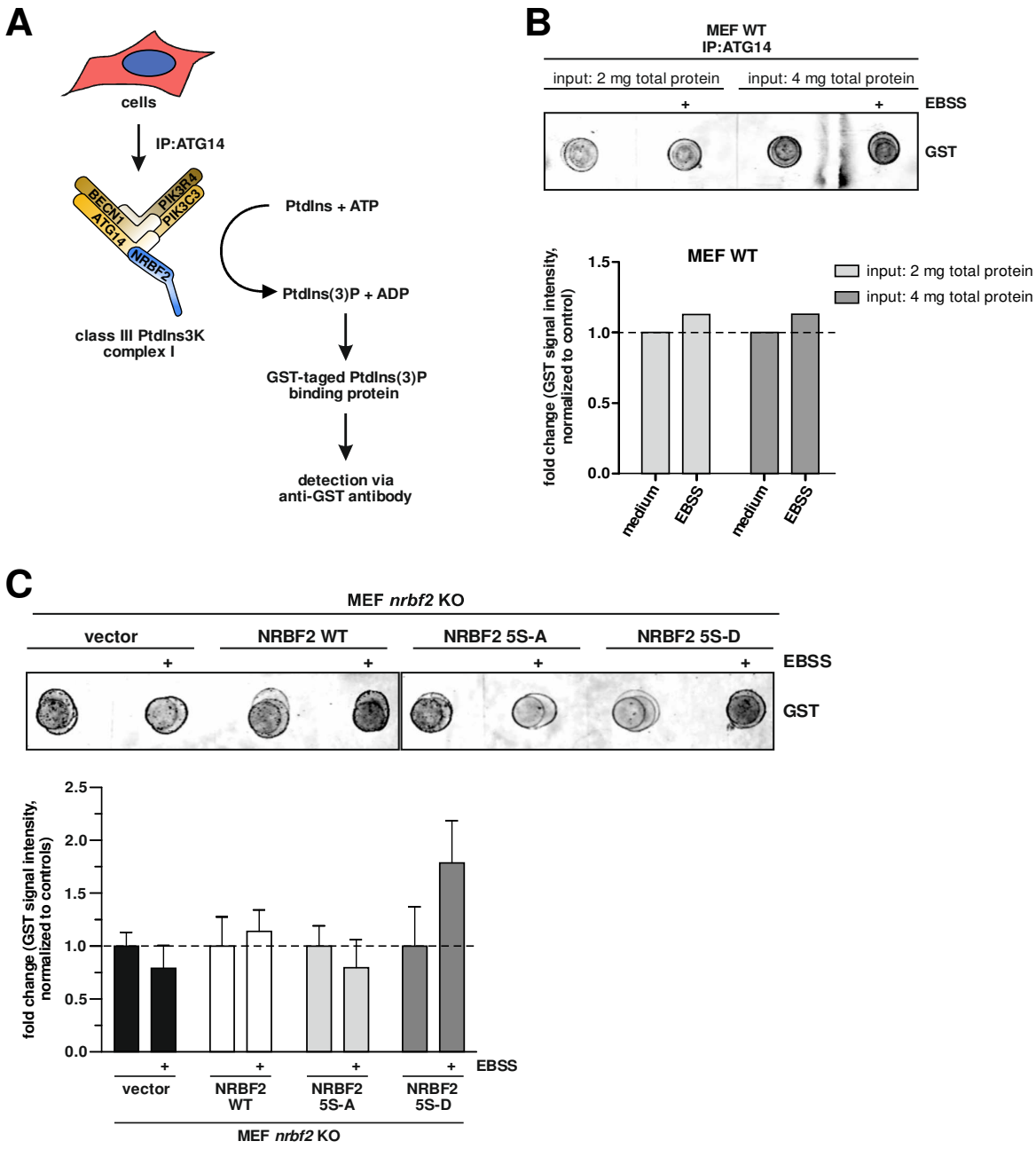

Figure 5.20: Measurement of *in vitro* PIK3C3 activity. (A) Schematic representation of the performed *in vitro* PIK3C3 activity assay. (B) Establishment of PIK3C3 activity assay for wild-type MEFs. Cells were incubated for 2 h in full medium (DMEM) or starvation medium (EBSS). Cleared cellular lysates were prepared, ATG14 immunopurifications of 2 or 4 mg total protein were performed and subsequently incubated with PtdIns and ATP. The PtdIns3P production was assessed by dot blot analysis and detection of a PtdIns3P binding protein (upper panel). Intensities were quantified and diagrams show fold change values normalized to control (medium treatment, lower panel). (C) PIK3C3 activity assay was performed analogously to B for *nrbf2 KO* MEFs retrovirally transfected with empty vector or cDNA encoding for the indicated NRBF2 variants. Detection of a PtdIns3P binding protein was measured (upper panel). Intensities were quantified and diagrams show fold change values normalized to controls (medium conditions). Results are mean ± SEM. One-way ANOVA (corrected by Tukey's multiple comparisons test) did not reveal any significant changes. n = 4 (lower panel).

The assessment of *in vitro* PIK3C3 activity for wild-type MEFs displayed an increase in PtdIns3P production after administration of amino acid starvation for 2 h. The amount of applied total protein for ATG14 immunopurifications did not influence the obtained results (Fig 5.20, B). For cells expressing mutated versions of NRBF2, an increase in PIK3C3 activity after starvation was detected for cells transfected with cDNAs encoding wild-type or 5S-D-NRBF2, with the stronger effect for the latter one. In contrast, for *nrbf2 KO* or 5S-A-expressing MEFs no increase in PtdIns3P production after starvation was detected. Instead, a slight decrease was overserved. Due to high variations between the single experiments, differences were not considered significant (Fig 5.20, C).

Analogously to the validation of results obtained by the *in vitro* kinase assay described above (compare 1.3.1), the *in vitro* PIK3C3 activity measurements were confirmed by an independent, physiological readout. In this case, the recruitment of the early autophagy protein WIPI2 to the emerging autophagosomes was monitored. Accumulation of WIPI2 is directly dependent on the PtdIns3P amount present at autophagosomal membranes generated by PIK3C3 [71] and can be analyzed by confocal microscopy.

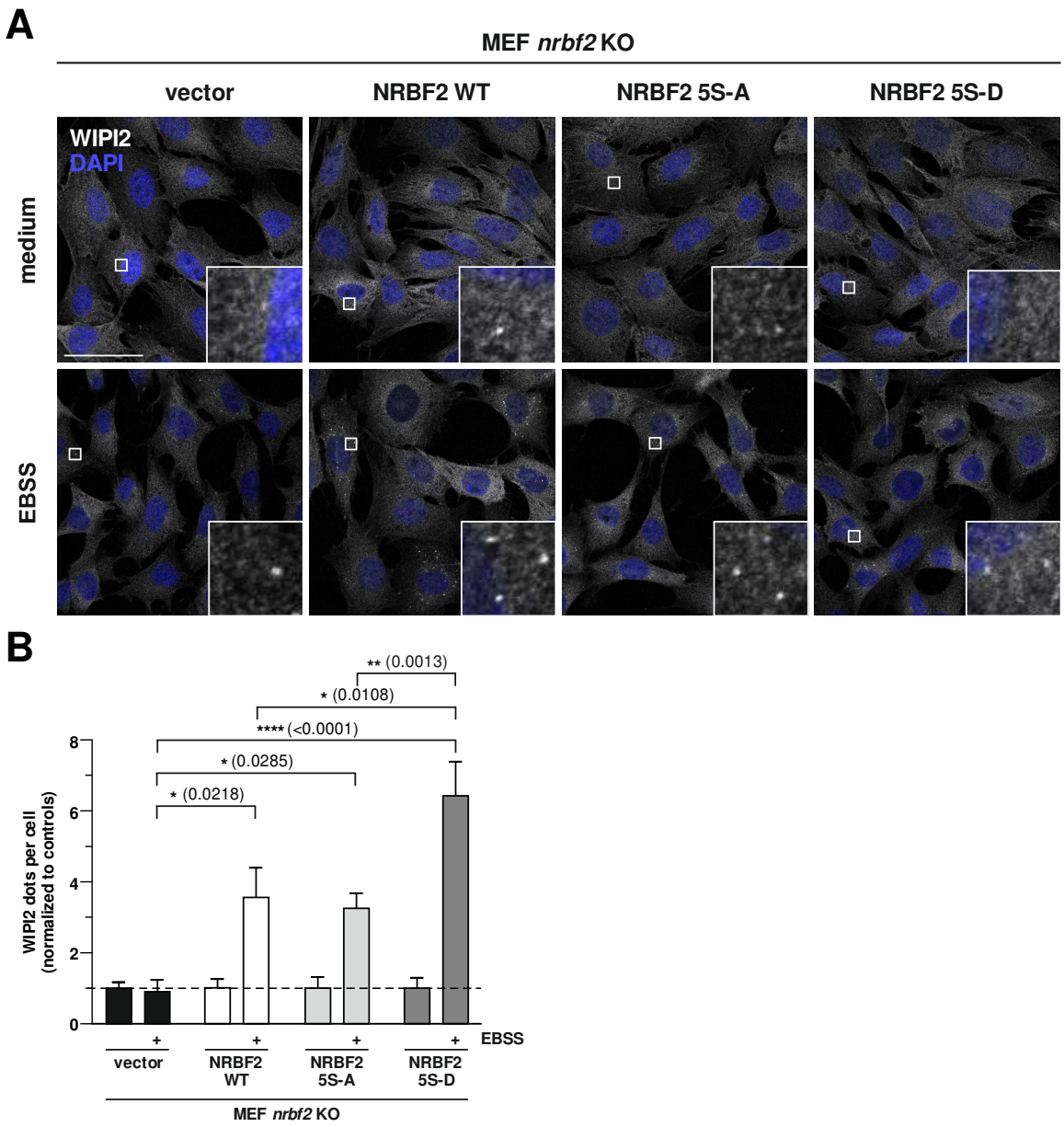

Figure 5.21: Mutations of NRBF2 phospho-acceptor sites regulate class III PtdIns3K complex activity. (A) *nrbf2 KO* MEFs retrovirally transfected with empty vector or cDNA encoding for the indicated NRBF2 variants were grown on glass cover slips overnight and incubated for 2 h in full medium (DMEM) or starvation medium (EBSS). Cells were fixed, permeabilized and immunostained for WIPI2. Imaging was performed using an inverse confocal laser scanning microscope. Scale bar: 50 µm. (B) A minimum of 100 cells per condition was analyzed and quantification was done using Fiji. Diagrams show number of dots per cell normalized to the control samples (corresponding medium treatment). Results are mean ± SEM. Statistical analysis was done by one-way ANOVA (corrected by Tukey's multiple comparisons test), *P < 0.05, **P < 0.01, ****P < 0.0001. Only selected significant differences are annotated. A complete list of P values for all calculated significant differences can be found in the addendum.

Induction of WIPI2 puncta formation after starvation was not detected for *nrbf2 KO* MEFs, but for all cell lines expressing any version of NRBF2. Cells expressing either wild-type or 5S-A-NRBF2 displayed a similar increase in WIPI2 puncta formation following starvation treatment. The phospho-mimicking NRBF2 5S-D variant displayed the strongest increase in PIK3C3 activity, which is in line with the previously performed *in vitro* PIK3C3 activity assay (Fig 5.21, B).

In summary, NRBF2 was identified as a member of the class III PtdIns3K complex. Impairment of the autophagic flux after deletion of NRBF2 in DT40 cells identified this protein as a positive regulator of autophagy. Additionally, autophagy-independent functions of NRBF2 were observed by investigations of PPAR-controlled gene regulation. NRBF2 interacts with PPAR alpha, localizes to the nucleus and is involved in the differential gene expression of *Ppara* itself and some other transcription factors after pharmacological activation of PPARs. Furthermore, a crosstalk of the ULK1 complex and the PtdIns3K complex in terms of ULK1-dependent NRBF2 phosphorylation was identified. A phospho-mimicking nRBF2 mutation hampered the PtdIns3K complex assembly by exclusion of ATG14 and NRBF2, which had no effect on the overall autophagic flux, but rather regulated the PIK3C3 activity in response to starvation.

6 Discussion

This thesis dealt with a detailed elucidation of the autophagy signaling pathway with special regard to the class III PtdIns3K complex. PIK3C3, the catalytically active component of this complex, is the only known class III PI3-kinase in eukaryotic cells and crucial for the formation of autophagosomal membrane structures and thus the initiation of autophagy. The aim was to investigate previously unknown regulatory mechanisms of the autophagy signaling pathway, which might also be of relevance for crosstalk with other cellular signaling pathways, such as programmed cell death (apoptosis). Especially with regard to medical research, this work might contribute to an extended understanding of various diseases and to a further development of pharmacological therapies. In healthy individuals, autophagy maintains cellular homeostasis and thereby contributes to the prevention of cancer or neurodegenerative diseases by circumventing DNA damage or clearance of protein aggregates and dysfunctional organelles. However, once cancer has developed, these cells can generate an increased nutrient supply and resistance to chemotherapeutics or radiation therapy by an upregulation of autophagic processes. In such cases, a targeted intervention to inhibit cellular autophagy would be the way of choice for clinical treatment. Meanwhile, chloroquine and hydroxychloroquine, which inhibit lysosomal acidification, have been applied successfully in phase 2 clinical trials for therapy of various types of cancer [96]. In contrast, treatment strategies for neurodegenerative diseases like Alzheimer or Parkinson disease aim for an induction of autophagic processes to counteract the formation of harmful protein aggregates (compare 2.1.3.1). In both cases, a detailed understanding of the underlying regulatory mechanisms of autophagy is essential.

In this context, NRBF2 was identified as a novel member of the PtdIns3K complex I and positive regulator of the autophagic flux. NRBF2 is a phosphorylation-target of the autophagy initiating kinase ULK1 to fine-tune the PIK3C3 activity in response to starvation, adding another level of crosstalk between the two autophagy-initiating protein complexes. Interestingly, NRBF2 comprises additional, autophagy-independent cellular functions, as it interacts with the nuclear receptor PPAR alpha and is involved in the regulation of its gene expression in response to PPAR stimulation.

6.1 Identification of NRBF2 as member of the class III PtdIns3K complex and characterization of its role in autophagy

The basis of this work was the performed mass spectrometric screening for novel interaction partners of BECN1. Nowadays the application of mass spectrometric methods for the identification of enriched or unknown proteins in a large scale has become an established methodology for the detailed characterization of entire signaling networks. In the present study, a label-free method using BECN1-GFP as a bait was performed in two human cell lines under growth and starvation conditions.

Protein identification by mass spectrometry displays some limitations like varying reproducibility due to relative protein abundancy or peptide cleavage. To overcome these limitations, the experiments were performed as technical replicates to enable a statistical analysis. All of the so far known interaction partners of the class III PtdIns3K complex were identified (PIK3C3, PIK3R4, BECN1, UVRAG and RUBCN) as significant interactors of BECN1. This outcome certifies the analysis as reliable and furthermore indicates that other identified proteins in this analysis are highly likely to be "true" interaction partners of BECN1 as well. Consequently, the fact that ATG14 was not enriched significantly in DG75 cells might not be due to inaccuracy. It might also be possible that complex formation is transient and not as stable for ATG14 in DG75 compared to other cell lines. Reaction conditions e.g. pH, salt and/or detergent concentration as well as sheer stress applied to samples during lysate generate might also have a more severe effect in DG75 cells.

In addition to the established BECN1 interaction partners, NRBF2 was found in the intersection between both cell lines, which displayed a weaker but still highly significant enrichment. Prior to the herein performed BENC1-interaction partner screening, Behrends and colleagues published a comprehensive analysis of the autophagy network emerging from several central nodes [170]. In this study, NRBF2 was identified as interaction partner of various members of the PtdIns3K complex and was even used as bait to identify further interaction partners. Probably due to the previously suspected divergent cellular function of NRBF2 (which is also evident from the origin of its name "nuclear-receptor binding factor 2"), this finding did not attract increased attention. The here achieved confirmation of the NRBF2 interaction with the PtdIns3K complex and the strong accumulation after immunopurification suggested an important function for NRBF2 in the regulation of

autophagy. For this reason and since no further studies were performed at that time, the further characterization of NRBF2 became the central project of this thesis.

It is noteworthy that the performed BECN1-interaction partner screening should not be considered as mere confirmation of Behrends et al., but is considered as an extension to the already existing data. First, an epithelial and a lymphatic cell line was allowing for investigation of possible cell type- and line-specific differences. This way, members of the 14-3-3 scaffold and adapter protein family were identified as binding partners of BECN1 exclusively in DG75 cells. The influence of 14-3-3 proteins on the autophagy signaling pathway by binding of various proteins as a result of phosphorylation has already been observed several times. Examples of negative effects on autophagy regulation like the binding and inactivation of TSC2 after phosphorylation by AKT, which results in an activation of mTORC1 [32], or the binding of phosphorylated PIK3C3 and the corresponding reduction of lipid kinase activity [193] are well documented. Examples for stimulation of autophagic processes by 14-3-3 proteins have been shown as a result of binding and inactivation of raptor after AMPK phosphorylation [25] or interaction with ULK1 [194]. Interestingly, direct or indirect effects on BECN1 could be shown specifically for 14-3-3 theta, which is one of the two 14-3-3 proteins identified in this thesis. As a result, an induction of autophagy was described for osteosarcoma and glioma cells, while an autophagy inhibition was shown in lung cancer cells [195–197]. This suggests that in DG75 cells autophagy might also be affected by direct interaction of 14-3-3 protein and BECN1. Since lymphomas are not subjected to impaired nutrient supply, it would be interesting to investigate whether and for what reason autophagy should be up- or downregulated in these cells. Exclusively for HEK293 cells and next to ATG14, an interaction of BECN1 with TSC1 and TSC2 was observed. The influence of TSC proteins on autophagy through modulation of mTORC1 activity has already been described (compare 2.1.2.1). However, direct interaction with BECN1 and thus a protein of the autophagy signaling pathway was only reported for TSC1 [170]. Again, it would be interesting to investigate to what extent a feedback mechanism exists between the PtdIns3K and the mTORC1 complex.

Further differentiations to the work carried out by Behrends et al. were the additional inclusion of autophagy-inducing conditions and the way of protein enrichment. Due to high purity of immunopurifications using GFP nanobodies and the utilization of free GFP as a control, this system is preferable to the use of HA and FLAG antibodies.

In retrospect, it would have been interesting to extend the performed experiments to several cancer cell lines for which an increased response to inhibition of autophagy has already been shown. However, the PtdIns3K complex might not necessarily be the primary target of dysregulation, which is why the whole autophagy signaling network should have been investigated. Additionally and with regard to the usage of EBSS as pro-autophagic stimulus, it has to be considered that this treatment does not reflect any physiological conditions. The supplementary use of pharmacological inducers of autophagy such as rapamycin or the novel class of highly selective mTOR inhibitors like Torin2 [198] could be considered in future experiments. Furthermore, it has to be taken into account that the baits used in this experiment were artificially overexpressed and that endogenous BECN1 was still present in the cell lines used.

For further characterization, a biochemical validation of the BECN1-NRBF2 interaction was achieved. Various co-immunopurification experiments on either overexpressed or endogenous protein level were successfully performed.

A comprehensive analysis of a protein's function and its specific effects is often achieved by removing the protein to be investigated from the cellular context and a subsequent investigation of the resulting changes. Methods to reduce cellular protein amounts, such as siRNA-mediated knockdown, are easy to apply, but the strength of the observable effects differs significantly from those of cellular knockout models. The establishment of such a cellular NRBF2 knockout, specific for DT40 cells, was aimed for and was achieved during this work. In the temporal context of these experiments, the DT40 cell system represented an attractive alternative to the prevailing knockout methods by ZFNs or TALENs. The increased rates of targeted to random integration of foreign DNA enable targeting of almost every gene at a reasonable cost/time ratio. Since DT40 cells are a chicken B-cell line, a high similarity of signaling pathways to other eukaryotic species can be assumed and furthermore a direct comparison to the previously used DG75 cell line is possible. However, the antibody-based detection of proteins is often hampered by larger differences in protein sequences, which was also the case for NRFB2. These problems can be minimized by the use of DNA/RNA-based screening methods and reconstitution with human proteins. From today's perspective, however, this system has lost its eligibility due to establishment of the simple, fast, reliable and intensely studied CRISPR/Cas9 knockout system. The groundbreaking possibility of targeted modification of any gene in any

transfectable cell system has recently led to a major progress in research [199]. In particular, the possibility of modifying genes and proteins under endogenous expression conditions by tagging or mutation can be linked as general opportunity for improvement to several of the experiments performed within this thesis. Therefore, the CRISPR/Cas9 system could be applied to expand performed analysis to a wide range of cell lines e.g. various cancer cell lines as suggested before. Nevertheless, the generated NRBF2 DT40 knockout was genetically validated and, in combination with reconstitution by human NRBF2, was used for further experiments. A function for NRBF2 as a positive regulator of autophagy was shown by measurement of LC3 turnover by immunoblot and should be examined in more detail by further experiments like immunofluorescence microscopy of GFP-WIPI or RFP-GFP-LC3. In addition, a more precise determination of domains mediating the interaction with the PtdIns3K complex should be performed by generation of truncated NRBF2 versions and subsequent pulldown experiments. The fact that nearly simultaneously three independent research groups published comprehensive characterizations of NRBF2 in the eukaryotic system underlined the relevance of this project. While Zhong and colleagues identified NRBF2 as a negative regulator of the PtdIns3K complex and thus of autophagy [55], Lu et al. and Cao et al. observed a positive influence on induced autophagy, while basal autophagy rates were not affected [53,54]. The discrepancy between these observations shows that a final, unifying theory of the NRBF2 function in autophagy has yet to be established.

In the context of this work, two yet unexplored aspects were examined more closely:

1) Is NRBF2, besides its function as a regulatory protein during autophagy, also involved in the long-term transcriptional control of autophagy-related genes?

2) Is the autophagic function of NRBF2 influenced by phosphorylation as a post-translational modification?

6.2 NRBF2 interacts with the nuclear receptor PPAR alpha and is involved in the transcriptional control of various genes

As already described in the introduction, an involvement of various transcription factors in the transcription of autophagy-related genes was shown as a cellular response to prolonged starvation periods. A particularly outstanding position can be accounted to the

FXR-PPAR alpha-CREB axis due to the regulation of a large number of core ATG genes. However, what has never been shown so far is the direct involvement of certain ATGs in the transcriptional control of other ATGs. Such a function was suspected for NRBF2 and examined in more detail in the second part of this thesis. The assumption of such a theory is due to the apparently ambivalent cellular functions of NRBF2. The original identification of NRBF2 as an interaction partner of nuclear receptors by yeast two-hybrid screening [175] was followed by the clarification of the regulatory function within the autophagy signaling network [53–55]. The later observed extensive transcriptional regulation of core ATGs by PPAR alpha [129] now suggests a connection between these two cellular functions of NRBF2. This theory is also supported by further publications, which could show an additional influence of the nuclear receptors PPAR beta/delta and PPAR gamma on the regulation of autophagic processes [177,178].

Such a direct link between short- and long-term control of autophagic processes would represent a new dimension of regulatory mechanism. Feedback signals coming directly from the autophagic flux could enable a more precise temporal control of transcriptional processes or convey the need for a prolonged upregulation. Specialized feedback signals adjusted to the occurring stress situations might also be conceivable. PPAR alpha is a general regulator of fatty acid oxidation and ketogenesis in the liver, which might suggest an additional link to lipophagy, the specific breakdown of lipid droplets by autophagic processes. As a further support of this theory, it has to be stated that nuclear functions could already be demonstrated for other ATGs independently of their role in autophagy. ULK1 for example is involved in the regulation of necrotic cell death by activation of nuclear PARP1 [200].

As prerequisites for a transcriptional function of NRBF2, the subcellular localization and the interaction with members of the PPAR nuclear receptor family had to be investigated. By various co-immuno- and affinity-purification experiments, an interaction of NRBF2 with PPAR alpha was confirmed, whereas this was not possible for the interaction with PPAR gamma. PPAR beta/delta was not examined in more detail due to the lack of suitable antibodies. It should be noted that the use of C-terminally tagged NRBF2 prevented interaction with PPAR alpha. Furthermore, immunofluorescence microscopy was able to detect both a cytosolic and a weaker nuclear localization of NRBF2, which was influenced by induction of autophagy or pharmacological activation of the individual PPAR family

members. According to an *in silico* prediction based on observations by Kosugi and colleagues [201], NRBF2 itself has a bipartite nuclear localization signal (NLS, amino acid 175 to 204) that occupies most of the coiled coil region (amino acid 168 to 209). However, only a weak nuclear localization is calculated for this NLS, which supports the results obtained by immunofluorescence microscopy.

In further experiments, observations reported by Palomer and colleagues [177] or Li and colleagues [178] about upregulation of BECN1 and LC3-II protein levels after pharmacological activation of PPARs were examined for their dependence on NRBF2. In the murine hepatic cell line AML12, which was also used by Lee and colleagues, these described effects could be confirmed, thereby also confirming the effectiveness of the employed pharmacological PPAR agonists. In addition, a regulation as a response to PPAR activation was also shown for ULK1 as another protein relevant for the regulation of autophagy. This experimental setup was then transferred to NRBF2-deficient MEF cells. By comparison of wild-type and NRBF2-deficient cells or of *nrbf2* KO cells which were either reconstituted or vector-transfected, an influence of NRBF2 on the observed regulation of protein expression was indeed observed. The most prominent effects were consistently observed for the PPAR alpha agonist Wy14643. Already Lee and colleagues used the PPAR alpha agonist Wy14643 for cell culture applications, while the other PPAR agonist GW7647 was used for the treatment of living mice. However, it must be noted that the observed effects in MEF cells, especially for BECN1, were considerably weaker compared to AML12 cells. One reason might be the fact that the used MEF cell lines are not of hepatic or adipose origin where the PPAR family exerts their main functions. The fact that nevertheless some effects could be observed in epithelial cells might indicate a conserved regulatory mechanism.

At this point, the potential of the CRISPR/Cas9 technology has to be considered once again. The establishment of a NRBF2 deficient hepatic cell line could have enabled investigations in an accurate physiological context. Firstly, it should be noted that increased protein levels are not necessarily due to transcriptional changes. Stabilization effects due to post-translational modifications might also be a possible explanation [202]. Secondly, increased protein levels of some ATGs are not equivalent to an increased induction of autophagy. This assumption must always be accompanied by additional measurements of the autophagic flux. In the context of the here performed experiments, a more precise quantification of

protein levels for example by ELISA would be helpful for a better evaluation of actual treatment efficiency.

In summary, a NRBF2-dependency of PPAR-stimulated protein expression of several ATGs was observed, which supports the theory of a transcriptional function of NRBF2. In the further course of this thesis, the influence of NRBF2 on the general cellular transcription was monitored by microarray analysis. Therefore, the NRBF2-knockout MEF cells either reconstituted or vector-transfected were used. In addition, the influence of starvation was investigated by EBSS treatment.

The obtained results have to be evaluated with regard to their point of comparison. In order to estimate the influence of NRBF2-deficiency, the genes differentially regulated between both cell lines have to be examined under growth and starvation conditions. Only about 1300 genes were differentially regulated and only to a moderate level. To assess the influence of starvation conditions, the differentially regulated genes of each cell line must be compared between medium and EBSS treatment. In NRBF2-deficient cells, an elevated number of almost 3000 genes was identified. Additionally, stronger regulations up to factor 5 were detected.

The representation as Venn diagram helps to distinguish which subset of regulated genes might be of particular interest. For comparison of the two cell lines, all differential expressed genes are caused by NRBF2-deficiency and hence are interesting candidates. The intersection of 86 candidates marks the gene regulations, which occur regardless of the culturing conditions and therefore are of “general” importance after NRBF2-defiency. Nevertheless, the 918 candidate genes identified under medium conditions or the 847 candidate gens for starvation conditions are still interesting candidates, albeit restricted to external stimulation. By consideration of significance- and fold-change values, only *Stat2*, *Irf7*, *Il6* and *Pex7* remained for this comparison. The first three genes can be directly related to autophagy due to their roles in "immunological autophagy". This term refers to the involvement of autophagic processes in innate or adaptive immune responses for elimination of intracellular bacteria or for processing and presentation of antigens by the major histocompatibility complex class I and II [104,105]. Various cytokines like interleukin (IL)-1, IL-2, IL-6, tumor necrosis factor (TNF) alpha and both type I and type II interferon (IFN) are autophagy inducers, while IL-4, IL-10 and IL-13 have restrictive functions [203,204]. In addition, a reversed regulatory influence of autophagy on cytokine production can be

observed. Thus, increased rates of autophagy cause increased production and secretion of IL-6 by activation of STAT3 [205], while an interruption of normal autophagic flux is associated with increased secretion of pro-inflammatory cytokines IL-1β and IL-18 [206,207]. In turn, IRF7 and IRF3 are involved in the production of pro-inflammatory type I interferons after the activation of Toll-like receptors (TLR) 2 and 4 [208]. Type I IFN like IFN α cause signal transduction via the JAK/STAT pathway [209], where also STAT2 is located. These identified regulated genes suggest a putative involvement of NRBF2 in immunological processes. However, it has to be questioned how suitable the used MEF cell system is for the detection and further investigation of immunological processes. In the future, these results have to be confirmed in a more suitable model system like Raw267 cells, a macrophage cell line for the study of pro-inflammatory cytokines.

On the other hand, no obvious connection to autophagy can be found for *Pex7*, which was differentially regulated under both medium and EBSS treatment. As a cargo receptor, PEX7 is responsible for the recognition of proteins which contain peroxisomal targeting signal (PTS) 2 motifs and their subsequent import into the peroxisome, where β-oxidation of fatty acids takes place [210]. A connection to autophagy is suggested only by a common subcellular localization with TSC1, TSC2 and Rheb on peroxisomes. In response to ROS, TSC1 and TSC2 are bound by PEX19 and PEX5, thereby hampering mTORC1 activity [211]. With regard to the cellular functions of peroxisomes, which are key metabolic organelles for fatty acid beta-oxidation [212], a close connection to PPAR alpha signaling is obvious. Expression of many genes involved in peroxisomal beta-oxidation is controlled by PPAR alpha [213], the herein used *Acox1* as positive control for PPAR alpha stimulation is one of them. Furthermore, the molecular mechanisms of pexophagy, the selective degradation of peroxisomes, constantly emerges. Displaying a half-life of about 2 days, the formation and degradation of Peroxisomes suggests a dynamic process [214]. Upon impairment of peroxisomal function, ubiquitination of PEX5 enables interaction with SQSTM1/p62 or NBR1 and subsequent autophagic degradation [215]. Additionally, PEX14 is able to directly interact with LC3 [216]. So far, no direct involvement of PEX7 in these processes is known, nevertheless the NRBF2-dependent differential regulation of a PPAR alpha target gene suggests a functional connection. This may not exclusively be an autophagic function, also a general, lipid kinase related function might be possible. This could be further investigated with regard to pexophagy or in tissue specific context with PPAR alpha function (e.g. in hepatic tissue).

The microarray data was further analyzed in the context of the influence of growth conditions. Differential regulation of several ATGs necessary for the induction of autophagy was identified in NRBF2-expressing cells after starvation, which was abolished by NRBF2 deficiency. For this situation, an increased number of transcription factors like *Jun*, *Nfkb1*, *Rarg* and *Rxra* were found among the regulated genes. The latter two even belong to the class of nuclear receptors, where *Rxra* is of essential importance for the transcriptional activity of PPARs as it represents the heteromeric interaction partner of all PPAR family members [217]. It is a hypothetical consideration, whether this regulation of *Rxra* in NRBF2-deficient cells represents some kind of feedback or compensation mechanism, since in this scenario NRBF2 is not available for "normal" PPAR alpha-mediated transcription.

In addition, an *in silico* performed cluster analysis of the most promising gene-subsets displayed a frequent occurrence of genes involved in lipid metabolism, which is not surprising regarding the cellular function of PPAR alpha, but illustrates a possible link to NRBF2 function.

With regard to the cell lines used for microarray analyses, it must generally be kept in mind that not all detected differences must be attributed to the absence of NRBF2. It is a common phenomenon that in response to the lack of a certain protein, cells perform various types of compensation mechanisms [218]. Ideally, conditional knockout systems can be used, where the protein to be examined is removed from the cellular context immediately before analysis. Regardless of advantages by the CRISPR/Cas9 technology, the generation of such systems is still quite elaborate. Instead of performing a microarray analysis, where identification is based on hybridization reactions with known gene sequences immobilized on the microarray chip, it would nowadays be possible to perform RNA-Seq experiments. This method uses new deep-sequencing technologies to enable a direct sequencing of RNA and is therefore not limited to a certain number of known genes [219]. Since RNA-Seq enables the identification of e.g. regulatory RNAs, which are commonly not entirely covered by a microarray-chip, this method can be advantageous, but would have provided only minor improvements during this thesis.

Validation of the genes identified by microarray was done by relative quantification of real-time quantitative reverse transcription (qRT)-PCR experiments [182]. Due to the large number of genes to be investigated, primer pairs were individually designed and successfully tested for their amplification efficiencies. Thus, influence of the NRBF2 knockout on the

expression of the respective genes was further investigated. The obtained results were consistent with those from the microarray analysis and displayed only mild regulation of about 20% for most genes. As expected, *Stat2* and especially *Irf7* were downregulated strongly by comparison of NRBF2-deficient and NRBF2-expressing cells. The observed strong downregulation of *Ppara* in NRBF2-defienct cells in combination with no alterations of the heteromeric interaction partner *Rxra* were somehow surprising, especially since *Ppara* was not identified by microarray analysis. These findings might indicate a positive interplay between NRBF2 and PPAR alpha, and in this way, the absence of NRBF2 also hampers *Ppara* expression.

Treatment with EBSS as a pro-autophagic stimulus significantly altered expression of all analyzed genes except for *Rxra* and *Jun*. For all ATGs expected upregulations were confirmed, which was quite strong e.g. for *Bnip3* [112,220]. The investigated transcription factors were either clearly up- *(Rarg*, *Stat2*, *Foxo3* and *Irf7*) or clearly downregulated *(Nfkb1* and *Ppara*), which was not expected for the latter ones. Besides the positive influence on autophagy by increased transcription of some ATGs, also an activation of mTOR and the subsequent inactivation of autophagy following TNF treatment [221] was shown for the NF-κB signaling pathway, which might explain the observed repression of *Nfkb1* transcription. However, it is not clear why transcription of *Ppara* was repressed by EBSS treatment, since PPAR alpha was linked to the transcriptional upregulation of various ATGs after starvation [129]. If this downregulation represents some kind of feedback mechanism remains speculative. Furthermore, the clear repression of *Il6* contradicts the observations made by Zhang and colleagues, which postulated a positive effect of increased autophagy [205]. Upregulation of *Irf7* transcription supports the reported beneficial effects of autophagy on immunological processes. The genes *Acox1*, *Sesn2* and *Ctsf* were used as positive controls for PPAR alpha regulated gene expression [129] and all displayed clear upregulations. However, NRBF2-dependent differences were not observed. The use of the pro-autophagic stimulus EBSS can be a possible explanation, since NRBF2 might be engaged in the execution of autophagic pathways and therefore has lower transcriptional activity.

To conclude the investigations on the influence of NRBF2 on transcriptional processes, gene regulation following pharmacological PPAR-activation was investigated. Here, many of the examined genes were not affected at all, or the observed effects were rather small compared to the previously performed EBSS treatment. The most prominent differential

gene regulation could again be observed after activation of PPAR alpha by Wy14643, but a general influence of NRBF2 was not obvious. Strikingly, *Uvrag* was the only ATG to show a repression after activation of PPAR gamma and beta/delta, but was upregulated after PPAR alpha activation. Accordingly, some other ATGs (e.g. *Bnip3*, *Tsc1* or *Wdr45*) were slightly downregulated by PPAR gamma activation. This might indicate different functional connections between the PPAR family members and the transcriptional control of autophagy. As stated under 2.1.5, PPAR gamma is centrally involved in adipocyte differentiation and its function cannot be compensated by PPAR alpha or beta/delta. Lately, an involvement of autophagy in adipocyte maintenance was unraveled. Beige adipocytes, the second form of thermogenic adipose tissue [222], can lose the morphological and molecular characteristics and acquire characteristics of white adipose tissue. This transformation is associated with an increase in mitochondrial clearance by autophagy [223] and might counteract the physiological functions of PPAR gamma, which is why the here observed downregulation of ATGs could function as a supporting mechanism of adipocyte differentiation. The simultaneous upregulation of *Uvrag* and other ATGs by PPAR alpha activation underlines the importance of a specific context for autophagy regulation. If the observed slight increase in gene expression of these ATGs corresponds to an increased autophagic activity in PPAR alpha specific tissue (e.g. hepatic cells) should be investigated and presumably correlates with increased lipid catabolism.

Many of the genes associated with immunological processes of autophagy like *Nfkb1*, *Irf7*, *Stat2* and *Il6* displayed similar repression after activation of PPAR gamma and beta/delta. The observed negative regulation of immunological relevant genes suggests a general role for PPAR gamma and beta/delta opposed to PPAR alpha and might illustrate their different functions for lipid metabolism and adipose tissue differentiation already described in 2.1.5. Supporting evidence can be drawn from the proposed anti-inflammatory functions described for PPAR gamma [224]. For further investigations of this observed negative regulation of pro-inflammatory immune signaling, a more suitable cell system than murine embryonic fibroblasts should be applied.

However, the most interesting finding was a general and opposing regulation pattern for *Ppara* and *Rxra*, which additionally seemed to be NRBF2-dependent. NRBF2-deficient cells tended to show little change, while cells in which NRBF2 was expressed displayed repression of *Ppara* and upregulation of *Rxra* after stimulation of any PPAR. This repression

of *Ppara* was also found in the previous experiments using EBSS as stimulus. Whether this might be some kind of compensation process after activation of a corresponding PPAR has to be further investigated. That NRBF2-deficient cells did not display this regulation pattern for *Ppara* might be due to the already existing downregulation of *Ppara* due to NRBF2 deficiency.

However, it must also be noted that the genes *Acox1* and *Sesn2* used as positive controls for PPAR alpha stimulation showed only minimal reactions after treatment with Wy14643, which is in contradiction to the observations made by Lee and colleagues [129]. However, ineffectiveness of the used PPAR agonists can be excluded due to the successful application in previous experiments.

To conclude this part of the thesis, it can be stated that NRBF2 has indeed an influence on transcriptional processes. Autophagy-related genes are not necessarily regulated, but rather a number of transcription factors and cytokines involved in immunological autophagy. The fact that the use of the pro-autophagic stimulus EBSS in murine embryonic fibroblasts did not result in any NRBF2-dependent differences in gene transcription might indicate a function for NRBF2 only in combination with certain types of stimuli and/or in special cell type backgrounds. This might be an immunological stimulus, indicated by the many immunological relevant genes found to be differentially regulated by NRBF2 deficiency. Additionally, it might be worthwhile trying a combined stimulation by EBSS and PPAR-activation, to investigate if PPAR-dependent gene regulation can be shifted by starvation conditions to affect more ATGs. A reason, why the applied activation of PPARs did not result in strong changes of gene expression might be that the investigated genes were chosen on the basis of the performed microarray analysis using EBSS as stimulus. Starvation and PPAR activation do not necessarily induce similar transcriptional responses. A focus on validated PPAR target genes might reveal stronger NRBF2-dependent transcriptional reactions. In addition, NRBF2 seems to have an influence on its direct interaction partner PPAR alpha and thus also on RXR alpha, which might suggest a possible connection to PPAR alpha-mediated processes of lipid metabolism (possibly via lipophagy, the autophagosomal degradation of lipid droplets). However, how exactly the autophagic and transcriptional functions of NRFB2 are interconnected needs to be investigated in future experiments. Is NRBF2 initially involved in autophagosome biogenesis and are the

transcriptional functions only executed when its function is no longer mandatory during late stages of the autophagic flux? Alternatively, are both functions performed in parallel, or does a hierarchy of relevance exist? Can one function be specifically stimulated without influencing the other? All these questions might be further clarified by identification of NRBF2-domains required for interaction with PPAR alpha. A sequence motif necessary for interaction with nuclear receptors has already been identified in NRBF2, but its relevance has to be characterized in more detail. However, due to the co-immunopurification experiments performed here, the importance of the C-terminus of NRBF2 is likely. A participation of further co-factors in mediating the interaction or nuclear localization cannot be excluded either. Here, further information could be generated by artificially introducing a strong NLS or even a nuclear export signal (NES) into the NRBF2 sequence. It might also be of interest to clarify the differences between the individual PPAR family members with regard to NRBF2-dependent transcription processes. Are these function- or cell type-dependent? Future experiments should focus on the two remaining PPAR isoforms gamma and beta/delta. Although no evidence for a direct interaction of NRBF2 and PPAR gamma has been found so far, some transcriptional connections seem to exist. Especially, regulation of genes related to immunological processes might fit to the cellular functions of PPAR gamma.

Finally, it can be assumed that more prominent effects for PPAR alpha activation can be observed in a hepatic cell system. This should also be considered for further investigation of the identified immunological genes. The CRISPR/Cas9 system can be utilized to accomplish some of these aspects.

6.3 ULK1 regulates the class III PtdIns3K complex via the phosphorylation of NRBF2

In the third and last part of this thesis, aspects of a putative phosphorylation of NRBF2 by ULK1, the central kinase of the autophagy signaling pathway, and its possible influence on the class III PtdIns3K complex and on the general autophagic capacity were investigated.

Although the integration of NRFB2 into the PtdIns3K complex as an additional subunit has been demonstrated sufficiently, there is still no consensus on the exact regulatory function of NRBF2. The existence of an additional regulation of NRBF2 function by PTM such as phosphorylation might help to connect these controversial theories. Since the direct

regulation of downstream components of the autophagy signaling pathway by ULK1, possibly due to the relatively low sequence specificity, is a frequently occurring regulation mechanism and might also apply for NRBF2. Additionally, the recent identification of autophagy-independent functions of NRBF2 in the previous part of this work indicates the need for regulatory mechanisms to control these two functions independently and possibly by phosphorylation. In advance to this work, two large scale kinase screens already identified two phospho-acceptor sites in NRBF2 (Ser113 and Ser168), without further clarification of the exact function or the mediating kinase [188–190]. Later on, Ser113 and additionally Ser120 were attributed to mTORC1 [185].

Further evidence for the existence of a NRBF2 phosphorylation was gathered by an initial *in vitro* kinase assay using GST-NBRF2 and crude cellular lysates of HEK293 cells, revealing a weak phosphorylation signal mediated by one or more kinases. By optimization of the substrate purification process and by utilization of recombinant ULK1 as kinase, a specific NRBF2 phosphorylation by ULK1 was demonstrated *in vitro.* For further confirmation the ULK1 inhibitor MRT67307 was used, which prevented phosphorylation of NRBF2. It has to be noted that MRT67307 is not solely ULK1 specific, but possesses highest selectivity for TBK1 instead [187]. However, since purified ULK1 was used in the experiment, this point does not need further consideration. Additionally, a possible degradation band could be observed for the used substrate, which also showed a weak signal in autoradiography. The phosphorylation status of NRBF2 following *in vitro* kinase assay was analyzed by mass spectrometry, identifying phosphorylation of five serine residues. This elevated number of phospho-acceptor sites may be due to the rather low sequence specificity of ULK1, which may lead to non-specific phosphorylation events during *in vitro* experiments. Nevertheless, a reduction of the phosphorylation signal to background values was achieved in an *in vitro* kinase assay after mutation of all five identified phospho-acceptor sites to alanine.

In addition, the identified phosphor-acceptor sites displayed a high degree of conservation between several eukaryotic species. However, a comparison with the recently identified NRBF2 orthologue ATG38 in yeast [50] is not possible due to high sequence differences. With regard to the reported ULK1 consensus motif, Ser50, Ser56 and Ser277 meet the criteria of hydrophobic amino acids at the -3, +1 or +2 position. Regarding the crystal structure of the MIT domain of human NRBF2, strikingly Ser50 and Ser56 are located in the connection of two alpha-helical structures and thus are easily accessible, whereas Ser15 is located at the

center of a helical region. Since association with the PtdIns3K complex is mediated via an interaction of the NRBF2 MIT domain and a coiled coil domain of ATG14, this location of the two phospho-acceptor sites is particularly interesting with regard to possible structural changes. Ser101, similar to both mTORC1-dependent phospho-acceptor sites Ser113 and Ser120, is located centrally in the protein sequence, but this certain section is missing in a second isoform of NRBF2 (COPR1, also identified in the original yeast two-hybrid screen by Flores et al.). The fifth identified ULK1-dependent phospho-acceptor site Ser277 is located at the C-terminal end of NRBF2. According to Ohashi et al. [51] and Araki et al. [50], the NRBF2 C-terminus is responsible for the homodimerization of two monomeric forms of NRBF2 and localization to the PAS. Additionally, this serine may be of interest with regard to the role of NRBF2 C-terminus for the interaction with PPAR alpha described in this thesis.

For verification of the obtained *in vitro* kinase assay results in intact cells, a modified version of the PLA was performed to detect post-translational modifications like phosphorylations by using an antibody that recognizes phosphorylated serine residues. The comparison of wild-type and NRBF2-deficient MEF cells after treatment with medium displayed a clear reduction of PLA signals in NRBF2-deficient cells. However, to exclude possible influences due to the genetic heterogeneity between these two cell lines, no further experiments investigating the effect of EBSS-stimulation were performed. Instead, wild-type MEF cells were depleted for NRBF2 by siRNA knockdown and subsequently used for PLA following either medium, EBSS or combination treatment of EBSS and the ULK1 inhibitor MRT67307. Again, a significant reduction of PLA signals was observed in cells with reduced NRBF2 expression. In addition, an increase due to EBSS treatment was blocked by inhibition of ULK1. Taken together, the performed *in vitro* kinase assays suggest a ULK1-dependent phosphorylation of NRBF2 at multiple sites. This hypothesis is supported by PLA experiments in intact cells. Due to its unconventional use, some aspects have to be considered about the performed PLA. The siRNA knockdown efficiency and the utilized antibodies exert a major influence on the obtained results. By using an antibody against phosphorylated serine residues, also the detection of serine-phosphorylated interaction partners of NRBF2 is possible in theory. Although this becomes less likely with increasing distance, it cannot be excluded within the 40 nm limit specified by the manufacturer. However, there are few alternatives for an *in vivo* detection of protein phosphorylation without the use of phospho-specific NRBF2 antibodies. Methods based on selective dye

labelling or the specific retention of phospho-groups in a gel matrix such as Pro-Q® Diamond or Phos-tag™ do not offer sufficiently high sensitivity. Enrichment by immunopurification and subsequent detection by immunoblotting or the recently available homogeneous time resolved fluorescence (HTRF) or bioluminescence resonance energy transfer (BRET) methods would again be based on the use of anti-phospho-serine antibodies. However, by inclusion of several control experiments, it would be possible to validate the specificity of the performed PLA. Treatment with λ-phosphatase could generally determine whether the detected signals are caused by phosphorylation. Furthermore, mutation of the five identified phospho-acceptor sites in the NRBF2 gene using the CRISPR/Cas9 technique could verify whether specific NRBF2 phosphorylation is detected.

After accomplishing the identification of putative phospho-acceptor sites, these were analyzed for their cellular function. In addition to the already used pan serine to alanine mutant (5S-A), a pan serine to aspartate mutant (5S-D) was generated to mimic a constitutive phosphorylation status. These two NRBF2 variants were stably expressed in NRBF2-deficient MEF cells and, together with the already reconstituted and vector transfected cells, they were used for subsequent experiments. A strong expression was detected for all NRBF2 versions by immunoblot, whereby the 5S-A version showed a slight difference in migration pattern. An increased proteasomal degradation was excluded by application of the proteasomal inhibitors bortezomib or MG-132 (data not shown). However, an additional testing of protein stability after inhibition of *de novo* protein synthesis by cycloheximide could be performed.

In the further course, the influence of NRBF2 phosphorylation on the composition of the class III PtdIns3K complex was investigated by size exclusion chromatography experiments. Generally, the PtdIns3K complex was detected in a molecular mass range from 670 to 400 kDa for all investigated cell lines. No preference for a monomeric or a dimeric form of the complex, but rather a continuous transition between both forms was observed, which is in contrast to observations made by Ohashi and colleagues, who described an oligomerization status depending on the relative abundance of NRBF2 [51]. However, these observations were made after addition of recombinant NRBF2 to the purified heterotetrameric complex of PIK3R4, PIK3C3, ATG14 and BECN1 from HEK293T cells, which might account for differences compared to the *in vivo* results obtained in this work.

The core complex of PIK3C3, PIK3R4 and BECN1 was not affected by the phosphorylation status or deficiency of NRBF2, but significant changes were observed for the additional complex I or II components NRBF2, ATG14 or UVRAG, respectively. The majority for each NRBF2 variant was observed around 180 kDa and thus not incorporated in the PtdIns3K complex, though small amounts of the wild-type and unphosphorylated NRBF2 were integrated into the core complex under medium conditions. The existence of a low molecular mass population also indicates the possibility of further, possibly autophagy-independent cellular functions of NRBF2, which might be connected to the above described transcriptional effects of NRBF2. For ATG14, each cell line displayed a somehow different migration pattern. For the presence of wild-type NRBF2, ATG14 is located exclusively in the PtdIns3K core complex, whereas the NRBF2 5S-A mutant causes the appearance of a second ATG14 population below 160 kDa. The NRBF2 5S-D mutant causes ATG14 to migrate exclusively in this new population, while NRFB2 deficiency causes a partial shift of ATG14 to a molecular mass range slightly higher than the core complex. UVRAG was detectable under 160 kDa for all conditions and, besides for the 5S-D mutant, small parts of UVRAG were always present in the core complex. Without further investigations of autophagic capacity, it is difficult to assign a certain meaning to these observations. However, it must be kept in mind that these observations were made on the basis of phosphorylation mimicry, which might not be an equivalent substitute for a “real” phosphorylation. In general, most proteins are not abundantly present in a phosphorylated or unphosphorylated state, but more realistically pools of the same protein with varying modification status exists which ratios are subjected to change upon stimulation. Therefore, ectopic expression of the NRBF2 phospho-acceptor mutants generates a very artificial system omitting the significance of hierarchical transition of protein modifications. Furthermore, in case of the NRBF2 5S-D variant, only one single protein is present in a phosphorylated state, while all other components of the PtdIns3K complex are likely unphosphorylated. It cannot be excluded that physiological interactions request a coordinated phosphorylation status of all components, which is why these experiments should be repeated under autophagy-inducing conditions. In addition, the introduced amino acid substitutions can affect the protein structure and thereby the interaction capacity, which should be further investigated by co-immunopurification experiments.

Furthermore, increased and non-physiological protein expression levels might also influence the performed experiments.

For further validation of the obtained results, additional size exclusion chromatography experiments were performed using ULK1/2 double-deficient MEF cells. Here a NRBF2 and ATG14 migration pattern similar to wild-type or unphosphorylated NRBF2 could be observed, supporting the previous experiments.

To assess the general autophagic capacity, the turnover of LC3-II and SQSTM1 and the LC3-dot formation were investigated by immunoblot and immunofluorescence microscopy. Regardless of the NRBF2 phosphorylation status, no strong effect on the autophagic flux was detected. However, Lu and colleagues already highlighted that NRBF2 does not play an essential role in basal autophagy, but rather modulates PIK3C3 activity in response to various stimuli [54]. This assumption is supported by the results of NRBF2-deficient cells, which displayed an autophagic flux comparable to wild-type cells.

As an experimental validation of this assumption, the PIK3C3 activity was monitored in relation to the phosphorylation status of NRBF2. First, an *in vitro* assay was performed where the PIK3C3 activity of the PtdIns3K complex co-immunopurified via ATG14 is measured by detection of the *in vitro* generated PtdIns(3)P amount. This method was successfully tested in wild-type MEF cells and transferred to MEF cells expressing mutant NRBF2 versions. A slight increase in PIK3C3 activity was observed for wild-type NRBF2 and a clearly stronger increase for the 5S-D mutant, while the 5S-A mutant and NRBF2-deficient cells displayed a slight reduction in PIK3C3 activity. In retrospect, however, the results of this assay have to be evaluated critically. The exclusion of ATG14 and NRBF2 5S-D from the PtdIns3K complex observed by size exclusion chromatography questions the applicability of immunopurifications via ATG14. The fact that despite a possibly hampered co-immunopurification of the PtdIns3K complex still an increase in PIK3C3 activity was measured for the 5S-D mutant might indicate a strong influence of NRBF2 phosphorylation on the PtdIns3K complex. Nevertheless, this experiment has to be repeated for immunopurifications of another PtdIns3K complex component. The additional use of radioactively labeled ATP could replace fluctuating immunoblot detections.

As completion of the third part of this thesis and for the validation of PIK3C3 activity, the accumulation of the PtdIns(3)P-binding protein WIPI2 was investigated *in vivo* using immunofluorescence microscopy. The results obtained mainly coincide with the previously

performed *in vitro assay.* No increase in WIPI2 accumulation after EBSS treatment and thus an unchanged PIK3C3 activity could be determined for NRBF2-deficient cells, which again is in line with Lu et al. However, the presence of any NRBF2-version caused an increase in WIPI2 dots after stimulation. In contrast to the *in vitro assay*, the 5S-A mutant displayed a comparatively weak induction of PIK3C3 activity, while the 5S-D mutant again showed the most pronounced increase in PIK3C3 activity. Fluorescence microscopic analysis of other PtdIns(3)P-binding proteins such as DFCP1 or GFP-2xFYVE should be performed for a possible verification of these results.

In summary, the ULK1-dependent phosphorylation of NRBF2 on multiple sites was detected *in vitro* and could be confirmed by PLA in intact cells. After mutation of these residues, an influence on the PtdIns3K complex assembly was determined. Under medium conditions, phosphorylated NRBF2 excludes itself, ATG14, and UVRAG from the PtdIns3K core complex. This did not result in interference of the general autophagic flux, but a significant increase in specific PIK3C3 activity in the presence of the NRBF2 5S-D mutant was detected.
This observation might be explainable as follows: The ULK1-dependent phosphorylation of NRBF2 causes a sensitization of the PtdIns3K-complex I for activation by nutrient deprivation, which manifests in an increased PIK3C3 activity after pro-autophagic stimulation. At lower ULK1 activity under basal conditions, mimicry of the NRBF2 phosphorylation seems to interfere with the complex assembly and thus hampers the basal activity of PtdIns3K complex I. It is possible that the order of ULK1-dependent phosphorylation events of the complex components BECN1, ATG14, PIK3C3 and NRBF2 are of importance for the activation or the activity of PtdIns3K complex I. This chronological hierarchy is artificially disturbed by the integration of phosphorylated NRBF2 without accompanying phosphorylation of the other complex components.
Nevertheless, some similar aspects between results obtained during this thesis and observations reported by Araki and Ma and colleagues are obvious. Araki et al. observed that in yeast one ATG38 dimer interacts via the N-terminal MIT domain with the ATG14-ATG6 and via an unknown domain separately with the VPS34-VPS15 sub complexes, thereby assembling them into a functional PtdIns3K complex I [50]. This illustrates the general possibility to disintegrate the PtdIns3K complex I into sub complexes. This might also account for the observed exclusion of ATG14 from the PtdIns3K complex I in presence of

the phosphorylation mimicking NRBF2 5S-D variant. However, this dos not explain, why BECN1 remains part of the PtdIns3K complex. In addition to this, Ma et al. postulated, that mTORC1-mediated phosphorylation of NRBF2 at Ser113 and Ser120 shifts NRBF2 binding preferences from the autophagy inducing BECN1-ATG14 sub complex to the non-autophagy inducing PIK3C3-PIK3R4 sub complex [185]. To what extent this theory of mTORC1-dependent NRBF2 phosphorylation and subsequent inhibition of PtdIns3K complex activity is compatible with the here identified positive regulatory effect of ULK1-mediated NRBF2 phosphorylation remains to be clarified. It seems somehow contradictory that phosphorylation events at positions 113 and 120 inhibit PIK3C3 activity [185], while Ser101 in a spatial proximity is supposed to have opposed effects. The identified ULK1-dependent phosphorylation may only occur after the mTORC1-dependent phosphorylation has been removed, which merely accompanies the fact that ULK1 is inactive unless mTORC1 is suppressed. This theory might also be confirmed by repetition of the size exclusion chromatography experiments for autophagy-inducing conditions. Additionally, co-immunopurification experiments using the mutated NRBF2 variants should be performed to examine the potentially affected interaction capacity of the NRBF2 5S-D version. Therefore, both mutated NRBF2 versions (5S-A and 5S-D) harboring different epitope tags to facilitate immunopurification could be expressed in the same cell line. After subsequent immunopurifications, the specific interaction capacities could be assessed.

In addition, a further narrowing of the identified phospho-acceptor sites to their respective relevance and function, would minimize structural changes due to unnecessary mutations. In this context, it would be interesting to investigate whether Ser50 and Ser56 due to their higher correspondence to the ULK1 consensus sequence and their structural position at the C-terminal end of the MIT domain, may be primarily responsible for the observed effects on ATG14.

6.4 Conclusions and future perspectives

The initially stated goal of creating new approaches for a targeted therapeutic modulation of induced autophagy by identification of previously unknown interaction partners or areas in the autophagy signaling pathway was only partially achieved. Indeed, an influence of the NRBF2-ATG14 interaction depending on the phosphorylation status and thus the autophagic activity can be suspected. After further characterization, especially the interaction interfaces of NRBF2 and ATG14 can still prove to be potential therapeutic targets. In particular, the possibility of inhibiting this interaction should be further investigated. Depending on the effects such an inhibition may have on the additional transcriptional function of NRBF2, synergistic or antagonistic effects can be of consequence. Further investigations regarding the transcriptional effects of NRBF2 in a tissue-specific context or if applicable in samples from patients could open up new possibilities for clinical treatment. At present, tumor treatment by anti-cancer drugs in combination with inhibitors of autophagy is a promising option, while targeted modulation of specific transcriptional processes is difficult to achieve. Anyhow, the possibility of a broader and easier application of gene therapy in the near future, thanks to the rapid progress of the CRISPR/Cas9 system, should not be ignored. Accordingly and after validation of the observed transcriptional effects in a suitable cellular context, future studies will have to reveal whether the autophagy-regulatory or the transcription-regulatory function of NRBF2 can provide a clinically relevant target.

7 References

1. De Duve, C., Pressman, B. C., Gianetto, R., Wattiaux, R. & Appelmans, F. Tissue fractionation studies. *Biochem J* **60,** 604–617 (1955).
2. Deter, R. L., Baudhuin, P. & De Duve, C. Participation of lysosomes in cellular autophagy induced in rat liver by glucagon. *J. Cell Biol.* **35,** C11-6 (1967).
3. Tsukada, M. & Ohsumi, Y. Isolation and characterization of autophagy-defective mutants of Saccharomyces cerevisiae. *Fed. Eur. Biochem. Soc.* **333,** 169–174 (1993).
4. Choi, A. M. K., Ryter, S. W. & Levine, B. Autophagy in Human Health and Disease. *N. Engl. J. Med.* **368,** 651–662 (2013).
5. Cuervo, A. M. & Wong, E. Chaperone-mediated autophagy: roles in disease and aging. *Cell Res.* **24,** 92–104 (2014).
6. Li, W., Li, J. & Bao, J. Microautophagy: lesser-known self-eating. *Cell. Mol. Life Sci.* **69,** 1125–1136 (2012).
7. Feng, Y., He, D., Yao, Z. & Klionsky, D. J. The machinery of macroautophagy. *Cell Res.* **24,** 24–41 (2014).
8. Klionsky, D. J. *et al.* How shall i eat thee? *Autophagy* **3,** 413–416 (2007).
9. Singh, R. *et al.* Autophagy regulates lipid metabolism. *Nature* **458,** 1131–1135 (2009).
10. Suzuki, K. *et al.* The pre-autophagosomal structure organized by concerted functions of APG genes is essential for autophagosome formation. *EMBO J.* **20,** 5971–5981 (2001).
11. Hamasaki, M. *et al.* Autophagosomes form at ER-mitochondria contact sites. *Nature* **495,** 389–393 (2013).
12. Axe, E. L. *et al.* Autophagosome formation from membrane compartments enriched in phosphatidylinositol 3-phosphate and dynamically connected to the endoplasmic reticulum. *J. Cell Biol.* **182,** 685–701 (2008).
13. Tooze, S. A. & Yoshimori, T. The origin of the autophagosomal membrane. *Nat. Cell Biol.* **12,** 831–835 (2010).
14. Reggiori, F. & Ungermann, C. Autophagosome Maturation and Fusion. *J. Mol. Biol.* **429,** 486–496 (2017).
15. Yao, Z., Delorme-Axford, E., Backues, S. K. & Klionsky, D. J. Atg41/Icy2 regulates autophagosome formation. *Autophagy* **11,** 2288–2299 (2015).
16. Mizushima, N., Yoshimori, T. & Ohsumi, Y. The Role of Atg Proteins in Autophagosome Formation. *Annu. Rev. Cell Dev. Biol.* **27,** 107–32 (2011).
17. Suzuki, H., Kaizuka, T., Mizushima, N. & Noda, N. N. Structure of the Atg101 – Atg13 complex reveals essential roles of Atg101 in autophagy initiation. *Nat. Struct. Mol. Biol.* **22,** 572–80 (2015).
18. Wallot-Hieke, N. *et al.* Systematic analysis of ATG13 domain requirements for autophagy induction. *Autophagy* **14,** 743–763 (2018).
19. Alers, S., Löffler, A. S., Wesselborg, S. & Stork, B. The incredible ULKs. *Cell Commun. Signal.* **10,** 1–14 (2012).
20. Young, A. R. J. *et al.* Autophagy mediates the mitotic senescence transition. *Genes Dev.* **23,** 798–803 (2009).
21. Saxton, R. A. & Sabatini, D. M. mTOR Signaling in Growth, Metabolism, and Disease. *Cell* **168,** 960–976 (2017).
22. Hara, K. *et al.* Raptor, a Binding Partner of Target of Rapamycin (TOR), Mediates TOR Action. *Cell* **110,** 177–189 (2002).

23. Hosokawa, N. *et al.* Nutrient-dependent mTORC1 Association with the ULK1–Atg13–FIP200 Complex Required for Autophagy. *Mol. Biol. Cell* **20,** 327–331 (2009).
24. Jacinto, E. *et al.* Mammalian TOR complex 2 controls the actin cytoskeleton and is rapamycin insensitive. *Nat. Cell Biol.* **6,** 1122–1128 (2004).
25. Gwinn, D. M. *et al.* AMPK Phosphorylation of Raptor Mediates a Metabolic Checkpoint. *Mol. Cell* **30,** 214–226 (2008).
26. Inoki, K., Zhu, T. & Guan, K.-L. TSC2 mediates cellular energy response to control cell growth and survival. *Cell* **115,** 577–590 (2003).
27. Kim, J., Kundu, M., Viollet, B. & Guan, K. L. AMPK and mTOR regulate autophagy through direct phosphorylation of Ulk1. *Nat. Cell Biol.* **13,** 132–141 (2011).
28. Kim, J. H. J. *et al.* Differential regulation of distinct Vps34 complexes by AMPK in nutrient stress and autophagy. *Cell* **152,** 290–303 (2013).
29. Zhang, D. *et al.* AMPK regulates autophagy by phosphorylating BECN1 at threonine 388. *Autophagy* **12,** 1447–1459 (2016).
30. Brugarolas, J. *et al.* Regulation of mTOR function in response to hypoxia by REDD1 and the TSC1/TSC2 tumor suppressor complex. *Genes Dev.* **18,** 1–12 (2004).
31. Ma, L., Chen, Z., Erdjument-Bromage, H., Tempst, P. & Pandolfi, P. P. Phosphorylation and Functional Inactivation of TSC2 by Erk: Implications for Tuberous Sclerosis and Cancer Pathogenesis. *Cell* **121,** 179–193 (2005).
32. Cai, S. L. *et al.* Activity of TSC2 is inhibited by AKT-mediated phosphorylation and membrane partitioning. *J. Cell Biol.* **173,** 279–289 (2006).
33. Sancak, Y. *et al.* The Rag GTPases Bind Raptor and Mediate Amino Acid Signaling to mTORC1. *Science* **320,** 1496–1502 (2008).
34. Sabers, C. J. *et al.* Isolation of a Protein Target of the FKBP12-Rapamycin Complex in Mammalian Cells. *J. Biol. Chem.* **2,** 815–822 (1995).
35. Mizushima, N. The role of the Atg1/ULK1 complex in autophagy regulation. *Curr. Opin. Cell Biol.* **22,** 132–139 (2010).
36. Russell, R. C. *et al.* ULK1 induces autophagy by phosphorylating Beclin-1 and activating VPS34 lipid kinase. *Nat. Cell Biol.* **15,** 741–50 (2013).
37. Egan, D. F. *et al.* Small Molecule Inhibition of the Autophagy Kinase ULK1 and Identification of ULK1 Substrates. *Mol. Cell* **59,** 285–297 (2015).
38. Park, J. *et al.* The ULK1 complex mediates MTORC1 signaling to the autophagy initiation machinery via binding and phosphorylating ATG14. *Autophagy* **12,** 547–564 (2016).
39. Di Bartolomeo, S. *et al.* The dynamic interaction of AMBRA1 with the dynein motor complex regulates mammalian autophagy. *J. Cell Biol.* **191,** 155–168 (2010).
40. Zhou, C. *et al.* Regulation of mATG9 trafficking by Src- and ULK1- mediated phosphorylation in basal and starvation-induced autophagy. *Cell Res.* **27,** 184–201 (2017).
41. Lim, J. *et al.* Proteotoxic Stress Induces Phosphorylation of p62/SQSTM1 by ULK1 to Regulate Selective Autophagic Clearance of Protein Aggregates. *PLoS Genet.* **11,** 1–28 (2015).
42. Wu, W. *et al.* ULK 1 translocates to mitochondria and phosphorylates FUNDC1 to regulate mitophagy. *EMBO Rep.* **15,** 566–575 (2014).
43. Dunlop, E. A., Hunt, D. K., Acosta-Jaquez, H. A., Fingar, D. C. & Tee, A. R. ULK1 inhibits mTORC1 signaling, promotes multisite Raptor phosphorylation and hinders substrate binding. *Autophagy* **7,** 737–747 (2011).

44. Kraft, C. *et al.* Binding of the Atg1/ULK1 kinase to the ubiquitin-like protein Atg8 regulates autophagy. *EMBO J.* **31,** 3691–3703 (2012).
45. Alemu, E. A. *et al.* ATG8 family proteins act as scaffolds for assembly of the ULK complex: Sequence requirements for LC3-interacting region (LIR) motifs. *J. Biol. Chem.* **287,** 39275–39290 (2012).
46. Joachim, J. *et al.* Activation of ULK Kinase and Autophagy by GABARAP Trafficking from the Centrosome Is Regulated by WAC and GM130. *Mol. Cell* **60,** 899–913 (2015).
47. Herman, P. K. & Emr, S. D. Characterization of VPS34, a gene required for vacuolar protein sorting and vacuole segregation in Saccharomyces cerevisiae. *Mol. Cell. Biol.* **10,** 6742–54 (1990).
48. Panaretou, C., Domin, J., Cockcroft, S. & Waterfield, M. D. Characterization of p150, an Adaptor Protein for the Human Phosphatidylinositol (PtdIns) 3-Kinase. *J. Biol. Chem.* **272,** 2477–2485 (1997).
49. Itakura, E., Kishi, C., Inoue, K. & Mizushima, N. Beclin 1 Forms Two Distinct Phosphatidylinositol 3-Kinase Complexes with Mammalian Atg14 and UVRAG. *Mol. Biol. Cell* **19,** 5360–5372 (2008).
50. Araki, Y. *et al.* Atg38 is required for autophagy-specific phosphatidylinositol 3-kinase complex integrity. *J. Cell Biol.* **203,** 299–313 (2013).
51. Ohashi, Y. *et al.* Characterization of Atg38 and NRBF2, a fifth subunit of the autophagic Vps34/PIK3C3 complex. *Autophagy* **12,** 2129–2144 (2016).
52. Young, L. N., Cho, K., Lawrence, R., Zoncu, R. & Hurley, J. H. Dynamics and architecture of the NRBF2-containing phosphatidylinositol 3-kinase complex I of autophagy. *Proc. Natl. Acad. Sci.* **1,** 201603650 (2016).
53. Cao, Y. *et al.* NRBF2 regulates macroautophagy as a component of Vps34 Complex I. *Biochem. J.* **461,** 315–22 (2014).
54. Lu, J. *et al.* NRBF2 regulates autophagy and prevents liver injury by modulating Atg14L-linked phosphatidylinositol-3 kinase III activity. *Nat. Commun.* **5,** (2014).
55. Zhong, Y. *et al.* Nrbf2 Protein Suppresses Autophagy by Modulating Atg14L Protein-containing Beclin 1-Vps34 Complex Architecture and Reducing Intracellular Phosphatidylinositol-3 Phosphate Levels. *J. Biol. Chem.* **289,** 26021–26037 (2014).
56. Christoforidis, S. *et al.* Phosphatidylinositol-3-OH kinases are Rab5 effectors. *Nat. Cell Biol.* **1,** 249–52 (1999).
57. Sun, Q. *et al.* Identification of Barkor as a mammalian autophagy-specific factor for Beclin 1 and class III phosphatidylinositol 3-kinase. *Proc. Natl. Acad. Sci.* **105,** 19211–19216 (2008).
58. Liang, C. *et al.* Beclin1-binding UVRAG targets the class C Vps complex to coordinate autophagosome maturation and endocytic trafficking. *Nat. Cell Biol.* **10,** (2008).
59. Liang, X. H. *et al.* Protection against Fatal Sindbis Virus Encephalitis by Beclin , a Novel Bcl-2-Interacting Protein. *J. Virol.* **72,** 8586–8596 (1998).
60. Decuypere, J.-P., Parys, J. B. & Bultynck, G. Regulation of the Autophagic Bcl-2/Beclin 1 Interaction. *Cells* **1,** 284–312 (2012).
61. Wei, Y., Pattingre, S., Sinha, S., Bassik, M. & Levine, B. JNK1-Mediated Phosphorylation of Bcl-2 Regulates Starvation-Induced Autophagy. *Mol. Cell* **30,** 678–688 (2008).
62. Zalckvar, E. *et al.* DAP-kinase-mediated phosphorylation on the BH3 domain of beclin 1 promotes dissociation of beclin 1 from Bcl-XL and induction of autophagy. *EMBO*

Rep. **10,** 285–292 (2009).
63. Wei, Y., Sinha, S. & Levine, B. Dual Role of JNK1-Mediated Phosphorylation of Bcl-2 in Autophagy and Apoptosis Regulation. *Autophagy* **4,** 949–951 (2008).
64. Wirawan, E. *et al.* Caspase-mediated cleavage of Beclin-1 inactivates Beclin-1-induced autophagy and enhances apoptosis by promoting the release of proapoptotic factors from mitochondria. *Cell Death Dis.* **1,** (2010).
65. Matsuzawa, Y. *et al.* RIPK3 regulates p62–LC3 complex formation via the caspase-8-dependent cleavage of p62. *Biochem. Biophys. Res. Commun.* **456,** 298–304 (2015).
66. Oral, O. *et al.* Cleavage of Atg3 protein by caspase-8 regulates autophagy during receptor-activated cell death. *Apoptosis* **17,** 810–820 (2012).
67. Han, J. *et al.* A complex between Atg7 and caspase-9: A novel mechanism of cross-regulation between autophagy and apoptosis. *J. Biol. Chem.* **289,** 6485–6497 (2014).
68. Wang, R. C. *et al.* Akt-Mediated Regulation of Autophagy and Tumorigenesis Through Beclin 1 Phosphorylation. *Science* **338,** 956–959 (2012).
69. Wei, Y. *et al.* EGFR-Mediated Phosphorylation of Beclin 1 in Autophagy Suppression, Tumor Progression and Tumor Chemoresistance. *Cell* **154,** 1269–1284 (2013).
70. Wei, Y. *et al.* The stress-responsive kinases MAPKAPK2/MAPKAPK3 activate starvation-induced autophagy through Beclin 1 phosphorylation. *Elife* **4,** 1–25 (2015).
71. Polson, H. E. J. *et al.* Mammalian Atg18 (WIPI2) localizes to omegasome-anchored phagophores and positively regulates LC3 lipidation. *Autophagy* **6,** 506–522 (2010).
72. Velikkakath, A. K. G., Nishimura, T., Oita, E., Ishihara, N. & Mizushima, N. Mammalian Atg2 proteins are essential for autophagosome formation and important for regulation of size and distribution of lipid droplets. *Mol. Biol. Cell* **23,** (2012).
73. Orsi, A. *et al.* Dynamic and transient interactions of Atg9 with autophagosomes, but not membrane integration, are required for autophagy. *Mol. Biol. Cell* **23,** (2012).
74. Young, A. R. J. *et al.* Starvation and ULK1-dependent cycling of mammalian Atg9 between the TGN and endosomes. *J. Cell Sci.* **119,** 3888–3900 (2006).
75. Geng, J. & Klionsky, D. J. The Atg8 and Atg12 ubiquitin-like conjugation systems in macroautophagy. *EMBO Rep.* **9,** 859–864 (2008).
76. Weidberg, H. *et al.* Membrane Fusion LC3 and GATE-16 N Termini Mediate Membrane Fusion Processes Required for Autophagosome Biogenesis. *Dev. Cell* **20,** 444–454 (2011).
77. Weidberg, H. *et al.* LC3 and GATE-16/GABARAP subfamilies are both essential yet act differently in autophagosome biogenesis. *EMBO J.* **29,** 1792–1802 (2010).
78. Bjørkøy, G. *et al.* p62/SQSTM1 forms protein aggregates degraded by autophagy and has a protective effect on huntingtin-induced cell death. *J. Cell Biol.* **171,** 603–614 (2005).
79. Kirkin, V., Lamark, T., Johansen, T. & Dikic, I. NBR1 cooperates with p62 in selective autophagy of ubiquitinated targets. *Autophagy* **5,** 732–733 (2009).
80. Liu, Z. *et al.* Article Ubiquitylation of Autophagy Receptor Optineurin by HACE1 Activates Selective Autophagy for Tumor Suppression. *Cancer Cell* **26,** 106–120 (2014).
81. Monastyrska, I., Rieter, E., Klionsky, D. J. & Reggiori, F. Multiple roles of the cytoskeleton in autophagy. *Biol. Rev.* **84,** 431–448 (2009).
82. Itakura, E., Kishi-Itakura, C. & Mizushima, N. The hairpin-type tail-anchored SNARE syntaxin 17 targets to autophagosomes for fusion with endosomes/lysosomes. *Cell*

151, 1256–1269 (2012).
83. Nair, U. & Klionsky, D. J. Activation of autophagy is required for muscle homeostasis during physical exercise. *Autophagy* **7,** 1405–1406 (2011).
84. Hansen, M., Rubinsztein, D. C. & Walker, D. W. Autophagy as a promoter of longevity: insights from model organisms. *Nat. Rev. Mol. Cell Biol.* 1–15 (2018).
85. Ciechanover, A. & Kwon, Y. T. Degradation of misfolded proteins in neurodegenerative diseases: therapeutic targets and strategies. *Exp. Mol. Med.* **47,** e147 (2015).
86. Dikic, I. Proteasomal and Autophagic Degradation Systems. *Annu. Rev. Biochem.* **86,** 193–224 (2017).
87. Lin, M. T. & Beal, M. F. Mitochondrial dysfunction and oxidative stress in neurodegenerative diseases. *Nature* **443,** 787–795 (2006).
88. Dehay, B. *et al.* Pathogenic Lysosomal Depletion in Parkinson's Disease. *J. Neurosci.* **30,** 12535–12544 (2010).
89. Won, J., Im, Y., Kim, J., Singh, A. K. & Singh, I. Involvement of AMP-activated-protein-kinase (AMPK) in neuronal amyloidogenesis. *Biochem. Biophys. Res. Commun.* **399,** 487–491 (2010).
90. Aita, V. M. *et al.* Cloning and genomic organization of Beclin 1, a candidate tumor suppressor gene on chromosome 17q21. *Genomics* **59,** 59–65 (1999).
91. Mizushima, N., Levine, B., Cuervo, A. M. & Klionsky, D. J. Autophagy fights disease through cellular self-digestion. *Nature* **451,** 1069–1075 (2008).
92. Liang, X. H. *et al.* Induction of autophagy and inhibition of tumorigenesis by beclin 1. *Nature* **402,** 1–5 (1999).
93. Apel, A., Herr, I., Schwarz, H., Rodemann, H. P. & Mayer, A. Blocked autophagy sensitizes resistant carcinoma cells to radiation therapy. *Cancer Res.* **68,** 1485–1494 (2008).
94. Guo, J. Y. *et al.* Activated Ras requires autophagy to maintain oxidative metabolism and tumorigenesis. *Genes Dev.* **25,** 460–470 (2011).
95. Zou, Z. *et al.* Aurora kinase A inhibition-induced autophagy triggers drug resistance in breast cancer cells. *Autophagy* **8,** 1798–1810 (2012).
96. Onorati, A. V, Dyczynski, M., Ojha, R. & Amaravadi, R. K. Targeting Autophagy in Cancer. *Cancer* 1–12 (2018).
97. Rosenfeldt, M. T. *et al.* p53 status determines the role of autophagy in pancreatic tumour development. *Nature* **504,** 296–300 (2013).
98. Papandreou, M. & Tavernarakis, N. Autophagy and the endo/exosomal pathways in health and disease. *Biotechnol. J.* **11,** 1–9 (2016).
99. Ruivo, C. F., Adem, B., Silva, M. & Melo, S. A. The Biology of Cancer Exosomes: Insights and New Perspectives. *Cancer Res.* **77,** 6480–6488 (2017).
100. Catalano, M. *et al.* Autophagy induction impairs migration and invasion by reversing EMT in glioblastoma cells. *Mol. Oncol.* **9,** 1612–1625 (2015).
101. Sharifi, M. N. *et al.* Autophagy promotes focal adhesion disassembly and cell motility of metastatic tumor cells through the direct interaction of paxillin with LC3. *Cell Rep.* **15,** 1660–1672 (2016).
102. Yoshida, T., Tsujioka, M., Honda, S., Tanaka, M. & Shimizu, S. Autophagy suppresses cell migration by degrading GEF-H1, a RhoA GEF. *Oncotarget* **7,** 34420–34429 (2016).
103. Sundelin, S. P. & Terman, A. Different effects of chloroquine and hydroxychloroquine on lysosomal function in cultured retinal pigment epithelial cells. *APMIS* **110,** 481–

489 (2002).
104. Deretic, V. Autophagy in immunity and cell-autonomous defense against intracellular microbes. *Immunol. Rev.* **240,** 92–104 (2011).
105. Münz, C. Antigen processing via autophagy — not only for MHC class II presentation anymore? *Curr. Opin. Immunol.* **22,** 89–93 (2010).
106. Rockel, J. S. & Kapoor, M. Autophagy: controlling cell fate in rheumatic diseases. *Nat. Rev. Rheumatol.* **12,** 517–531 (2016).
107. Zheng, Y. T. *et al.* The Adaptor Protein p62/SQSTM1 Targets Invading Bacteria to the Autophagy Pathway. *J. Immunol.* **183,** 5909–5916 (2009).
108. Ogawa, M. *et al.* Escape of Intracellular Shigella from Autophagy. *Science* **307,** (2005).
109. Schnaith, A. *et al.* Staphylococcus aureus Subvert Autophagy for Induction of Caspase-independent Host Cell Death. *J. Biol. Chem.* **282,** 2695–2706 (2007).
110. Parihar, S. P. *et al.* Statin Therapy Reduces the Mycobacterium tuberculosis Burden in Human Macrophages and in Mice by Enhancing Autophagy and Phagosome Maturation. *J. Infect. Dis.* **209,** 754–763 (2014).
111. Kirisako, T. *et al.* Formation Process of Autophagosome Is Traced with Apg8/Aut7p in Yeast. *J. Cell Biol.* **147,** 435–446 (1999).
112. Füllgrabe, J., Ghislat, G., Cho, D.-H. & Rubinsztein, D. C. Transcriptional regulation of mammalian autophagy at a glance. *J. Cell Sci.* **129,** 3059–3066 (2016).
113. Settembre, C. *et al.* TFEB Links Autophagy to Lysosomal Biogenesis. *Science* **332,** 1429–1433 (2013).
114. Martina, J. A., Chen, Y., Gucek, M. & Puertollano, R. MTORC1 functions as a transcriptional regulator of autophagy by preventing nuclear transport of TFEB. *Autophagy* **8,** 903–914 (2012).
115. Chauhan, S. *et al.* ZKSCAN3 Is a Master Transcriptional Repressor of Autophagy. *Mol. Cell* **50,** 16–28 (2013).
116. Tsunemi, T. *et al.* PGC-1α Rescues Huntington' s Disease Proteotoxicity by Preventing Oxidative Stress and Promoting TFEB Function. *Sci. Transl. Med.* **4,** (2012).
117. Bowman, C. J., Ayer, D. E. & Dynlacht, B. D. Foxk proteins repress the initiation of starvation-induced atrophy and autophagy programs. *Nat. Cell Biol.* **16,** 1202–1214 (2014).
118. Zhao, J. *et al.* FoxO3 Coordinately Activates Protein Degradation by the Autophagic/Lysosomal and Proteasomal Pathways in Atrophying Muscle Cells. *Cell Metab.* **6,** 472–483 (2007).
119. Zhao, Y. *et al.* Cytosolic FoxO1 is essential for the induction of autophagy and tumour suppressor activity. *Nat. Cell Biol.* **12,** (2010).
120. Polager, S., Ofir, M. & Ginsberg, D. E2F1 regulates autophagy and the transcription of autophagy genes. *Oncogene* **27,** 4860–4864 (2008).
121. Shaw, J. *et al.* Antagonism of E2F-1 regulated Bnip3 transcription by NF-κB is essential for basal cell survival. *Proc. Natl. Acad. Sci.* **105,** 20734–20739 (2008).
122. Jiang, Q. *et al.* Heat shock protein 90-mediated inactivation of nuclear factor-κB switches autophagy to apoptosis through becn1 transcriptional inhibition in selenite-induced NB4 cells. *Mol. Biol. Cell* **22,** 1167–1180 (2011).
123. Zhang, J. & Ney, P. a. Role of BNIP3 and NIX in cell death, autophagy, and mitophagy. *Cell Death Differ.* **16,** 939–946 (2009).
124. Guo, K. *et al.* Hypoxia induces the expression of the pro-aptotic gene BNIP3. *Cell*

Death Differ **8,** 367–376 (2001).
125. Raingeaud, J. *et al.* Pro-inflammatory Cytokines and Environmental Stress Cause p38 Mitogen-activated Protein Kinase Activation by Dual Phosphorylation on Tyrosine and Threonine. *J. Biol. Chem.* **13,** 7420–7426 (1995).
126. Jia, G., Cheng, G., Gangahar, D. M. & Agrawal, D. K. Insulin-like growth factor-1 and TNF-α regulate autophagy through c-jun N-terminal kinase and Akt pathways in human atherosclerotic vascular smooth cells. *Immunol. Cell Biol.* **84,** 448–454 (2006).
127. Kenzelmann Broz, D. *et al.* Global genomic profiling reveals an extensive p53-regulated autophagy program contributing to key p53 responses. *Genes Dev.* **27,** 1016–1031 (2013).
128. Seok, S. *et al.* Transcriptional regulation of autophagy by an FXR-CREB axis. *Nature* **516,** 108–11 (2014).
129. Lee, J. M. *et al.* Nutrient-sensing nuclear receptors coordinate autophagy. *Nature* **516,** 112–115 (2014).
130. Ghosh, A. *et al.* Activation of peroxisome proliferator-activated receptor α induces lysosomal biogenesis in brain cells: Implications for lysosomal storage disorders. *J. Biol. Chem.* **290,** 10309–10324 (2015).
131. Yan, S., Yang, X., Chen, T., Xi, Z. & Jiang, X. The PPARγ agonist Troglitazone induces autophagy, apoptosis and necroptosis in bladder cancer cells. *Cancer Gene Ther.* **21,** 188–193 (2014).
132. Qin, H. *et al.* 15d-Prostaglandin J2 Protects Cortical Neurons Against Oxygen–Glucose Deprivation/Reoxygenation Injury: Involvement of Inhibiting Autophagy Through Upregulation of Bcl-2. *Cell Mol Neurobiol* **35,** 303–312 (2014).
133. Bensinger, S. J. & Tontonoz, P. Integration of metabolism and inflammation by lipid-activated nuclear receptors. *Nature* **454,** 470–477 (2008).
134. Glass, C. K. & Ogawa, S. Combinatorial roles of nuclear receptors in inflammation and immunity. *Nat. Rev. Immunol.* **6,** 44–55 (2006).
135. Daynes, R. A. & Jones, D. C. Emerging roles of PPARs in inflammation and immunity. *Nat. Rev. Immunol.* **2,** 748–759 (2002).
136. Shi, Y., Hon, M. & Evans, R. M. The peroxisome proliferator-activated receptor δ, an integrator of transcriptional repression and nuclear receptor signaling. *Proc. Natl. Acad. Sci.* **99,** 2613–2618 (2002).
137. Braissant, O. & Wahli, W. Differential Expression of Peroxisome Proliferator-Activated Receptor-α, -β and -γ during Rat Embryonic Development. *Endocrinology* **139,** 2748–2754 (1998).
138. Kersten, S. *et al.* Peroxisome proliferator–activated receptor α mediates the adaptive response to fasting. *J. Clin. Invest.* **103,** 1489–1498 (1999).
139. Chinetti, G. *et al.* Activation of Proliferator-activated Receptors α and γ Induces Apoptosis of Human Monocyte-derived Macrophages. *J. Biol. Chem.* **273,** 25573–25580 (1998).
140. Tordjman, K. *et al.* PPARα deficiency reduces insulin resistance and atherosclerosis in apoE-null mice. *J. Clin. Invest.* **107,** 1025–1034 (2001).
141. Peters, J. M. *et al.* Growth, Adipose, Brain, and Skin Alterations Resulting from Targeted Disruption of the Mouse Peroxisome Proliferator-Activated Receptor β(δ). *Mol. Cell. Biol.* **20,** 5119–5128 (2000).
142. Pan, D., Fujimoto, M., Lopes, A. & Wang, Y. Twist-1 Is a PPARδ-Inducible, Negative-Feedback Regulator of PGC-1α in Brown Fat Metabolism. *Cell* **137,** 73–86 (2009).

143. Wang, Y. *et al.* Regulation of Muscle Fiber Type and Running Endurance by PPARδ. *PLoS Biol.* **2,** 1532–1539 (2004).
144. Lee, C. *et al.* Transcriptional Repression of Atherogenic Inflammation: Modulation by PPARδ. *Science* **302,** 453–457 (2003).
145. Tontonoz, P., Hu, E., Graves, R. A., Budavari, A. I. & Spiegelman, B. M. mPPARγ2: tissue-specific regulator of an adipocyte enhancer. *Genes Dev.* **8,** 1224–1234 (1994).
146. Semple, R. K., Chatterjee, V. K. K. & O'Rahilly, S. PPARγ and human metabolic disease. *J. Clin. Invet.* **116,** 581–589 (2006).
147. Marfella, R. *et al.* Myocardial lipid accumulation in patients with pressure-overloaded heart and metabolic syndrome. *J. Lipid Res.* **50,** 2314–2323 (2009).
148. Chung, S. W. *et al.* Oxidized Low Density Lipoprotein Inhibits Interleukin-12 Production in Lipopolysaccharide-activated Mouse Macrophages via Direct Interactions between Peroxisome Proliferator-activated Receptor-γ and Nuclear Factor-κB. *J. Biol. Chem.* **275,** 32681–32687 (2000).
149. Sanger, F., Nicklen, S. & Coulson, A. R. DNA sequencing with chain-terminating inhibitors. *Proc. Natl. Acad. Sci.* **74,** 5463–5467 (1977).
150. Saiki, R. K. *et al.* Enzymatic Amplification of β-Globin Genomic Sequences and Restriction Site Analysis for Diagnosis of Sickle Cell Anemia. *Science* **230,** 1350–1354 (1985).
151. Mullis, K. *et al.* Specific Enzymatic Amplification of DNA In Vitro: The Polymerase Chain Reaction. *Cold Spring Harb Symp Quant Biol* **51,** 263–73 (1986).
152. Li, M. Z. & Elledge, S. J. Harnessing homologous recombination in vitro to generate recombinant DNA via SLIC. *Nat. Methods* **4,** 251–256 (2007).
153. Graham, F. L., Smiley, J., Russell, W. C. & Nairn, R. Characteristics of a Human Cell Line Transformed by DNA from Human Adenovirus Type 5. *J. Gen. Virol.* **36,** 59–74 (1977).
154. Ben-Bassat, H. *et al.* Establishment in continuous culture of a new type of lymphocyte from a 'Burkitt like' malignant lymphoma (line D.G.-75). *Int. J. Cancer* **19,** 27–33 (1977).
155. Baba, T. W. & Humphries, E. H. Differential response to avian leukosis virus infection exhibited by two chicken lines. *Virology* **135,** 181–188 (1984).
156. Buerstedde, J.-M. *et al.* Light chain gene conversion continues at high rate in an ALV-induced cell line. *EMBO J.* **9,** 921–927 (1990).
157. Buerstedde, J. M. & Takeda, S. Increased ratio of targeted to random integration after transfection of chicken B cell lines. *Cell* **67,** 179–188 (1991).
158. Wu, J. C., Merlinot, G. & Fausto, N. Establishment and characterization of differentiated, nontransformed hepatocyte cell lines derived from mice transgenic for transforming growth factor α. *Proc. Natl. Acad. Sci.* **91,** 674–678 (1994).
159. Cheong, H., Lindsten, T., Wu, J., Lu, C. & Thompson, C. B. Ammonia-induced autophagy is independent of ULK1/ULK2 kinases. *Proc. Natl. Acad. Sci.* **108,** 17856–17856 (2011).
160. Morita, S., Kojima, T. & Kitamura, T. Plat-E: an efficient and stable system for transient packaging of retroviruses. *Gene Ther.* **7,** 1063–1066 (2000).
161. Schindelin, J. *et al.* Fiji: an open-source platform for biological-image analysis. *Nat. Methods* **9,** 676–682 (2012).
162. Bradford, M. M. A rapid and sensitive method for the quantitation of microgram quantities of protein utilizing the principle of protein dye-binding. *Anal. Biochem.* **72,**

248–254 (1976).
163. Weber, K. & Osborn, M. The Reliability of Molecular Weight Determinations by Dodecyl Sulfate-Polyacrylamide Gel Electrophoresis. *J. Biol. Chem.* **244,** 4406–4412 (1969).
164. Laemmli, U. K. Cleavage of Structural Proteins during the Assembly of the Head of Bacteriophage T4. *Nature* **227,** (1970).
165. Cox, J. & Mann, M. MaxQuant enables high peptide identification rates, individualized p.p.b.-range mass accuracies and proteome-wide protein quantification. *Nat. Biotechnol.* **26,** 1367–1372 (2008).
166. Yeung, Y.-G. & Stanley, E. R. Rapid Detergent Removal from Peptide Samples with Ethyl Acetate for Mass Spectrometry Analysis. in *Current Protocols in Protein Science* 1–5 (2010).
167. Bolstad, B. M., Irizarry, R. A., Astrand, M. & Speed, T. P. A Comparison of Normalization Methods for High Density Oligonucleotide Array Data Based on Variance and Bias. *Bioinformatics* **19,** (2003).
168. Huang, D. W., Sherman, B. T. & Lempicki, R. A. Systematic and integrative analysis of large gene lists using DAVID bioinformatics resources. *Nat. Protoc.* **4,** 44–57 (2009).
169. Jordan, J. D., Landau, E. M. & Iyengar, R. Signaling networks: the origins review of cellular multitasking. *Cell* **103,** 193–200 (2000).
170. Behrends, C., Sowa, M. E., Gygi, S. P. & Harper, J. W. Network organization of the human autophagy system. *Nature* **466,** 68–76 (2010).
171. Rosenquist, M., Sehnke, P., Ferl, R. J., Sommarin, M. & Larsson, C. Evolution of the 14-3-3 protein family: Does the large number of isoforms in multicellular organisms reflect functional specificity? *J. Mol. Evol.* **51,** 446–458 (2000).
172. Zhang, J., Zheng, N. & Zhou, P. Exploring the functional complexity of cellular proteins by protein knockout. *Proc. Natl. Acad. Sci.* **100,** 14127–14132 (2003).
173. Klionsky, D. J. *et al.* Guidelines for the use and interpretation of assays for monitoring autophagy (3rd edition). *Autophagy* **12,** 1–222 (2016).
174. Rubinsztein, D. C. *et al.* In search of an "autophagomometer". *Autophagy* **5,** 585–589 (2009).
175. Yasumo, H. *et al.* Nuclear receptor binding factor-2 (NRBF-2), a possible gene activator protein interacting with nuclear hormone receptors. *Biochim. Biophys. Acta* **1490,** 189–197 (2000).
176. Flores, A. M., Li, L. & Aneskievich, B. J. Isolation and functional analysis of a keratinocyte-derived, ligand-regulated nuclear receptor comodulator. *J. Invest. Dermatol.* **123,** 1092–1101 (2004).
177. Palomer, X. *et al.* PPARβ/δ attenuates palmitate-induced endoplasmic reticulum stress and induces autophagic markers in human cardiac cells. *Int. J. Cardiol.* **174,** 110–118 (2014).
178. Li, B.-H. *et al.* Telmisartan-induced PPARγ activity attenuates lipid accumulation in VSMCs via induction of autophagy. *Mol. Biol. Rep.* **42,** 179–186 (2015).
179. Lambert, M., Jambon, S., Depauw, S. & David-Cordonnier, M.-H. Targeting Transcription Factors for Cancer Treatment. *Molecules* **23,** 1479 (2018).
180. Mattaj, I. W. & Englmeier, L. Nucleoplasmic Transport: The Soluble Phase. *Annu. Rev. Biochem.* **67,** 265–306 (1998).
181. Heid, C., Livak, K., Stevens, J. & Williams, P. Real time quantitative PCR. *Genome Res.* **6,** 986–994 (1996).

182. Pfaffl, M. W. A new mathematical model for relative quantification in real-time RT–PCR. *Nucleic Acids Res.* **29,** 16–21 (2001).
183. Wang, Y. C., Peterson, S. E. & Loring, J. F. Protein post-translational modifications and regulation of pluripotency in human stem cells. *Cell Res.* **24,** 143–160 (2014).
184. Khoury, G. A., Baliban, R. C. & Floudas, C. A. Proteome-wide post-translational modification statistics: Frequency analysis and curation of the swiss-prot database. *Sci. Rep.* **1,** (2011).
185. Ma, X. *et al.* MTORC1-mediated NRBF2 phosphorylation functions as a switch for the class III PtdIns3K and autophagy. *Autophagy* **13,** 592–607 (2017).
186. Wesselborg, S. & Stork, B. Autophagy signal transduction by ATG proteins: from hierarchies to networks. *Cell. Mol. Life Sci.* **72,** 4721–4757 (2015).
187. Petherick, K. J. *et al.* Pharmacological Inhibition of ULK1 Kinase Blocks Mammalian Target of Rapamycin (mTOR)-dependent Autophagy. *J. Biol. Chem.* **290,** 11376–11383 (2015).
188. Zhou, H. *et al.* Towards a comprehensive characterization of a human cancer cell phosphoproteome. *J. Proteome Res.* **12,** 260–71 (2012).
189. Daub, H. *et al.* Kinase-Selective Enrichment Enables Quantitative Phosphoproteomics of the Kinome across the Cell Cycle. *Mol. Cell* **31,** 438–448 (2008).
190. Oppermann, F. S. *et al.* Large-scale Proteomics Analysis of the Human Kinome. *Mol. Cell. Proteomics* **8,** 1751–1764 (2009).
191. Blaydes, J. P., Vojtesek, B., Bloomberg, G. B. & Hupp, T. R. The Development and Use of Phospho-Specific Antibodies to Study Protein Phosphorylation. in *Methods in Molecular Biology* **99,** 177–189 (2000).
192. Fredriksson, S. *et al.* Protein detection using proximity-dependent DNA ligation assays. *Nat. Biotechnol.* **20,** 473–477 (2002).
193. Pozuelo-Rubio, M. Regulation of autophagic activity by 14-3-3ζ proteins associated with class III phosphatidylinositol-3-kinase. *Cell Death Differ.* **18,** 479–492 (2011).
194. Lee, J. W., Park, S., Takahashi, Y. & Wang, H. The Association of AMPK with ULK1 Regulates Autophagy. *PLoS One* **5,** 1–9 (2010).
195. Wang, B., Ling, S. & Lin, W. 14-3-3τ Regulates Beclin 1 and Is Required for Autophagy. *PLoS One* **5,** (2010).
196. Kidd, M. E., Shumaker, D. K. & Ridge, K. M. The role of Vimentin intermediate filaments in the progression of lung cancer. *Am. J. Respir. Cell Mol. Biol.* **50,** 1–6 (2014).
197. Zhong, J. *et al.* Inhibition of CLIC4 Enhances Autophagy and Triggers Mitochondrial and ER Stress-Induced Apoptosis in Human Glioma U251 Cells under Starvation. *PLoS One* **7,** 1–10 (2012).
198. Liu, Q. *et al.* Discovery of 9-(6-Aminopyridin-3-yl)-1-(3-(trifluoromethyl)-phenyl)benzo[h][1,6]naphthyridin-2(1H)-one (Torin2) as a Potent, Selective, and Orally Available Mammalian Target of Rapamycin (mTOR) Inhibitor for Treatment of Cancer. *J. Med. Chem.* **54,** 1473–1480 (2011).
199. Mei, Y., Wang, Y., Chen, H., Sun, Z. S. & Ju, X. Recent progress in CRISPR/Cas9 technology. *J. Genet. Genomics* **2016,** (2016).
200. Joshi, A. *et al.* Nuclear ULK1 promotes cell death in response to oxidative stress through PARP1. *Cell Death Differ.* **23,** 1–15 (2015).
201. Kosugi, S., Hasebe, M., Tomita, M. & Yanagawa, H. Systematic identification of cell

cycle-dependent yeast nucleocytoplasmic shuttling proteins by prediction of composite motifs. *Proc. Natl. Acad. Sci.* **106,** 10171–10176 (2009).
202. Park, J. *et al.* RAS–MAPK–MSK1 pathway modulates ataxin 1 protein levels and toxicity in SCA1. *Nature* **498,** 325–331 (2013).
203. Schmeisser, H. *et al.* Type I interferons induce autophagy in certain human cancer cell lines. *Autophagy* **9,** 683–696 (2013).
204. Harris, J. Autophagy and cytokines. *Cytokine* **56,** 140–144 (2011).
205. Zhang, H. & McCarty, N. Tampering with cancer chemoresistance by targeting the TGM2-IL6-autophagy regulatory network. *Autophagy* **13,** 627–628 (2017).
206. Saitoh, T. *et al.* Loss of the autophagy protein Atg16L1 enhances endotoxin-induced IL-1β production. *Nature* **456,** 264–269 (2008).
207. Nakahira, K. *et al.* Autophagy proteins regulate innate immune responses by inhibiting the release of mitochondrial DNA mediated by the NALP3 inflammasome. *Nat. Immunol.* **8,** 222–30 (2011).
208. Rey-Jurado, E., Riedel, C. A., González, P. A., Bueno, S. M. & Kalergis, A. M. Contribution of autophagy to antiviral immunity. *FEBS Lett.* **589,** 3461–3470 (2015).
209. Darnell, J. E. J., Kerr, I. M. & Stark, G. R. Jak-STAT Pathways and Transcriptional Activation to IFNs Response and Other Transcriptional Activation in Extracellular Signaling Proteins. *Science* **264,** 1415–1421 (1994).
210. Smith, J. J. & Aitchison, J. D. Peroxisomes take shape. *Nat. Rev. Mol. Cell Biol.* **14,** 803–817 (2013).
211. Zhang, J. *et al.* A tuberous sclerosis complex signalling node at the peroxisome regulates mTORC1 and autophagy in response to ROS. *Nat. Cell Biol.* **15,** 1186–1196 (2013).
212. Wanders, R. J. A., Waterham, H. R. & Ferdinandusse, S. Metabolic Interplay between Peroxisomes and Other Subcellular Organelles Including Mitochondria and the Endoplasmic Reticulum. *Front. Cell Dev. Biol.* **3,** 1–15 (2016).
213. Pawlak, M., Lefebvre, P. & Staels, B. Molecular mechanism of PPARα action and its impact on lipid metabolism, inflammation and fibrosis in non-alcoholic fatty liver disease. *J. Hepatol.* **62,** 720–733 (2015).
214. Anding, A. L. & Baehrecke, E. H. Cleaning House: Selective Autophagy of Organelles. *Dev. Cell* **41,** 10–22 (2017).
215. Sargent, G. *et al.* PEX2 is the E3 ubiquitin ligase required for pexophagy during starvation. *J. Cell Biol.* **214,** 677–690 (2016).
216. Jiang, L., Hara-Kuge, S., Yamashita, S. I. & Fujiki, Y. Peroxin Pex14p is the key component for coordinated autophagic degradation of mammalian peroxisomes by direct binding to LC3-II. *Genes to Cells* **20,** 36–49 (2015).
217. Green, S. & Wahli, W. Peroxisome proliferator-activated receptors: finding the orphan a home. *Mol. Cell. Endocrinol.* **100,** 149–153 (1994).
218. El-Brolosy, M. A. & Stainier, D. Y. R. Genetic compensation: A phenomenon in search of mechanisms. *PLoS Genet.* **13,** 1–17 (2017).
219. Wang, Z., Gerstein, M. & Snyder, M. RNA-Seq: a revolutionary tool for transcriptomics. *Nat. Rev. Genet.* **10,** (2009).
220. Park, C. W. *et al.* BNIP3 is degraded by ULK1-dependent autophagy via MTORC1 and AMPK. *Autophagy* **9,** 345–360 (2013).
221. Djavaheri-Mergny, M. *et al.* NF-κB activation represses tumor necrosis factor-α-induced autophagy. *J. Biol. Chem.* **281,** 30373–30382 (2006).

222. Kajimura, S., Spiegelman, B. M. & Seale, P. Brown and beige fat: Physiological roles beyond heat generation. *Cell Metab.* **22,** 546–559 (2015).
223. Altshuler-Keylin, S. *et al.* Beige Adipocyte Maintenance Is Regulated by Autophagy-Induced Mitochondrial Clearance. *Cell Metab.* **24,** 402–419 (2016).
224. Welch, J. S., Ricote, M., Akiyama, T. E., Gonzalez, F. J. & Glass, C. K. PPARγ and PPARδ negatively regulate specific subsets of lipopolysaccharide and IFN-γ target genes in macrophages. *Proc. Natl. Acad. Sci.* **100,** 6712–6717 (2003).

8 Addendum

8.1 Complete list of *P* values for all calculated significant differences

Figure 5.4 C: Immunoblot analysis of LC3-II turnover of wild-type, *NRBF2*+/-, *NRBF2*-/- or NRBF2-/- DT40 cells transfected with empty vector or cDNA encoding for human NRBF2. Values calculated by one-way ANOVA (corrected by Tukey's multiple comparisons test), **P* < 0.05, ***P* < 0.01, ****P* < 0.001, *****P* < 0.0001.

Sample	Adjusted *P* Value	
WT Med vs. WT Med+BafA$_1$	***	0,0006
WT Med vs. WT EBSS	**	0,0012
WT Med vs. WT EBSS+BafA$_1$	****	<0,0001
WT Med vs. NRBF2+/- EBSS+BafA$_1$	****	<0,0001
WT Med vs. NRBF2-/- EBSS+BafA$_1$	**	0,0084
WT Med vs. hNRBF2 Med+BafA$_1$	***	0,0005
WT Med vs. hNRBF2 EBSS+BafA$_1$	****	<0,0001
WT Med vs. vector EBSS+BafA$_1$	**	0,0013
WT Med+BafA$_1$vs. WT EBSS+BafA$_1$	****	<0,0001
WT Med+BafA$_1$vs. NRBF2+/- Med	***	0,0006
WT Med+BafA$_1$vs. NRBF2+/- EBSS+BafA$_1$	*	0,0427
WT Med+BafA$_1$vs. NRBF2-/- Med	***	0,0006
WT Med+BafA$_1$vs. NRBF2-/- EBSS	*	0,0337
WT Med+BafA$_1$vs. hNRBF2 Med	***	0,0006
WT Med+BafA$_1$vs. hNRBF2 EBSS+BafA$_1$	**	0,0023
WT Med+BafA$_1$vs. vector Med	***	0,0006
WT Med+BafA$_1$vs. vector Med+BafA$_1$	*	0,0289
WT EBSS vs. WT EBSS+BafA$_1$	****	<0,0001
WT EBSS vs. NRBF2+/- Med	**	0,0012
WT EBSS vs. NRBF2+/- EBSS+BafA$_1$	*	0,023
WT EBSS vs. NRBF2-/- Med	**	0,0012
WT EBSS vs. hNRBF2 Med	**	0,0012
WT EBSS vs. hNRBF2 EBSS+BafA$_1$	**	0,0011
WT EBSS vs. vector Med	**	0,0012
WT EBSS+BafA$_1$vs. NRBF2+/- Med	****	<0,0001
WT EBSS+BafA$_1$vs. NRBF2+/- Med+BafA$_1$	****	<0,0001
WT EBSS+BafA$_1$vs. NRBF2+/- EBSS	****	<0,0001
WT EBSS+BafA$_1$vs. NRBF2-/- Med	****	<0,0001
WT EBSS+BafA$_1$vs. NRBF2-/- Med+BafA$_1$	****	<0,0001
WT EBSS+BafA$_1$vs. NRBF2-/- EBSS	****	<0,0001
WT EBSS+BafA$_1$vs. NRBF2-/- EBSS+BafA$_1$	****	<0,0001
WT EBSS+BafA$_1$vs. hNRBF2 Med	****	<0,0001
WT EBSS+BafA$_1$vs. hNRBF2 Med+BafA$_1$	****	<0,0001
WT EBSS+BafA$_1$vs. hNRBF2 EBSS	****	<0,0001
WT EBSS+BafA$_1$vs. vector Med	****	<0,0001

WT EBSS+BafA$_1$vs. vector Med+BafA$_1$	****	<0,0001
WT EBSS+BafA$_1$vs. vector EBSS	****	<0,0001
WT EBSS+BafA$_1$vs. vector EBSS+BafA$_1$	****	<0,0001
NRBF2+/- Med vs. NRBF2+/- EBSS+BafA$_1$	****	<0,0001
NRBF2+/- Med vs. NRBF2-/- EBSS+BafA$_1$	**	0,0084
NRBF2+/- Med vs. hNRBF2 Med+BafA$_1$	***	0,0005
NRBF2+/- Med vs. hNRBF2 EBSS+BafA$_1$	****	<0,0001
NRBF2+/- Med vs. vector EBSS+BafA$_1$	**	0,0013
NRBF2+/- Med+BafA$_1$vs. NRBF2+/- EBSS+BafA$_1$	****	<0,0001
NRBF2+/- Med+BafA$_1$vs. hNRBF2 EBSS+BafA$_1$	****	<0,0001
NRBF2+/- EBSS vs. NRBF2+/- EBSS+BafA$_1$	****	<0,0001
NRBF2+/- EBSS vs. hNRBF2 EBSS+BafA$_1$	****	<0,0001
NRBF2+/- EBSS+BafA$_1$vs. NRBF2-/- Med	****	<0,0001
NRBF2+/- EBSS+BafA$_1$vs. NRBF2-/- Med+BafA$_1$	****	<0,0001
NRBF2+/- EBSS+BafA$_1$vs. NRBF2-/- EBSS	****	<0,0001
NRBF2+/- EBSS+BafA$_1$vs. NRBF2-/- EBSS+BafA$_1$	**	0,0034
NRBF2+/- EBSS+BafA$_1$vs. hNRBF2 Med	****	<0,0001
NRBF2+/- EBSS+BafA$_1$vs. hNRBF2 Med+BafA$_1$	*	0,05
NRBF2+/- EBSS+BafA$_1$vs. hNRBF2 EBSS	***	0,0002
NRBF2+/- EBSS+BafA$_1$vs. vector Med	****	<0,0001
NRBF2+/- EBSS+BafA$_1$vs. vector Med+BafA$_1$	****	<0,0001
NRBF2+/- EBSS+BafA$_1$vs. vector EBSS	****	<0,0001
NRBF2+/- EBSS+BafA$_1$vs. vector EBSS+BafA$_1$	*	0,0215
NRBF2-/- Med vs. NRBF2-/- EBSS+BafA$_1$	**	0,0084
NRBF2-/- Med vs. hNRBF2 Med+BafA$_1$	***	0,0005
NRBF2-/- Med vs. hNRBF2 EBSS+BafA$_1$	****	<0,0001
NRBF2-/- Med vs. vector EBSS+BafA$_1$	**	0,0013
NRBF2-/- Med+BafA$_1$vs. hNRBF2 EBSS+BafA$_1$	****	<0,0001
NRBF2-/- EBSS vs. hNRBF2 Med+BafA$_1$	*	0,0285
NRBF2-/- EBSS vs. hNRBF2 EBSS+BafA$_1$	****	<0,0001
NRBF2-/- EBSS+BafA$_1$vs. hNRBF2 Med	**	0,0084
NRBF2-/- EBSS+BafA$_1$vs. hNRBF2 EBSS+BafA$_1$	***	0,0001
NRBF2-/- EBSS+BafA$_1$vs. vector Med	**	0,0084
hNRBF2 Med vs. hNRBF2 Med+BafA$_1$	***	0,0005
hNRBF2 Med vs. hNRBF2 EBSS+BafA$_1$	****	<0,0001
hNRBF2 Med vs. vector EBSS+BafA$_1$	**	0,0013
hNRBF2 Med+BafA$_1$vs. hNRBF2 EBSS+BafA$_1$	**	0,0028
hNRBF2 Med+BafA$_1$vs. vector Med	***	0,0005
hNRBF2 Med+BafA$_1$vs. vector Med+BafA$_1$	*	0,0245
hNRBF2 EBSS vs. hNRBF2 EBSS+BafA$_1$	****	<0,0001
hNRBF2 EBSS+BafA$_1$vs. vector Med	****	<0,0001
hNRBF2 EBSS+BafA$_1$vs. vector Med+BafA$_1$	****	<0,0001
hNRBF2 EBSS+BafA$_1$vs. vector EBSS	****	<0,0001
hNRBF2 EBSS+BafA$_1$vs. vector EBSS+BafA$_1$	**	0,0011
vector Med vs. vector EBSS+BafA$_1$	**	0,0013

Figure 5.7 B: Immunoblot analysis of AM12 cells. Values calculated by one-way ANOVA (corrected by Tukey's multiple comparisons test), **P* < 0.05.

Sample	Adjusted *P* Value
ULK1 Med vs. ULK1 200 µM Wy14643	* 0,0491
LC3-II Med vs. LC3-II EBSS	* 0,0421

Figure 5.7 D: Immunoblot analysis of *nrbf*2 KO MEF cells transfected with empty vector or cDNA encoding for human NRBF2. Values calculated by one-way ANOVA (corrected by Tukey's multiple comparisons test), **P* < 0.05, ***P* < 0.01.

Sample	Adjusted *P* Value
ULK1 EBSS vs. ULK1 GW501516	* 0,0459
ULK1 EBSS vs. ULK1 GW7647	* 0,0183
ULK1 EBSS vs. ULK1 Wy14643	* 0,0201
LC3-II EBSS vs. LC3-II EBSS	* 0,0111
LC3-II EBSS vs. LC3-II Telmisartan	** 0,0094
LC3-II EBSS vs. LC3-II GW501516	** 0,0073
LC3-II EBSS vs. LC3-II GW7647	** 0,0054
LC3-II EBSS vs. LC3-II Wy14643	** 0,0028

Figure 5.14 A: PLA of wild-type and *nrbf2* KO MEF cells. Values calculated by Student *t* test (2-tailed, 2-sample assuming unequal variances), **P* < 0.05.

Sample	*P* Value
MEF WT vs. MEF *nrbf2* KO	* 0,0139

Figure 5.14 B: PLA of wild-type MEF cells transfected with non-targeting control siRNA or *Nrbf2* siRNA. Values calculated by Student *t* test (2-tailed, 2-sample assuming equal variances), **P* < 0.05, ***P* < 0.01.

Sample	*P* Value
control siRNA Med vs. *Nrbf2* siRNA Med	** 0,0011
control siRNA EBSS vs. *Nrbf2* siRNA EBSS	* 0,0152
control siRNA EBSS+MRT67307 vs. *Nrbf2* siRNA EBSS+MRT67307	* 0,0266

Figure 5.18 C: Immunoblot analysis of LC3-II and SQSTM/p62 turnover of *nrbf2* KO MEF cells transfected with empty vector or cDNA encoding for NRBF2-variants. Values calculated by one-way ANOVA (corrected by Tukey's multiple comparisons test), **P* < 0.05, ***P* < 0.01, ****P* < 0.001, *****P* < 0.0001.

LC3-II

Sample	Adjusted P Value	
vector Med vs. vector EBSS+BafA$_1$	*	0,0233
vector Med vs. NRBF2 WT EBSS+BafA$_1$	**	0,0032
vector Med vs. NRBF2 5S-A EBSS+BafA$_1$	****	<0,0001
vector Med vs. NRBF2 5S-D EBSS+BafA$_1$	**	0,0045
vector Med+BafA$_1$ vs. NRBF2 WT EBSS+BafA$_1$	*	0,0257
vector Med+BafA$_1$ vs. NRBF2 5S-A EBSS+BafA$_1$	***	0,0003
vector Med+BafA$_1$ vs. +BafA$_1$NRBF2 5S-D EBSS+BafA$_1$	*	0,0349
vector EBSS vs. vector EBSS+BafA$_1$	**	0,008
vector EBSS vs. NRBF2 WT EBSS+BafA$_1$	**	0,001
vector EBSS vs. NRBF2 5S-A EBSS+BafA$_1$	****	<0,0001
vector EBSS vs. NRBF2 5S-D EBSS+BafA$_1$	**	0,0014
vector EBSS+BafA$_1$ vs. NRBF2 WT Med	**	0,0036
vector EBSS+BafA$_1$ vs. NRBF2 WT EBSS	*	0,0128
vector EBSS+BafA$_1$ vs. NRBF2 5S-A Med	*	0,0115
vector EBSS+BafA$_1$ vs. NRBF2 5S-A EBSS	*	0,0246
vector EBSS+BafA$_1$ vs. NRBF2 5S-D Med	*	0,0121
vector EBSS+BafA$_1$ vs. NRBF2 5S-D EBSS	*	0,0183
NRBF2 WT Med vs. NRBF2 WT EBSS+BafA$_1$	***	0,0004
NRBF2 WT Med vs. NRBF2 5S-A EBSS+BafA$_1$	****	<0,0001
NRBF2 WT Med vs. NRBF2 5S-D EBSS+BafA$_1$	***	0,0006
NRBF2 WT Med+BafA$_1$ vs. NRBF2 WT EBSS+BafA$_1$	**	0,0091
NRBF2 WT Med+BafA$_1$ vs. NRBF2 5S-A EBSS+BafA$_1$	****	<0,0001
NRBF2 WT Med+BafA$_1$ vs. NRBF2 5S-D EBSS+BafA$_1$	*	0,0126
NRBF2 WT EBSS vs. NRBF2 WT EBSS+BafA$_1$	**	0,0017
NRBF2 WT EBSS vs. NRBF2 5S-A EBSS+BafA$_1$	****	<0,0001
NRBF2 WT EBSS vs. NRBF2 5S-D EBSS+BafA$_1$	**	0,0024
NRBF2 WT EBSS+BafA$_1$ vs. NRBF2 5S-A Med	**	0,0015
NRBF2 WT EBSS+BafA$_1$ vs. NRBF2 5S-A EBSS	**	0,0034
NRBF2 WT EBSS+BafA$_1$ vs. NRBF2 5S-D Med	**	0,0016
NRBF2 WT EBSS+BafA$_1$ vs. NRBF2 5S-D EBSS	**	0,0025
NRBF2 5S-A Med vs. NRBF2 5S-A EBSS+BafA$_1$	****	<0,0001
NRBF2 5S-A Med vs. NRBF2 5S-D EBSS+BafA$_1$	**	0,0021
NRBF2 5S-A Med+BafA$_1$ vs. NRBF2 5S-A EBSS+BafA$_1$	**	0,0015
NRBF2 5S-A EBSS vs. NRBF2 5S-A EBSS+BafA$_1$	****	<0,0001
NRBF2 5S-A EBSS vs. NRBF2 5S-D EBSS+BafA$_1$	**	0,0048
NRBF2 5S-A EBSS+BafA$_1$ vs. NRBF2 5S-D Med	****	<0,0001
NRBF2 5S-A EBSS+BafA$_1$ vs. NRBF2 5S-D Med+BafA$_1$	**	0,0086
NRBF2 5S-A EBSS+BafA$_1$ vs. NRBF2 5S-D EBSS	****	<0,0001

NRBF2 5S-D Med vs. NRBF2 5S-D EBSS+BafA$_1$	**	0,0022
NRBF2 5S-D EBSS vs. NRBF2 5S-D EBSS+BafA$_1$	**	0,0035

SQSTM/p62

Sample	Adjusted P Value	
vector Med vs. NRBF2 5S-A EBSS+BafA$_1$	*	0,0189
vector Med+BafA$_1$ vs. NRBF2 5S-A EBSS+BafA$_1$	**	0,0028
vector EBSS vs. NRBF2 5S-A EBSS+BafA$_1$	***	0,0005
vector EBSS+BafA$_1$ vs. NRBF2 WT Med	*	0,0385
vector EBSS+BafA$_1$ vs. NRBF2 WT EBSS	**	0,0087
NRBF2 WT Med vs. NRBF2 5S-A EBSS+BafA$_1$	***	0,0003
NRBF2 WT Med+BafA$_1$ vs. NRBF2 5S-A EBSS+BafA$_1$	**	0,0014
NRBF2 WT EBSS vs. NRBF2 5S-A EBSS+BafA$_1$	****	<0,0001
NRBF2 WT EBSS+BafA$_1$ vs. NRBF2 5S-A EBSS+BafA$_1$	*	0,0132
NRBF2 5S-A Med vs. NRBF2 5S-A EBSS+BafA$_1$	*	0,0132
NRBF2 5S-A EBSS vs. NRBF2 5S-A EBSS+BafA$_1$	**	0,0019
NRBF2 5S-A EBSS+BafA$_1$ vs. NRBF2 5S-D Med	*	0,0221
NRBF2 5S-A EBSS+BafA$_1$ vs. NRBF2 5S-D Med+BafA$_1$	*	0,0109
NRBF2 5S-A EBSS+BafA$_1$ vs. NRBF2 5S-D EBSS	***	0,0007
NRBF2 5S-A EBSS+BafA$_1$ vs. NRBF2 5S-D EBSS+BafA$_1$	*	0,0366

Figure 5.19 B: Immunofluorescence of LC3 of *nrbf2* KO MEF cells transfected with empty vector or cDNA encoding for NRBF2-variants. Values calculated by one-way ANOVA (corrected by Tukey's multiple comparisons test), *$P < 0.05$, **$P < 0.01$, ***$P < 0.001$, ****$P < 0.0001$.

Sample	Adjusted *P* Value	
vector Med vs. vector EBSS+BafA$_1$	****	<0,0001
vector Med vs. NRBF2 WT Med+BafA$_1$	*	0,0218
vector Med vs. NRBF2 WT EBSS+BafA$_1$	****	<0,0001
vector Med vs. NRBF2 5S-A Med+BafA$_1$	***	0,001
vector Med vs. NRBF2 5S-A EBSS+BafA$_1$	****	<0,0001
vector Med vs. NRBF2 5S-D EBSS+BafA$_1$	****	<0,0001
vector Med+BafA$_1$ vs. vector EBSS+BafA$_1$	****	<0,0001
vector Med+BafA$_1$ vs. NRBF2 WT EBSS+BafA$_1$	****	<0,0001
vector Med+BafA$_1$ vs. NRBF2 5S-A EBSS+BafA$_1$	****	<0,0001
vector Med+BafA$_1$ vs. NRBF2 5S-D EBSS+BafA$_1$	****	<0,0001
vector EBSS vs. vector EBSS+BafA$_1$	****	<0,0001
vector EBSS vs. NRBF2 WT EBSS+BafA$_1$	****	<0,0001
vector EBSS vs. NRBF2 5S-A EBSS+BafA$_1$	****	<0,0001
vector EBSS vs. NRBF2 5S-D EBSS+BafA$_1$	****	<0,0001
vector EBSS+BafA$_1$ vs. NRBF2 WT Med	****	<0,0001
vector EBSS+BafA$_1$ vs. NRBF2 WT Med+BafA$_1$	****	<0,0001

vector EBSS+BafA$_1$ vs. NRBF2 WT EBSS	****	<0,0001
vector EBSS+BafA$_1$ vs. NRBF2 5S-A Med	****	<0,0001
vector EBSS+BafA$_1$ vs. NRBF2 5S-A Med+BafA$_1$	**	0,0081
vector EBSS+BafA$_1$ vs. NRBF2 5S-A EBSS	****	<0,0001
vector EBSS+BafA$_1$ vs. NRBF2 5S-D Med	****	<0,0001
vector EBSS+BafA$_1$ vs. NRBF2 5S-D Med+BafA$_1$	****	<0,0001
vector EBSS+BafA$_1$ vs. NRBF2 5S-D EBSS	****	<0,0001
NRBF2 WT Med vs. NRBF2WT EBSS+BafA$_1$	****	<0,0001
NRBF2 WT Med vs. NRBF2 5S-A EBSS+BafA$_1$	****	<0,0001
NRBF2 WT Med vs. NRBF2 5S-D EBSS+BafA$_1$	****	<0,0001
NRBF2 WT Med+BafA$_1$ vs. NRBF2 WT EBSS+BafA$_1$	****	<0,0001
NRBF2 WT Med+BafA$_1$ vs. NRBF2 5S-A EBSS+BafA$_1$	**	0,0015
NRBF2 WT Med+BafA$_1$ vs. NRBF2 5S-D EBSS+BafA$_1$	***	0,0007
NRBF2 WT EBSS vs. NRBF2 WT EBSS+BafA$_1$	****	<0,0001
NRBF2 WT EBSS vs. NRBF2 5S-A EBSS+BafA$_1$	***	0,0002
NRBF2 WT EBSS vs. NRBF2 5S-D EBSS+BafA$_1$	****	<0,0001
NRBF2 WT EBSS+BafA$_1$ vs. NRBF2 5S-A Med	****	<0,0001
NRBF2 WT EBSS+BafA$_1$ vs. NRBF2 5S-A Med+BafA$_1$	****	<0,0001
NRBF2 WT EBSS+BafA$_1$ vs. NRBF2 5S-A EBSS	****	<0,0001
NRBF2 WT EBSS+BafA$_1$ vs. NRBF2 5S-D Med	****	<0,0001
NRBF2 WT EBSS+BafA$_1$ vs. NRBF2 5S-D Med+BafA$_1$	****	<0,0001
NRBF2 WT EBSS+BafA$_1$ vs. NRBF2 5S-D EBSS	****	<0,0001
NRBF2 5S-A Med vs. NRBF2 5S-A Med+BafA$_1$	*	0,0133
NRBF2 5S-A Med vs. NRBF2 5S-A EBSS+BafA$_1$	****	<0,0001
NRBF2 5S-A Med vs. NRBF2 5S-D EBSS+BafA$_1$	****	<0,0001
NRBF2 5S-A Med+BafA$_1$ vs. NRBF2 5S-D Med	**	0,0048
NRBF2 5S-A Med+BafA$_1$ vs. NRBF2 5S-D EBSS+BafA$_1$	*	0,0357
NRBF2 5S-A EBSS vs. NRBF2 5S-A EBSS+BafA$_1$	****	<0,0001
NRBF2 5S-A EBSS vs. NRBF2 5S-D EBSS+BafA$_1$	****	<0,0001
NRBF2 5S-A EBSS+BafA$_1$ vs. NRBF2 5S-D Med	****	<0,0001
NRBF2 5S-A EBSS+BafA$_1$ vs. NRBF2 5S-D Med+BafA$_1$	***	0,0002
NRBF2 5S-A EBSS+BafA$_1$ vs. NRBF2 5S-D EBSS	****	<0,0001
NRBF2 5S-D Med vs. NRBF2 5S-D EBSS+BafA$_1$	****	<0,0001
NRBF2 5S-D Med+BafA$_1$ vs. NRBF2 5S-D EBSS+BafA$_1$	****	<0,0001
NRBF2 5S-D EBSS vs. NRBF2 5S-D EBSS+BafA$_1$	****	<0,0001

Figure 5.21 B: Immunofluorescence of WIPI2 of *nrbf2* KO MEF cells transfected with empty vector or cDNA encoding for NRBF2-variants. Values calculated by one-way ANOVA (corrected by Tukey's multiple comparisons test), *P < 0.05, **P < 0.01, ****P < 0.0001.

Sample	**Adjusted P Value**	
vector Med vs. NRBF2 WT EBSS	*	0,0324
vector Med vs. NRBF2 5S-A EBSS	*	0,0436
vector Med vs. NRBF2 5S-D EBSS	****	<0,0001
vector EBSS vs. NRBF2 WT EBSS	*	0,0218

vector EBSS vs. NRBF2 5S-A EBSS	*	0,0285
vector EBSS vs. NRBF2 5S-D EBSS	****	<0,0001
NRBF2 WT Med vs. NRBF2 WT EBSS	*	0,0309
NRBF2 WT Med vs. NRBF2 5S-A EBSS	*	0,0414
NRBF2 WT Med vs. NRBF2 5S-D EBSS	****	<0,0001
NRBF2 WT EBSS vs. NRBF2 5S-A Med	*	0,0223
NRBF2 WT EBSS vs. NRBF2 5S-D Med	*	0,0213
NRBF2 WT EBSS vs. NRBF2 5S-D EBSS	*	0,0108
NRBF2 5S-A Med vs. NRBF2 5S-A EBSS	*	0,0282
NRBF2 5S-A Med vs. NRBF2 5S-D EBSS	****	<0,0001
NRBF2 5S-A EBSS vs. NRBF2 5S-D Med	*	0,0268
NRBF2 5S-A EBSS vs. NRBF2 5S-D EBSS	**	0,0013
NRBF2 5S-D Med vs. NRBF2 5S-D EBSS	****	<0,0001

8.2 Publications

Parts of this thesis are included in the following manuscript

Berleth N, Wallot-Hieke N, Wu W, Schlütermann D, Böhler P, Stuhldreier F, Deitersen J, Cox J, Schmitz K, Seggewiß S, Peter C, Berleth M, Groth G, Tschapek A, Gödecke A and Stork B. *ULK1 Regulates the Class III PtdIns3K Complex via the Phosphorylation of NRBF2*. **Cellular Physiology and Biochemistry** [accepted for publication].

Further publications

Dieterle AM, Böhler P, Keppeler H, Alers S, **Berleth N**, Drießen S, Hieke N, Pietkiewicz S, Löffler AS, Peter C, Gray A, Leslie NR, Shinohara H, Kurosaki T, Engelke M, Wienands J, Bonin M, Wesselborg S and Stork B. (2014) *PDK1 Controls Upstream PI3K Expression and PIP3 Generation.* **Oncogene** 33(23) 3043–53.

Drießen S, **Berleth N**, Friesen O, Löffler AS, Böhler P, Hieke N, Stuhldreier F, Peter C, Schink KO, Schultz SW, Stenmark H, Holland P, Simonsen A, Wesselborg S and Stork B. (2015) *Deubiquitinase Inhibition by WP1130 Leads to ULK1 Aggregation and Blockade of Autophagy.* **Autophagy** 11(9) 1458–70.

Hieke N, Löffler AS, Kaizuka T, **Berleth N**, Böhler P, Drießen S, Stuhldreier F, Friesen O, Assani K, Schmitz K, Peter C, Diedrich B, Dengjel J, Holland P, Simonsen A, Wesselborg S, Mizushima N and Stork B. (2015) *Expression of a ULK1/2 Binding-Deficient ATG13 Variant Can Partially Restore Autophagic Activity in ATG13-Deficient Cells.* **Autophagy** 11(9) 1471–83.

Schlütermann D, Skowron MA, **Berleth N**, Böhler P, Deitersen J, Stuhldreier F, Wallot-Hieke N, Wu W, Peter C, Hoffmann MJ, Niegisch G and Stork B. (2018) *Targeting Urothelial Carcinoma Cells by Combining Cisplatin with a Specific Inhibitor of the Autophagy-Inducing Class III PtdIns3K Complex.* **Urol Oncol** 36(4).

Böhler P, Stuhldreier F, Anand R, Kondadi AK, Schlütermann D, **Berleth N**, Deitersen J, Wallot-Hieke N, Wu W, Frank M, Niemann H, Wesbuer E, Barbian A, Luyten T, Parys JB, Weidtkamp-Peters S, Borchardt A, Reichert AS, Peña-Blanco A, García-Sáez AJ, Itskanov S, van der Bliek AM, Proksch P, Wesselborg S and Stork B. (2018) *The Mycotoxin Phomoxanthone A Disturbs the Form and Function of the Inner Mitochondrial Membrane.* **Cell Death Dis** 9(3).

Wallot-Hieke N, Verma N, Schlütermann D, **Berleth N**, Deitersen J, Böhler P, Stuhldreier F, Wu W, Seggewiß S, Peter C, Gohlke H, Mizushima N and Stork B. (2018) *Systematic Analysis of ATG13 Domain Requirements for Autophagy Induction.* **Autophagy** 14(5) 743–63.

Erklärung

Ich versichere an Eides Statt, dass die Dissertation von mir selbständig und ohne unzulässige fremde Hilfe unter Beachtung der „Grundsätze zur Sicherung guter wissenschaftlicher Praxis an der Heinrich-Heine-Universität Düsseldorf“ erstellt worden ist. Die vorliegende Arbeit wurde von mir selbständig verfasst und keine anderen als die angegebenen Hilfsmittel verwendet. Alle wörtlich oder inhaltlich übernommenen Stellen habe ich als solche gekennzeichnet. Zudem versichere ich, dass ich die vorliegende Dissertation nur in diesem und keinem anderen Promotionsverfahren eingereicht habe und diesem kein früheres Promotionsverfahren vorausgegangen ist.

_____ _____

Ort, Datum Niklas Berleth